LUND UNIVERSITY

Electric Traction Machine Design for an E-RWD Unit

Marquez, Francisco

2014

[Link to publication](#)

Citation for published version (APA):
Marquez, F. (2014). *Electric Traction Machine Design for an E-RWD Unit.* [Doctoral Thesis (monograph), Division for Industrial Electrical Engineering and Automation].

Total number of authors:
1

Electric traction machine design for an E-RWD unit.

Francisco J. Márquez-Fernández

LUND UNIVERSITY

To The Beatles, Camarón y Paco,
W.A. Mozart & Janis Joplin.

TO MY FAMILY.

Abstract

Since the first generation of the Toyota Prius was introduced in December 1997, the number of Hybrid Electric Vehicles (HEVs) and pure Electric Vehicles (EVs) available in the market has increased substantially. Nowadays, sixteen years later, almost every car manufacturer has one or several HEV models within their range, and the most daring even have a pure electric configuration. Besides, the higher number of alternatives available is also reflected in the sales numbers, and the market share corresponding to HEVs and EVs is steadily increasing particularly in Europe, the United States and Japan.

EVs and HEVs were first developed at the end of the nineteenth century, and although the basic concept has not changed, bringing a new HEV or EV model up to the market has associated high development costs. The growing competition existent puts high demands on the electric system as well as the rest of the vehicle. As a consequence, substantial design effort is devoted to optimize both at system and component level, with respect to different parameters such as fuel efficiency, power density, cost and reliability. As bidirectional energy converters between electric and mechanical energy, electrical machines play an essential role inside electric or hybrid drivelines. All the power coming either to or from the electric energy source must be converted in the electrical machine. It is then obvious that the performance of the electrical machine has a high impact on the overall traction system, and therefore a thorough machine design is crucial for a successful electric driveline. However, the design of an electric traction machine for an EV or an HEV has to be addressed in a different way than a conventional machine for industrial purposes. The load profile of an electric traction motor is highly dynamic, depending on the driver's requirements and the external driving conditions, making it hard to define nominal operation conditions. Moreover, the requirements placed on the electrical machine in terms of size, weight, power density, efficiency and cost are usually strict. All this makes the design of such a machine a challenge, and new methodologies are needed in order to accomplish it.

This thesis describes in detail the design process of an electric traction machine for a particular HEV application, an Electric Rear Wheel Drive (E-RWD) unit. The evolution of the design is presented, analyzing the effect of the different driving forces at the different stages. Although it may seem

obvious, the most important prerequisite for a successful design is a sufficient and consistent set of specifications. However, the specifications needed for an electric traction machine design differ from those traditionally used for industrial machines. Throughout the thesis it is seen that a modest change on the specifications can lead to a significantly different solution. For this reason, a minimum set of initial specifications is proposed, together with the new machine design methodology based on the description of the load profile in the form of driving cycles.

The manufacturing of a prototype and the experimental validation of the design are also covered in this work. General considerations about different prototyping aspects such as the selection of materials, cutting of the laminations and winding configuration are discussed. Besides, experimental measurements are also presented in order to validate the design results. Two different test methods are used: conventional steady state test, loading the machine at different operation points, and dynamic braking. In addition, the traction machine is integrated in the E-RWD unit, and tested onboard the vehicle.

From the experience gained both from the design and the experimental testing phases, it appears that the performance of the machine is usually limited by its thermal capabilities. Improving the cooling conditions allows to operate the machine at higher power levels, which has a direct influence on the outcome of the design process. A way to enhance the cooling capabilities for conventional radial flux machines is investigated. Moreover, a machine design with a completely novel cooling concept based on direct cooling of laminated stator windings is presented, and its thermal characteristics are extensively analyzed.

Acknowledgements

BorgWarner, for sharing both the good and bad moments, late nights and weekends. You guys made this fun, even when things did not work out.

I cannot forget to thank my colleagues at the Industrial Electrical Engineering and Automation division. It has been a pleasure to work with you all these years, and I really hope to continue being part of the IEA crew. Thank you very much to all of you.

Living in Lund is like living in a tiny, tidy, nearly-perfect bubble surrounded by all sorts of curious and interesting people, most of them connected to science in some way. In this environment there is room for everything, from the most interesting discussions to the most surrealistic jokes. Alex, Xavi, Evripidis, Zhe, Eva, Hamid, Emily and many others; I would like to thank you all for being my family inside the bubble. A huge kiss goes to Ares, who came to Lund with me in the first place, and has always been there for me. *Mnita, gràcies per tot.*

I usually say that I am a musician with a huge interest for engineering. I am sure I could have never made it in Lund without music, and as many other things in life, music is much more fun when you share it. I want to sing thank you to Patric, Stephan, Sabina, Yasmin, Anki, Niklas and Johan for putting their hearts into our *Flamenco del Sur* project, and showing that music does not care about language differences, since music is a language by itself.

Back home in Spain, the list is endless. I just want to say thank you guys, for making me feel home every time, as if no time has ever passed. Thank you for the support, the encouragement, the updates and the warmth. Luismi, Samu, Isa & Jose, Manuel, Joaquín, Zara, Yadira, Raquel & Rita... you all know what you mean to me. Besides, I would not have been able to complete this work without the unconditional support of Rosa, *muchísimas gracias por ser tan tú, siempre conmigo.*

And last, but not least, I want to thank my family. They say that you choose your friends, but you cannot choose your family. Well, if I could, I would have chosen mine. Thank you very very much *Má and Pá* (Maribel & Paco) for being the best people I know. I cannot find the words to say how lucky I feel to have you, but perhaps there are no words for certain feelings. I want to thank my little sister, Elo. She can understand me in a way nobody else does. When she smiles, I know everything is going to be alright. Since the best is always saved for last, I would like to heartly thank my grandpa Pepe. Listening to him, seeing the world through his eyes, is the best way of learning about life. *Familia, os quiero muchísimo a todos. Gracias.*

Lund, December 15th 2013

Fran

Contents

Chapter 1

Introduction

1.1   Background

The road vehicle market in general, and the passenger car market in particular is experiencing a noticeable rise in the number of Electric Vehicles (EVs) and Hybrid Electric Vehicles (HEVs) commercially available. In the same way, the sales of electric driven vehicles increase, and even though they still represent a small fraction of the total vehicle sales, the numbers are continuously growing.

According to the Electric Drive Transportation Association (EDTA), 487480 electric powered transport vehicles (both EVs, and HEVs of different kinds) were sold in the US during 2012, which represents 3.38% of the total sales, compared to 284064 units (2.23%) in 2011, 274555 units (2.37%) in 2010 and 290292 units (2.78%) in 2009 [1]. In Europe (EU-27), the figures are smaller, and the International Council on Clean Transportation (ICCT) reports a market penetration of 0.77% in 2011, 0.61% in 2010 and 0.05% in 2009 for EVs and HEVs together [2]. Particularly interesting is the case of Norway at the time of finishing this work, with almost 12% of the passenger car sales in November 2013 being pure EVs and 8.9% HEVs [3].

But, what are the reasons behind this phenomenon? Why are there more and more electric and hybrid models available, from virtually all main car manufacturers? Looking at the evolution of the market over the last years, EVs and HEVs do not appear as a very interesting market niche when compared for example to small high-efficiency diesel cars in Europe, which currently dominate the passenger car market with over 55% of the market share on average (as high as 75% in Belgium and 78% in Luxemburg in year 2012). In addition, electric driven vehicles require higher development costs. Although electric

passenger cars are nothing new, the first models coming from the end of the nineteenth century, each and every electric component and/or system onboard the vehicle must comply with the current automotive standards, which implies a substantial effort to either bring up a new design or adapt an existing concept to the automotive regulations. Nonetheless, there are a number of reasons that make EVs and HEVs very attractive and promote their further development, highlighting them as a promising solution for future transportation.

Perhaps, the strongest argument in favor of electric powered vehicles is that they do not obtain the energy directly from fossil fuels. It is now a well known fact that fossil fuels are a limited resource; and even though there are still undiscovered deposits, and new technologies could facilitate the exploitation of non-conventional fossil fuels, the most optimistic predictions foresee a time horizon of a couple of hundred years at the most [4–7].

With this in mind, it is clear that a transition towards alternative renewable energy sources is needed. In fact, this transition has already started, and in the particular case of road transportation, the different kinds of Electric and Hybrid Electric Vehicles are a clear step in that direction.

As of today, fuel consumption figures for HEVs, except plug-in HEVs, are comparable to those of the new high-efficient diesel (and even some gasoline) vehicles, being generally superior in city driving when a significant fraction of the energy can be recovered through regenerative braking. However, in highway driving, the advantages of the hybrid driveline are not so noticeable, and it is hard to motivate the extra cost of the electric components. Nevertheless, HEVs are a necessary step towards pure EVs, serving as a real-life test bench for the new technical solutions, helping on the makeover of the industry and research centers towards electric propulsion, and being a perfect showcase to bring the technology closer to the general public.

Another argument supporting electric powered vehicles is their reduced impact on the atmosphere and the air quality. Nowadays there is a general concern about global warming and the greenhouse effect, and there is no doubt about the role played by the emissions coming from the different means of transportation in these phenomena [8, 9]. In EVs, since no combustion takes place, there are virtually no harmful emissions coming from the vehicle itself, which is a plus especially in highly densely populated areas. Of course, in the case of HEVs there are still emissions since part of the energy comes from the combustion engine, but the emission level is reduced proportionally to the fuel consumption. Whether electric vehicles have an impact on the atmosphere or not depends of course on the origin of the electric energy stored in the battery.

It is not within the scope of this thesis to get into this discussion, however, with pure EVs there is at least the possibility to use electricity from renewable sources, minimizing their environmental impact in that respect.

In addition, vehicles equipped with an electric drive can become safer and much more fun to drive. The dynamics of the electric system are substantially faster than those of the conventional combustion engine driveline. This implies a faster response to the driver's commands, but also to the different safety systems under potentially dangerous situations.

A key challenge in hybrid and electric propulsion research is battery technology, since batteries are pointed out as the main hindrance for the successful introduction of EVs and HEVs in the general market. The main issues connected to batteries in EVs and HEVs are related to the effective driving range of the vehicle for a certain battery size and weight, as well as increased vehicle cost. New battery technologies with improved energy and power densities appear regularly, and figures as high as $400\,Wh/kg$ [10] and $4500\,W/kg$ [11] are reported for energy and power density optimized cells respectively. Yet, current batteries are still barely sufficient to provide a driving range of a couple of hundred kilometers in the best case, within reasonable limits of size and weight. However, the role of the electrical machine in the electric drivetrain should not be overlooked. All the energy used by the electrical propulsion system is transformed from electric to mechanical energy -or vice versa- in the electrical machine. Thereby, improving the efficiency of the electrical machine has a direct impact on either the fuel consumption (in case of a HEV), the size of the battery, or both.

Electrical machines are well known devices, which have been around for almost 200 years now. The first direct current (DC) machines were developed around 1830, and approximately 50 years later, Galileo Ferraris and Nikola Tesla presented their alternating current (AC) machines independently. It just took a couple of decades until the concept was developed to a point similar to today's.

For most of this time, electrical machines have been designed to work under fairly constant loads, mostly in stationary industrial applications. The design process in this case is relatively easy. The machine should be able to run indefinitely at a predefined nominal operation point, while being able to get overloaded transiently, usually with a known duty cycle as well. However, when it comes to traction applications, the scenario is completely different. The operation regime of the electrical machine varies quite a lot from a pure EV, in which all the traction power needed must be supplied by the electric drive, to a HEV, in which the electric drive usually delivers high power during short

periods of time, in order to help the combustion engine when needed or to take care of the regeneration of the braking energy. In both cases, it is hard to define a nominal operation point, since the load is continuously varying according to the driver's requirements, and the driving circumstances. For this reason, an off-the-shelf machine optimized to work in an industrial application, is usually not a very good solution for an electric powertrain.

Designing electric traction machines is a challenge. The demands placed on the machine in terms of size, weight, torque and power density and cost are tight. Some of these demands conflict with each other, forcing the designer to find the best compromise for each particular application. In order to evaluate the suitability of a certain machine design for a particular application, or to compare between different designs, the complete vehicle and the driving conditions (most commonly in the form of a driving cycle) need to be considered. The driving cycle defines the inputs to the vehicle model, the desired speed profile, the inclination of the road and any other relevant driving condition not dependent on the vehicle. In turn, the vehicle model derives the load applied to the electrical machine based on the driving cycle inputs and the configuration of the powertrain. It is worth noticing that even the vehicle control strategy influences the final design, particularly in HEVs where the tractive power demands are split between the combustion engine and the electric propulsion system.

1.2   Scope of this work

This thesis addresses the design of the traction machine for one specific HEV application, an Electrical Rear Wheel Drive (E-RWD) unit, as described in Chapter 2. First, a machine design is proposed based on a handful of specifications provided by the vehicle manufacturer, where natural cooling and high packing density are prioritized. This solution is tested both off and on board, and from the test results, a partial redesign of the machine is proposed, taking into account the driving cycles and the configuration of the complete vehicle. This time, peak power and torque capabilities stand out among the technical requirements, and alternative cooling concepts other than natural cooling become vital to achieve the design goal. Besides, some time is devoted to more practical matters such as prototyping, testing, and implementing a suitable control scheme for the unit to work onboard the vehicle. A section in the thesis covers the most relevant aspects of the prototyping and testing phases.

At last, an innovative machine concept with exceptional cooling capabilities is presented. This new concept allows to consider different cooling scenarios

when the machine operates within the nominal power range and during overload, which results in a smaller, lighter and likely less expensive machine.

1.3   Thesis outline

The document is structured in five chapters (plus 3 appendixes) which reflect the evolution over time of the research work. The first chapter starts with a general introduction to pure Electric and Hybrid Electric Vehicles and the role played by electrical machines in such vehicles. The scope of the work and the outline of the thesis are also included as part of this chapter. Following the introduction, Chapter 2 introduces the E-RWD concept, and expounds on the design, prototyping and experimental validation of an Interior Permanent Magnet Synchronous Machine (IPMSM) that fulfills the design specification set.

After testing the electrical machine standalone and integrated in the E-RWD unit (both in a test bench and onboard the vehicle) some of the design specifications are updated. Chapter 3 deals with the redesign process of the electrical machine resulting from Chapter 2 in order to meet the new requirements.

Chapter 4 proposes a completely different machine concept for the same application. Based on the experience gained, a novel topology with enhanced cooling capabilities is introduced. The ability of easily adjusting the cooling power depending on the thermal context and the desired machine operation appears as a real asset for the E-RWD application.

The last chapter summarizes the most relevant conclusions that can be drawn from the previous discussions, and suggests several research lines that may be interesting for future work on the topic.

The appendixes at the end of the thesis collect relevant information and documents which, although they are not indispensable for the comprehension of the presented analysis, may be valuable for the more interested reader.

1.4   Scientific contributions

The main contributions of this thesis are:

- A deeply detailed description of a HEV traction machine design process, as it evolves steered by the changes in the technical specifications stated by the final user, i.e. the car manufacturer.

- The development of an alternative design methodology based on driving cycle data and a model of the complete vehicle, which proves to be more appropriate for traction applications.

- The compilation of the experience gained into a sort of handbook for the design of electrical machines for traction applications, where the author compiles the most important design specifications that the designer should be provided with, and describes the main steps towards a successful traction machine design.

- A contribution to the development of a design tool for radial flux electrical machines originated at the Industrial Electrical Engineering and Automation (IEA) division, at Lund University.

- An extension of the aforementioned design tool to create lumped-parameter thermal models automatically from the machine geometry and material data. This models are later used in different projects, integrated in more complex models to evaluate the time evolution of the temperatures of the different hybrid driveline components over a driving cycle.

- Thermal and electromagnetic analysis of a novel machine topology with exceptional cooling capabilities, allowing for direct cooling of the winding turns. A topology that can boost its cooling capacity significantly and in a very short time seems perfect for a traction application, in which the load profile is highly dynamic. An alternative design of such motor for the E-RWD application is also presented, according to the guidelines previously laid.

1.5   Publications

Part of the work presented in this thesis is also reported in the publications listed below:

- Avo Reinap, Dan Hagstedt, Francisco Márquez-Fernández and Yury Loayza. Development of a radial flux machine design environment. *XVIII International Conference on Electrical Machines ICEM2008*, Vilamoura (Portugal), 2008.

- Francisco Márquez-Fernández, Avo Reinap and Mats Alaküla. Design, optimization and construction of an electric motor for an Electric Rear Wheel Drive unit application for a hybrid passenger car. *XIX International Conference on Electrical Machines ICEM2010*, Roma (Italy), 2010.

- Francisco Márquez-Fernández, Avo Reinap, Zhe Huang and Mats Alaküla. Dynamic evaluation of the overloading potential of a convection cooled Permanent Magnet Synchronous Motor. *2011 IEEE International Electrical Machines and Drives Conference IEMDC2011*, Niagara Falls (US), 2011.

- Francisco Márquez-Fernández, Zhe Huang, and Mats Alaküla. Redesign of an Electrical Rear Wheel Drive (E-RWD) for a Hybrid Vehicle in a given drive cycle. *XX International Conference on Electrical Machines ICEM2012*, Marseille (France), 2012.

- Zhe Huang, Francisco Márquez-Fernández, Mats Alaküla, and Jinliang Yuan. Characterization and application of forced cooling channels for traction motors in HEVs. *XX International Conference on Electrical Machines ICEM2012*, Marseille (France), 2012.

Although related to the topic, the following publication is not included in this thesis.

- Dan Hagstedt, Francisco Márquez-Fernández and Mats Alaküla. A comparison between PMSM, EMSM and SMSM in a BAS application. *XVIII International Conference on Electrical Machines ICEM2008*, Vilamoura (Portugal), 2008.

Chapter 2

E-RWD unit traction machine design

2.1   Background and description

The concept of hybrid traction applied to passenger cars is nothing really new. The first documented realization, coming from 1898, was built by Ferdinand Porsche in Germany. The Lohner-Porsche petrol-electric "Mixte" is a series hybrid, in which a petrol engine operated at constant speed drives a dynamo in order to charge a bank of accumulators. The electrical machines are installed inside the hubs of the front weels, avoiding the use of drive shafts, transmission, gears, clutch, belts or chains, etc. Inspired by the Lohner-Porsche, several other hybrid vehicles were manufactured up to the 1920's, when combustion engine vehicles took over the passenger transport market driven by the low prices of petrol and the price reduction resulting from the mass production methods developed by Henry Ford. Some of these hybrid solutions actually contributed to develop the concept further, such as the Henri-Pieper Auto-mixte (Liege, Belgium 1906). In this case, a 24 h.p. combustion engine is used to drive an electrical machine via a magnetic disc clutch. The electrical machine is coupled to the rear wheels through a chain transmission. While the Lohner-Porsche is configured as a series hybrid, the Henri-Pieper features a parallel topology in which the electrical machine is used as a generator when the combustion engine is low loaded or when braking in order to charge the batteries; or alternatively as a motor in order to provide extra boost when the torque demands were high [12–14]. This is the same functional description as of a general parallel hybrid of today.

Although some other models were manufactured with limited success, particularly during the Arab oil embargo in the 1960s and 1970s, it is not until the introduction of the first Toyota Prius in 1997 that hybrid vehicles start playing a role in the passenger car market. The Prius is then the first modern hybrid car, i.e. the first mass produced hybrid car according to modern automotive industry standards.

The first Prius model, as well as all the subsequent hybrids manufactured by Toyota Motor Corporation, features a complex hybrid topology, in which the combustion engine is combined with two electrical machines (one mainly working as a motor and one as a generator, although they can both operate in both modes eventually). A planetary gear set is used to split the power conveniently between the combustion engine and the electrical machines. [15]

A bit later than Toyota, another Japanese car manufacturer, Honda, presented a number of hybrid models as well. Honda however opted for a simpler powertrain solution, and all their hybrid alternatives feature a parallel configuration. This reduction in complexity implied also a reduction in price, and the Honda Insight, being the cheapest hybrid in the market at the time, was the first hybrid model to reach the top selling car in Japan in May 2009. Later the same year, the very strong launch of the third generation Prius reached the first position in total sales for the year of 2009 in Japan. [16, 17]

Other car manufacturers have also placed their bid in the hybrid market. A number of brands, in an attempt to reduce the fuel consumption of their thirstiest models, have developed hybrid systems for SUVs as the Ford Escape, Toyota Highlander and Lexus 400h/450h in 2005, Saturn Green Line in 2006, Volkswagen Touareg and BMW X6 ActiveHybrid in 2009 [18–22]. Furthermore, the hybrid distinctive is used to increase even further the exclusiveness of the top luxury brands, and nowadays even Ferrari, Porsche, Jaguar or Mercedes-Benz among others offer a hybrid version of their top-end models. [23]

The Electric Rear Wheel Drive (E-RWD) unit is a simple approach for electrification of passenger cars, which can be seen as a parallel hybrid configuration. The main idea consists in keeping the conventional transmission based on the Internal Combustion Engine (ICE) in the front wheels and installing an E-RWD unit to drive the rear wheels instead of the dummy axle of the vehicle. When compared to the current hybrid solutions in the market, the E-RWD approach reduces the integration complexity and number of components, maximizing the commonality with non-hybrid versions of the same vehicle. For these reasons, the E-RWD unit appears as a highly cost effective solution, suitable to be offered as an add-on system to an existing passenger car, with minor modifications in

its original configuration. Despite all these arguments in favor, it was not until the first quarter of 2012 that it first appeared in the market, when the PSA Peugeot-Citroën group launched the Peugeot 3008 Hybrid4, equipped with an electric rear wheel drive unit although without torque vectoring capability [24]. In September 2012, Volvo introduced in Sweden the V60 Plug-In hybrid, also featuring an E-RWD unit. The V60 Plug-In was very much welcomed, and by the end of the year Volvo announced that all the 1000 units initially planned for the European market in 2013 were already sold out. While the Peugeot 3008 Hybrid4 is the first mass production diesel-electric hybrid, the V60 Plug-In is the first diesel-electric plug-in hybrid.

The E-RWD unit can be implemented in many different ways; the most significant ones for a passenger car application are represented in Figure 2.1 below. Torque vectoring, i.e. the ability to split the torque between the right and left wheel in a controlled way, is a desired characteristic of the E-RWD system. The need for gears will depend on the machine design. Clutches are needed in case the electrical machines have to be mechanically disconnected from the wheels.
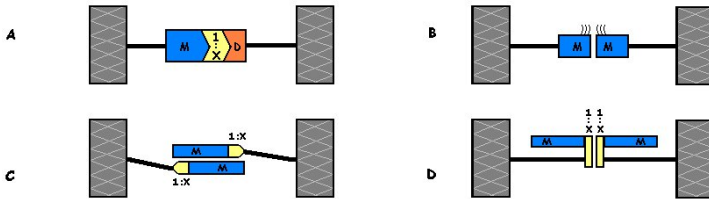
Figure 2.1: System layout for E-RWD unit.

Alternative A in Figure 2.1 consists in a single traction machine, plus a reduction gear and a differential device in order to split the torque between the left and the right wheels, while alternatives B, C and D are two-machine approaches. In B the electrical machines are directly connected to the wheels (they could be in-wheel machines); C and D include a gearbox. The E-RWD unit should be installed with minor modifications in the vehicle, therefore in-wheel machines are not considered. Due to the limited space available, alternative A is preferred and the use of a clutch is also discarded. However, in order to provide torque vectoring the conventional differential device in Figure 2.2a is replaced by two planetary gears -one at each side of the traction machine- with a cross shaft and an auxiliary electric motor as shown in Figure

2.2b.
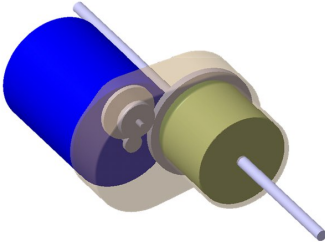
(a) Single machine and differential
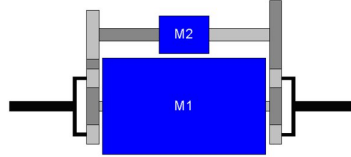
(b) Single machine with planetary gears

Figure 2.2: Single electric traction machine approach.

A system like the one presented results in a very compact unit, hence it can be installed in an existing passenger car with only minor modifications, providing the well known advantages of electric hybridization (reduction of fuel consumption and emissions) and enhancing the performance of the vehicle due to the extra power and the torque vectoring capability.

2.2 Technical specifications

2.2.1 Packing constrains

As mentioned earlier, the E-RWD unit is conceived as an add-on to an existing passenger car, and therefore it should be possible to install it without major modifications of the vehicle. As a consequence, the physical size of the E-RWD unit is one of the most restrictive design requirements, and the resulting size of the traction machine is dependent on both the total size of the unit and the degree of integration achieved. The E-RWD unit should be installed into a Saab 93, slightly smaller in size than the initially considered Volvo V70, which, together with the integration of the planetary gears and the rest of components, implies a reduction of the volume available for the electric traction machine from a $250\,mm$ diameter, $200\,mm$ length cylinder at the beginning of the project to a final $214\,mm$ diameter, $160\,mm$ length cylinder as available volume for the electrical machine including end windings but not shields, bearings, mechanical supports, etc. Figure 2.3 shows an integration study performed by former Haldex Traction.
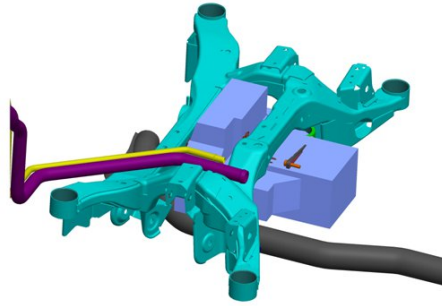
Figure 2.3: Unit packing in the vehicle subframe. The blue block represents the volume available for the E-RWD unit.

2.2.2 Cooling conditions

The E-RWD unit is intended to be air cooled, thus avoiding the need of an external cooling circuit, therefore natural convection is assumed for the design. Nevertheless, taking full advantage of the prototyping possibilities available, two other cooling alternatives are also considered: epoxy encapsulation of the end windings and oil spray cooling of the end windings. However, only the natural convection cooled machine is analyzed in this work. Nonetheless, the experience gained during the experimental tests performed on the other two alternatives opens new research lines for future projects.

2.2.3 Supply and load conditions

Since there is no clutch, the electrical machine and the wheels are always connected through the planetary gears. Hence, the electrical machine maximum speed is proportional to the vehicle maximum speed, and the scale factor equals the gear ratio of the planetary gears, in this case 9.6. Assuming a maximum vehicle speed of $150 \, km/h$, and a wheel radius of approximately $250 \, mm$ the machine should be able to operate at least up to $15000 \, rpm$.

Due to the characteristics of the battery pack available and the absence of a DC/DC converter, the DC-Link voltage for the drive is set to $300 \, V$.

Although in the beginning of the design phase the objective was to maximize the torque and power output in nominal operation, as the project progresses and the E-RWD unit concept matures, the peak torque stands out as an important requirement for this application. A new peak torque requirement derived from the vehicle dynamics analysis performed by former Haldex Traction is

introduced aiming for $100\,Nm$. Equipped with the E-RWD unit, the vehicle performs as a Parallel Hybrid Electric Vehicle, with the ICE providing most of the stationary power and the electric traction machine taking care of the transients, filling in when boost power is needed or feeding the braking energy back to the battery. Therefore, the electrical machine is loaded with high dynamics, hence defining a continuous power or torque level is a difficult task. Nevertheless, the continuous current loading for natural convection cooling of the unit, defined as the current loading that can be sustained indefinitely without overheating the machine, is initially assumed to $6.5\,A/mm^2$ (peak current density value in the winding conductors) based on previous design experiences. This assumption is later confirmed both by means of a detailed thermal model of the machine as well as experimental measurements.

Finally, the efficiency of the unit should be maximized in order to achieve the maximum reduction of fuel consumption and emissions, while keeping the overall cost of the unit as low as possible.

2.2.4   Summary of technical specifications

Table 2.1 collects all the technical specifications provided. Although it is shown in the following chapters that this is not the optimal set of specifications, these are actually the only requirements placed on the machine design at this stage.

Table 2.1: Summary of technical specifications.

L_{tot}	Total available length (mm)	160.0
d_{so}	Outer stator diameter (mm)	214.0
n_{max}	Maximum mechanical speed (rpm)	15000
U_{dc}	DC link voltage (V)	300
J_{nom}	Nominal current loading (peak value) in the conductors (A/mm^2)	6.5
T_{max}	Peak torque (not continuously) (Nm)	100
Cooling principle: Natural convection on the outer surface		

2.3   Machine type selection

An electrical machine can be defined as a device that transforms electrical energy into mechanical energy or vice versa. Such an open definition encloses

a large variety of devices differing not only in their physical shape and size, but also on their capabilities, the nature of the produced movement and their operation principle.

Linear machines are not suitable for the E-RWD application as it has been presented in Figure 2.2, and therefore will not be considered in the following discussion. Among rotary machines, two large groups are usually distinguished depending upon the supplied currents: DC (Direct Current) and AC (Alternating Current) machines. Being older and simpler in both its working principle and control, the DC machine is generally speaking larger, heavier and less efficient than the AC one. AC machines can be classified according to the relationship between the rotational speed of the rotor and the frequency of the induced magnetic field in synchronous or asynchronous (also called induction) machines. In the synchronous AC machine, the rotor spins with the same frequency as the alternating magnetic field (or a sub-multiple of it depending on the number of pole pairs) while in the asynchronous one the mechanical and the electrical frequencies differ, and actually it is this difference that induces a magnetic field in the rotor which is responsible for the movement.

Moreover, the synchronous AC machines can be further classified according to the physical principle originating the magnetic forces responsible for the mechanical movement. In this way, Permanent Magnetized Synchronous Machines (PMSM) have permanent magnets in the rotor and the movement is a consequence of the interaction between the magnetic field originated from the rotor magnets and the magnetic field originated from the stator coils; Electrically Magnetized Synchronous Machines (EMSM) present a wound rotor so the rotor magnetization originates from an electromagnet, and Reluctance Machines do not have a magnetic field source in the rotor and use the saliency in the rotor (difference in magnetic reluctance) to create the movement, in the same way as a ferromagnetic needle will align with an external magnetic field.

Each of the machine types mentioned exhibit certain characteristics that makes it suitable for one or another application. In order to select the best candidate for the EWRD application a Machine Selection Matrix is proposed, comparing Permanent Magnet Synchronous Machine (PMSM), Switched Reluctance Machine (SRM), Synchronous Reluctance Machine (SynRM), Induction Machine (IM), Electrically Magnetized Synchronous Machine (EMSM) and Direct Current Machine (DCM) [25]. The most relevant characteristics of an electrical machine are listed in the matrix rows. Each of these characteristics is assigned a weight according to their relevance for the application. The weight assigned to the different characteristics is decided by the industrial project partners. Besides, each machine type considered is assigned a column

in the matrix, and it is graded between 0 (poor) and 5 (excellent) for each of the characteristics listed. The final score for each machine type is obtained multiplying its grade for each characteristic times the corresponding weight and then adding for all the characteristics listed. The resultant matrix is shown in Figure 2.4.

According to the selection matrix, the PMSM appears as the best candidate for the application. However, in order to broaden the scope of the project it is decided to investigate the capabilities of the SynRM due to its appealing characteristics, especially its robust construction, easy and cost effective manufacturing and the lack of permanent magnet material in the rotor, which yields to a reduction of the machine cost and no need for field weakening over base speed. Therefore, a complete PMSM plus a SynRM rotor suitable to be tested in the PMSM stator will be designed, manufactured and tested.

Property:	PMSM	SRM	SynRM	IM	DCM	EMSM	Weight
Cost (incl electronics)	2	4	4	4	3	4	5
Weight	5	4	4	4	3	3	5
Size	5	4	4	4	3	4	4
Inertia	4	5	4	4	3	4	3
Acoustic noise level	4	2	4	4	4	4	5
Electric noise level	5	3	4	4	3	4	3
Response time	5	5	4	5	5	5	3
Control accuracy	5	4	4	4	4	5	3
Torque	5	4	3	4	4	4	3
Efficiency	5	4	4	4	2	4	4
Power	5	3	3	3	2	4	4
Speed range	4	5	5	5	3	5	4
Fail safety	3	5	5	5	5	5	4
Drag torque	4	4	4	4	4	4	3
Complexity of electronics	4	4	4	4	5	3	3
Complexity of software	4	3	3	3	5	3	3
Cooling capabilities	5	4	4	3	3	3	4
Temperature restistance	3	4	4	4	4	4	4
Maintenance	4	4	4	4	2	3	2
Technical risk	5	4	4	5	5	4	2
Total score	301	278	282	286	251	281	

Figure 2.4: Machine Selection Matrix.

2.4 PMSM Electromagnetic design and optimization

2.4.1 Geometry description

The first design alternative for the electric traction machine is a radial flux electrical machine, in which both the rotor and stator ferromagnetic cores are made of laminated electrical steel. The lamination plane is perpendicular to the machine axial direction, and since most of the magnetic flux moves along the lamination plane, the problem can be tackled with the 2D design tools described in Appendix B and [26].

A first literature review in order to find a PMSM geometry featuring high torque and power density, together with a wide constant power region (since the maximum required speed is relatively high) leads to interior permanent magnet machines (IPMSM). Moreover, v-shape IPMSM, with a high contribution of the reluctance torque to the final torque production, seems to be a good candidate [25, 27–32]. The geometry proposed by the Toshiba corporation in [32], with improved efficiency in the field weakening region is taken as starting point for the design, and will be further modified to fulfill the technical requirements.

The parametrized rotor geometry is shown in Figure 2.5. Gray color represents laminated steel while light red corresponds to permanent magnet material. The different geometric parameters shown in the figure are also listed in Table 2.2. Those under *Input parameters* can be set by the machine designer, while those under *Calculated parameters* come as a result of the geometric calculations based on the input parameters.

Table 2.2: Rotor geometric parameters.

Input parameters:

N_p	Number of poles $(-)$.
r_{ri}	Inner rotor radius (m).
r_{ro}	Outer rotor radius (m).
K_1	Portion of the pole pitch occupied by magnets $(-)$.
K_2	Placement and size of the circular flux barrier $(-)$.
K_3	Placement and size of the magnets $(-)$.
K_4	Size of the triangular flux barrier $(-)$.
d_1	Distance from the magnet flux barrier to the outer rotor surface (m).

d_2 Definition of the magnets placement box (m).

d_r Half width of the iron bridge between two contiguous flux barriers (m).

h_m Permanent magnet thickness (m).

Calculated parameters:

r_1 Placement of the circular flux barrier $r_1 = r_i + K_2(r_o - r_i)$ (m).

r_2 Placement of the magnet flux barrier $r_2 = r_o - d_2$ (m).

r_3 Placement of the magnet flux barrier $r_3 = r_o - d_1$ (m).

r_{hl} Radius of the circular flux barrier $r_{hl} = K_2 (r_o - r_i) / 2$ (m).

α Angular pitch of the magnets $\alpha = K_1 \pi / N_p$ (rad).

d_3 Placement of the magnets (calculated iteratively to fit a magnet with the desired width inside a predefined box) (m).

d_4 Size of the triangular flux barrier $d_4 = K_4 d_3$ (m).

Figure 2.5: Parametrized geometry of a v-shape IPMSM rotor.

Correspondingly, the parametrized stator geometry is shown in Figure 2.6 and its geometric parameters listed in Table 2.3.

Table 2.3: Stator geometric parameters.

r_{si}	Inner stator radius (m).
r_{so}	Outer stator radius (m).
K_y	Stator yoke depth factor $K_y = a\,/\,b$ $(-)$.
K_s	Stator slotting factor $K_s = \alpha\,/\,\delta$ $(-)$.
K_{so}	Slot opening factor. $K_{so} = \beta\,/\,\gamma$ $(-)$.
K_{st}	Tooth tip aspect ratio factor $K_{st} = c\,/\,d$ $(-)$.

(a) Stator geometry parameters.   **(b)** Tooth-tip details.
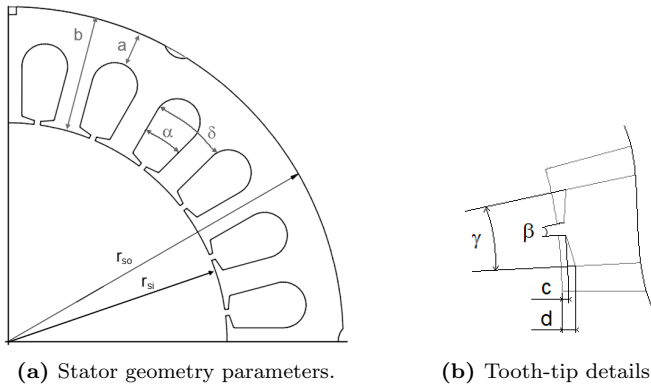
Figure 2.6: Parametrized geometry of the stator.

2.4.2   Design roadmap

The design process is started despite the lack of a comprehensive and definitive set of specifications (as it is discussed already, this is one of the main challenges for a traction machine designer within the automotive industry). As a direct consequence, the design activities are affected by the updates of the technical and physical requirements by the different actors in the project.

The next figure presents the time evolution of the design process, as it changes with the specifications updates. It aims to help the reader understand the different design steps presented in the rest of this chapter, serving as a sort of guide or roadmap towards the final design.
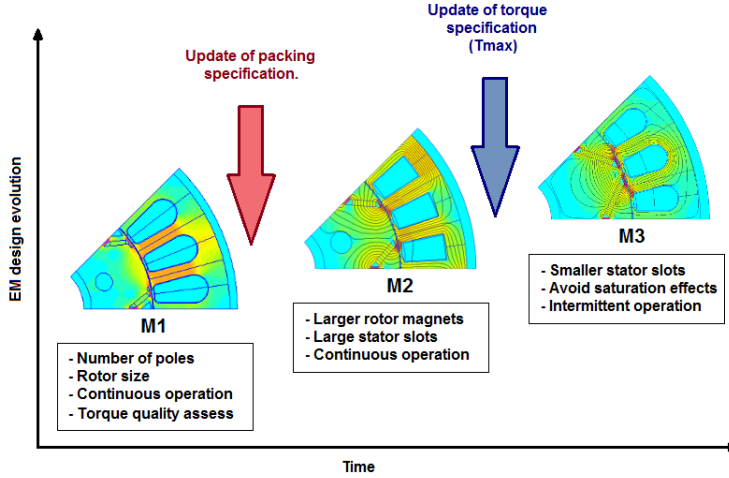
Figure 2.7: Time evolution of the design process.

Each machine geometry considered is analyzed both thermally and electro-magnetically in order to obtain its torque and flux characteristics. These maps are subsequently processed to foresee the machine operation as described in Appendix B and [26].

Looking at Figure 2.7, first a batch of simulations is conducted on the geometry M1 in order to investigate several basic parameters of the machine, such as the number of poles and the ratio between the rotor and the stator diameter. From this first simulations the number of poles is set to 8 (4 pole pairs). A higher number of poles would imply a higher electrical frequency, which requires higher switching frequency of the power electronic modules in order to control the current. An 8-pole machine is proposed as a trade off between the torque output of the machine and the maximum allowed electrical frequency, which is easily calculated from (2.1), and for a maximum machine speed of $15000\,rpm$ yields $1\,kHz$.

$$f_{el} = \frac{n\ N_p}{120} \tag{2.1}$$

Although a larger rotor diameter would in principle lead to a higher output torque, it is also true that if the outer machine diameter is constrained, a larger rotor diameter implies a thinner stator, and therefore less room for the stator windings. From the first simulations conducted, the ratio between the rotor and the stator outer diameter is set to 0.65 in order to maximize the output

torque, which is in accordance with [33]. It is worth remembering that the physical dimensions of the machine are updated along the design period, and therefore the results obtained for a certain size need to be verified for the new requirements, and some of these design parameters may need to be updated.

2.4.3   Torque quality analysis

A passenger car is a large and heavy mechanical system, which is not very likely affected by the torque ripple of the electrical machine in normal operation. In fact, the quality of the torque supplied by the ICE is, generally speaking, worse than that of an electric drive unit. However, at low speeds and high torque operation, the ripple on the output torque of the traction machine can be noticeable, influencing the comfort feeling of the passengers. Moreover, a high torque ripple will affect the lifespan of the gears and the rest of the mechanical transmission components. For these reasons, it is desired to reduce the torque ripple levels, keeping in mind that the average output torque should not be decreased. Starting from the size constrains of M1, several simulations are conducted, evaluating the influence of several geometric parameters in the torque quality, while the rest of parameters are kept unchanged for the sake of comparison. The investigated parameters are K_{so} -slot opening factor- and K_{st} -tooth tip aspect ratio- in the stator and K_4 -size of the triangular flux barrier- in the rotor (please refer to Figures 2.5 and 2.6).

The effect of the rotor and stator geometries in the output torque is compiled in Tables 2.4 and 2.5 respectively. The geometric parameters are dimensionless. All torque values are in Nm.

Table 2.4: Influence of the rotor geometry on the torque ripple.

K_4	$T_n \pm \Delta T$	$\pm \Delta T$ (@ 0A)
0.00	78 ±17.9	±1.5
0.25	78 ±18.2	±1.5
0.50	76 ±21.9	±2.6
0.66	74 ±25.9	±3.0
0.75	74 ±27.4	±1.9

From Table 2.4 it is clear that the triangular flux barrier in the rotor does not contribute to the torque production, moreover, the larger the barrier is, the higher the torque ripple becomes. Therefore it is decided to remove this flux barrier from the rotor, i.e., set K_4 to 0.

Table 2.5: Influence of the stator geometry on the torque ripple.

K_{so}; K_{st}	$T_n \pm \Delta T$	$\pm \Delta T$ (@ $0A$)
0.15; 0.30	76 ±24.8	±4.1
0.15; 0.40	76 ±24.8	±4.1
0.15; 0.50	76 ±24.8	±4.1
0.15; 0.60	76 ±24.8	±4.1
0.30; 0.30	76 ±28.2	±12.3
0.30; 0.40	76 ±28.2	±12.3
0.30; 0.50	76 ±28.2	±12.3
0.30; 0.60	76 ±28.2	±12.3
0.45; 0.30	76 ±31.0	±22.0
0.45; 0.40	76 ±31.0	±22.0
0.45; 0.50	76 ±31.0	±22.0
0.45; 0.60	76 ±31.0	±22.0
0.60; 0.30	74 ±31.5	±27.9
0.60; 0.40	74 ±31.5	±27.9
0.60; 0.50	74 ±31.5	±27.9
0.60; 0.60	74 ±31.5	±27.9

From Table 2.5 it can be deduced that the torque ripple decreases as the slot opening factor decreases, while the tooth tip aspect ratio has no significant influence on it. The slot opening is limited by the manufacturing process, and it has to be sufficient to allow for insertion of the windings of the machine. Based on the manufacturing experience from BEVI AB [34], a slot opening of $2\,mm$ is acceptable. The tooth tip aspect ratio is set to 0.5.

Figure 2.8 shows the most significant results from the Finite Element (FE) simulation for the final combination: $K_{so} = 0.15$, $K_{st} = 0.50$ and $K_4 = 0$. The torque-speed diagram together with a preliminary efficiency map is presented in the top left; the input power (blue), output power (black), copper losses (green) and iron losses (red) vs. speed are in the top right plot; the torque ripple at no load is shown in the bottom left and the torque ripple at nominal load is shown in the bottom left graph. Please refer to Appendix B and [26] for further details on the machine characteristics calculation process.

It is worth mentioning that the conclusions from this torque quality assessment are also valid for the subsequent geometries analyzed, despite the size reduction experienced.
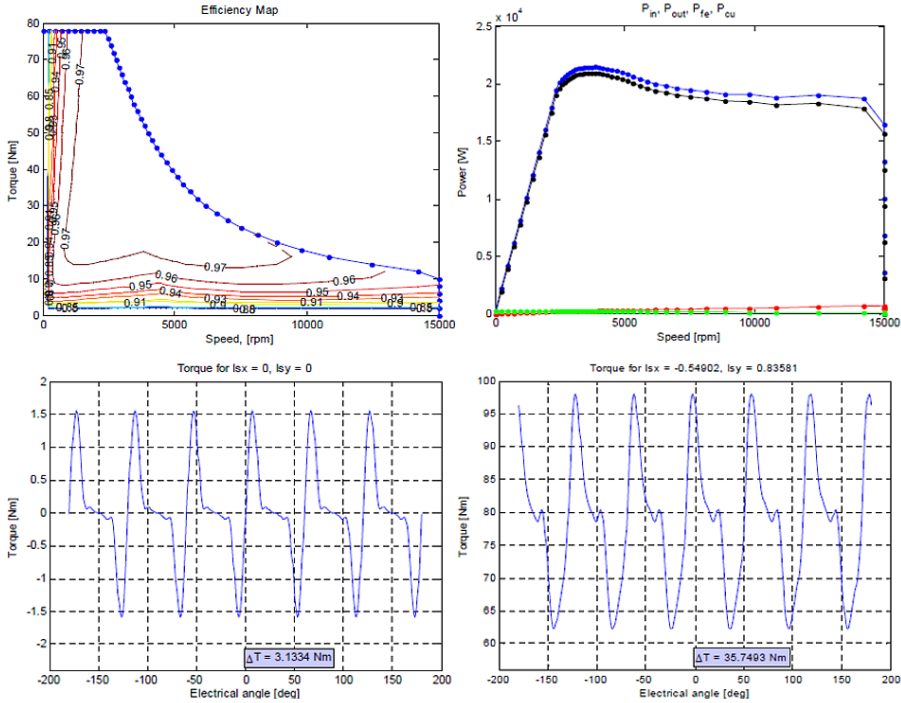
Figure 2.8: FE simulation results for the torque ripple optimized machine.

2.4.4 Geometry optimization in continuous operation

At this point in the design, the mechanical design of the E-RWD unit, housing and mechanical transmission, is nearly completed and as a consequence the physical volume available for the traction machine is updated (marked with a red interaction arrow in Figure 2.7 between machine geometries M1 and M2). After this change, the outer dimensions of the machine M2 are $214\,mm$ diameter and $160\,mm$ length including end windings, as stated in section 2.2 which are the final size specifications. Since the new specifications imply a reduction of the machine available volume, it comes necessary to modify the previous geometry design (based on the size constrains for M1) in order to

fulfill the torque and power requirements. The geometry optimization is carried
out in two stages, the first one focusing on the continuous output torque of
the machine and the second one aiming to improve the peak torque performance.

First, both rotor and stator geometries are optimized in order to maximize
the continuous output torque, i.e., the torque that can be delivered indefinitely
without overheating the machine. The continuous current loading of the
machine is determined by iterative FE thermal simulations, so that the hot-
spot temperature does not exceed the maximum temperature specification of
150 °C. However, due to the 2D nature of the FE model used, convection is only
considered over the outer area corresponding to the machine's active length, and
therefore the continuous current loading resulting from the simulations assuming
typical values of the convection coefficient is underestimated ($3.82 \ A/mm^2$
for $h_{ca} = 15 \ W/(m^2 K)$). Despite this, the comparison between the different
geometries is still possible, and the conclusions obtained here are valid for
higher current loading as well.

Both the stator and rotor geometries are analyzed at this stage. Regarding
the stator, the parameters of interest are the slotting factor K_s and the back
yoke depth factor K_y, both defined in Table 2.3. The rotor geometry is
somewhat different from the one in Figure 2.5. The triangular flux barrier is
suppressed in order to reduce the output torque ripple as motivated before, and
the circular flux barrier is also eliminated to allow for a larger diameter shaft.
Since the available volume for the electrical machine is significantly smaller
than initially considered, larger magnets are needed in order to meet the peak
torque requirements. The flux barriers beside the magnets are reshaped to
give room to the larger magnets. For the rotor geometry, the parameters of
interest are K_1 defining the ratio of the angular span covered by magnets and
K_3 characterizing the radial proportion occupied by magnets. For the sake of
clarity, all parameters involved at this stage are listed below.

Stator parameters (see Figure 2.6a):

r_{si} Inner stator radius (m).

r_{so} Outer stator radius (m).

K_y Stator yoke depth factor $K_y = a \, / \, b \quad (-)$.

K_s Stator slotting factor $K_s = \alpha \, / \, \delta \quad (-)$.

Rotor parameters (see Figure 2.9b):

r_{ri} Inner rotor radius (m).

r_{ro} Outer rotor radius (m).

K_1 Portion of the pole pitch occupied by magnets $(-)$.

K_3 Placement and size of the magnets $(-)$.

d_1 Distance from the magnet flux barrier to the outer rotor surface (m).

d_r Half width of the iron bridge between two contiguous flux barriers (m).

α Angular pitch of the magnets $\alpha = K_1 \pi / N_p$ (rad).

h_m Permanent magnet thickness (m).

(a) Stator geometry parameters.

(b) Rotor geometry parameters.
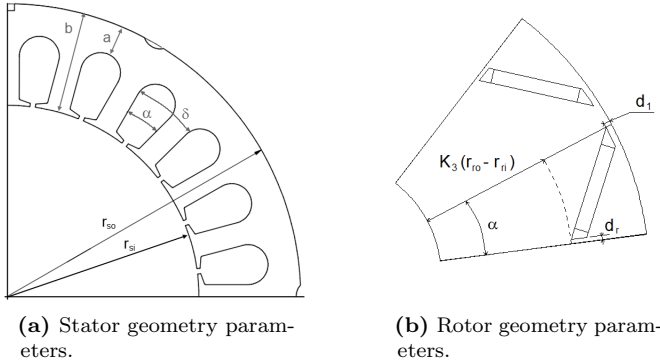
Figure 2.9: Geometric parameters evaluated in the machine optimization.

Stator geometry optimization in continuous operation

In order to analyze the influence of the stator parameters in the performance of the machine, several simulations are conducted for different values of K_s and K_y for different rotor sizes (r_g denotes the airgap radius and r_{so} the outer stator radius), while the rest of the geometry remains unchanged. The rotor geometry in this study is characterized by $K_1 = 0.65$ and $K_3 = 0.625$. Torque and power values in continuous operation resulting from these simulations are presented in Table 2.6 ($T_n\,(Nm)/P_n\,(kW)$).

From Table 2.6 it is clear that the highest torque ($26\,Nm$) is obtained for an air-gap to outer diameter ratio of 0.68, $K_s = 0.6$ and $K_y = 0.3$ (shadowed in red). However, when both the maximum power and the field weakening capabilities are taken into account, the alternative with $r_g / r_{so} = 0.65$, $K_s = 0.7$

and $K_y = 0.3$ (shadowed in green) is a better combination at this stage, since it is capable of delivering higher constant power up to the maximum speed. Figure 2.10 shows the power vs. speed curves obtained from FE simulations.

Table 2.6: T_n *(Nm) / P_n (kW) for continuous operation for different stator geometry combinations with $K_1 = 0.65$ and $K_3 = 0.625$.*
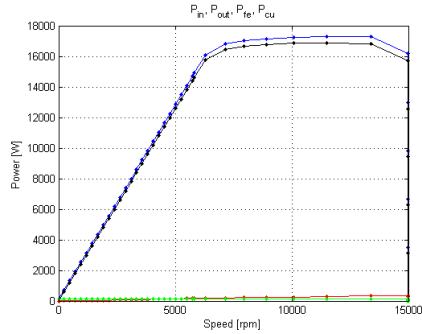
		$K_s = 0.5$	$K_s = 0.6$	$K_s = 0.7$
$r_g/r_{so} = 0.60$	$K_y = 0.3$	22/14.4	22/15.4	22/15.9
	$K_y = 0.4$	20/13.1	20/14.0	20/15.1
$r_g/r_{so} = 0.65$	$K_y = 0.3$	24/14.0	24/15.2	24/16.3
	$K_y = 0.4$	22/12.7	22/13.2	20/14.7
$r_g/r_{so} = 0.68$	$K_y = 0.3$	24/13.7	26/14.5	24/15.5
	$K_y = 0.4$	22/12.1	22/13.3	22/13.9
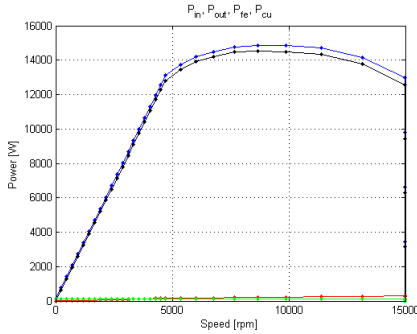
(a) $r_g / r_{so} = 0.68$, $K_s = 0.6$, $K_y = 0.3$ **(b)** $r_g / r_{so} = 0.65$, $K_s = 0.7$, $K_y = 0.3$

Figure 2.10: Power vs. speed curves for stator optimized geometries in continuous operation.

Rotor geometry optimization in continuous operation

In parallel with the stator optimization, several rotor geometries are simulated in order to evaluate the influence of the magnets' size and position in the output torque. Different values of the geometric parameters K_1 and K_3 are considered, while the rest of the geometry remains unchanged. The air-gap to

outer diameter ratio is kept constant at 0.65 and the slotting factor $K_s = 0.5$. Besides, two different values of the stator back-yoke depth factor are considered, $K_y = 0.25$ and $K_y = 0.30$, since larger magnets could lead to saturation in the stator yoke. The torque and the power values in continuous operation resulting from these simulations are presented in Table 2.7 ($Tn(Nm)/Pn(kW)$).

From Table 2.7, the best results in terms of torque and power for continuous operation appear for $K_y = 0.25$, $K_1 = 0.75$ and $K_3 = 0.06$ (shadowed in red). This makes sense when compared to the results of the previous designs. The magnet size is increased with respect to the previous proposals, and naturally, the larger the magnets, the higher the output torque. However, the constant power operation region is clearly affected when K_1 increases from 0.65 to 0.75, and therefore the alternative with $K_y = 0.25$, $K_1 = 0.65$ and $K_3 = 0.60$ (shadowed in green) is preferred. Figure 2.11 shows the power vs. speed characteristic for both alternatives.

Table 2.7: T_n (Nm) / P_n (kW) for continuous operation for different rotor geometry combinations with $K_s = 0.50$ and $r_g/r_{so}=0.65$.

		$K_3 = 0.600$	$K_3 = 0.625$	$K_3 = 0.650$
	$K_1 = 0.60$	24/14.9	22/14.5	22/14.2
$K_y = 0.25$	$K_1 = 0.65$	24/15.2	24/15.2	24/14.9
	$K_1 = 0.75$	28/14.6	26/15.1	26/14.6
	$K_1 = 0.60$	24/13.9	22/13.9	22/13.5
$K_y = 0.30$	$K_1 = 0.65$	24/13.9	24/14.0	24/14.1
	$K_1 = 0.75$	28/13.9	26/13.3	26/13.7

Analyzing the results presented above for both stator and rotor geometry optimizations, it is worth noticing that the best results in continuous operation are obtained for those geometries with the largest slot area. Larger slot area means more current in the windings assuming a constant current density loading, which in turns implies a higher output torque as long as the machine is not saturated. Consequently, it is the natural cooling capability and the core ability to carry magnetic flux what defines the stator geometry. Regarding the rotor, it can be seen that the larger the magnets, the larger the output torque obtained from the machine. However, there is a limitation in the magnet size besides the obvious physical room available: large magnets create a high magnetic flux linkage in the windings, which leads to higher field weakening current needs. Since the continuous current loading is fixed, the machine may not be able to keep a constant power over base speed, or even worse, it may
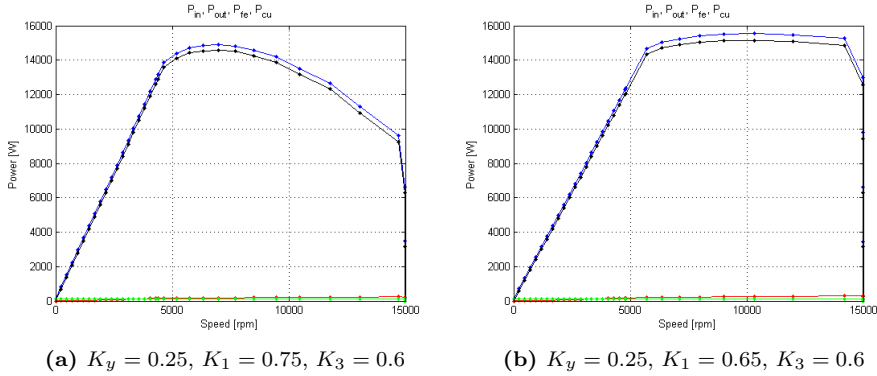
not meet the maximum speed specification.

(a) $K_y = 0.25$, $K_1 = 0.75$, $K_3 = 0.6$ **(b)** $K_y = 0.25$, $K_1 = 0.65$, $K_3 = 0.6$

Figure 2.11: Power vs. speed curves for rotor optimized geometries in continuous operation.

2.4.5   Distributed vs. concentrated windings

When analyzing the volume of the machine presented in the previous section, it appears that nearly half of the total length corresponds to the end windings. Hence, shortening the end windings implies an increase of the active length of the machine, which could lead to an increased output torque.

A change in the stator configuration in order to use concentrated instead of distributed windings is now proposed as a way to shorten the length of the end windings. Concentrated non-overlapping windings are extensively used in small electrical machines due to their short end windings and simple structure, suitable for high volume automated mass production. When compared to single layer, 1 slot per pole and phase windings, a reduction of the end winding length up to 2 times can be achieved for single layer concentrated windings, while for double layer concentrated windings it can increase up to 4 times. Besides, concentrated windings can be manufactured with higher slot fill factor than distributed windings, increasing the copper cross sectional area inside the slot hence reducing the current density and the resistive losses for a given stator current [35–37].

On the other hand, when it comes to larger machines where efficiency and smooth output torque play an important role, a distributed winding is preferred. Concentrated winding machines traditionally suffer from a low

fundamental winding factor, which leads to a higher current need for the same output torque and therefore increased copper losses, i.e. lower efficiency. Besides, the quality of the output torque is usually worse than for distributed winding machines, with a higher cogging torque and torque ripple. However, several studies suggest that with the appropriate choice of number of slots and poles both problems can be significantly mitigated. Winding factors over 0.9 are attainable for machines with more than 8 poles, both with single and double layer concentrated windings, and values as high as 10 times cogging torque reduction are reported [36–38]. When compared to distributed windings, concentrated windings create a magnetomotive force distribution along the airgap with a much higher harmonic content. Although only the fundamental component of the MMF distribution is involved in torque production, all other harmonics contribute to increase the phase inductance by increasing its harmonic leakage component. As a consequence, the field-weakening range of the machine can be substantially extended. [35]

In order to evaluate the potential of concentrated windings for the E-RWD application, a Plexiglas model of the stator laminations made by BEVI AB is used to estimate the difference in end windings length between the concentrated and distributed winding alternatives. From this model, it is concluded that a reduction of $20\,mm$ at most can be expected, and therefore, the active length of the machine with concentrated windings is set to $100\,mm$ instead of $80\,mm$. A FE model of the concentrated winding alternative with $q = 0.5$ where q is the number of slots per pole and phase, is used to investigate the performance of such a machine for the different geometric parameters (see Figure 2.12).

(a) Example of a Plexiglas model
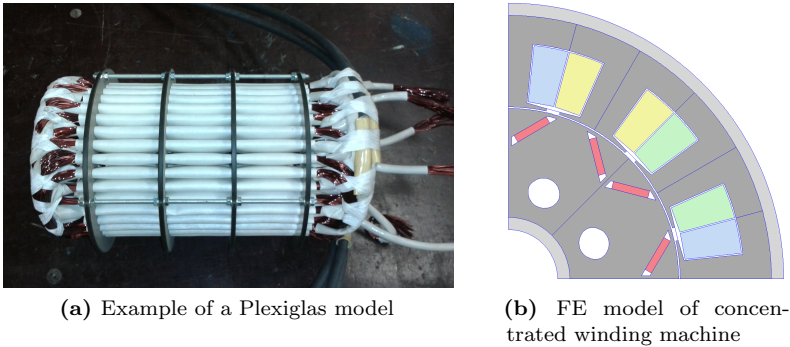
(b) FE model of concentrated winding machine

Figure 2.12: Investigation of the concentrated winding potential.

Several simulations are conducted for different stator geometries, while the rotor remains the same, corresponding to the best result from the previous

section ($K_1 = 0.75$ and $K_3 = 0.65$). In this new simulation batch, several rotor to outer diameter ratios are analyzed, for a combination of slotting factor (K_s) and stator yoke depth factor (K_y). As in previous sections, torque and power values in continuous operation resulting from these simulations are presented in Table 2.8 (Tn (Nm)/Pn (kW)).

Table 2.8: T_n (Nm) / P_n (kW) for continuous operation for different stator geometry combinations with concentrated windings

		$K_s = 0.50$	$K_s = 0.60$	$K_s = 0.65$
r_g/r_{so}=0.60	$K_y = 0.25$	30/16.4	34/19.2	34/20.2
	$K_y = 0.30$	26/15.5	30/18.7	32/19.6
r_g/r_{so}=0.65	$K_y = 0.25$	28/15.9	34/18.3	34/20.0
	$K_y = 0.30$	26/14.9	30/16.5	32/18.3
r_g/r_{so}=0.70	$K_y = 0.25$	26/14.4	30/16.6	32/17.7
	$K_y = 0.30$	26/12.5	30/14.5	30/18.1

Comparing these results with those obtained in Table 2.7, only minor differences are noticed in the torque delivered by two equivalent machines. For example, comparing both designs with $r_g/r_{so} = 0.65$, a stator characterized by $K_s = 0.5$ and $K_y = 0.3$; and a rotor characterized by $K_1 = 0.75$ and $K_3 = 0.65$ it can be seen that both machines produce $26\,Nm$. Based on the simulations made for the distributed winding alternative with different slotting factor values it is concluded that, for this machine size and assuming an end winding reduction of $20\,mm$ as measured from the Plexiglas model, there is no significant advantage in using concentrated windings. A number of slots per pole and phase (q) equals to 3/8 could give a better winding factor, and therefore higher output torque, although the difference in active length with the distributed winding alternative may not be sufficient to create a noticeable effect.

Nevertheless, all previous research work on concentrated windings for traction applications agree, based both on numerical and experimental results, that the high harmonic content on the airgap MMF distribution causes increased magnetic losses both in the stator laminations and most important, in the rotor magnets. Reducing the losses in the permanent magnets is not an easy task. Magnet segmentation, or using bonded instead of sintered magnets are some of the measurements proposed in the literature to that aim, though it is very seldom to find explicit mathematical models to quantify the effect of

the different actions (e.g. what size the magnets should be or what particular geometry is preferred based on the magnetic environment) [27, 28, 36, 37, 39]. In view of the above, the distributed windings stator alternative is preferred for the E-RWD unit traction machine.

2.4.6   Winding configuration

In all the simulation results presented so far it is assumed that every electrical machine considered has the same winding layout, plus that the DC link voltage is constant, in order to have a fair comparison between the different alternatives. Moreover, the windings are modeled as a single current conductor in which a certain current density is applied, taking into account the slot fill factor as well.

In reality, however, this is not the case and the winding consists of a bundle of thin copper wires parallel connected, that are wound around the stator teeth a certain number of turns. There is a limitation on the number of wires that fit inside a slot, usually related to the manufacturing process. This limitation is usually expressed in terms of the slot fill factor. When looking carefully inside the stator slot, three different elements can be found, namely: the slot insulation liner that stays between the stator lamination and the copper wires in order to avoid the formation of electric arc and protects the wires from erosion; the copper wires with their insulation varnish as well as some air in between the copper threads. The ratio between the total copper area and the slot cross-sectional area is called slot fill factor K_f. BEVI, with a wide experience in electric motor manufacturing, advises a maximum slot fill factor of 0.45 to 0.50 for hand wound machines with distributed windings. It is worth noticing that this figure can be remarkably increased with special manufacturing techniques and values as high as 0.84 are reported in the literature for example for the Toyota Prius THS II motor [40].

The total current inside a slot is the product of the number of parallel wires by the number of winding turns and by the current in a single wire. The larger the total slot current, the larger the magneto motive force induced by the winding current, and hence the larger output torque produced. In order to limit the current delivered by the power electronic converter, a high number of winding turns is desired, since the cost of the power switches is proportional to their current capability.

On the other hand, the voltage induced in the stator coils due to the variable magnetic flux linkage created when the rotor magnets spin also increases proportionally to the number of turns. In other words, increasing the number of turns in the winding leads to lower current demand on the power converter

for the same total slot, but lower base speed (and consequently lower maximum speed).

In order to select the most suitable winding setup, the DC link voltage has to be taken into account. From the project technical specifications, the DC link voltage is limited by the battery to $300\,V$, since there is no DC-DC converter included. Besides, the maximum machine current is also limited by the capabilities of the inverter, since the semiconductor devices of the drive should be dimensioned for the peak motor current.

Another relevant aspect of the winding is the shape and size of the copper threads used. Depending upon the slot geometry, either squared or rounded copper wires can be used in order to increase the slot fill factor. Besides, at high frequencies, the electrons tend to move to the surface of the conductor, reducing the effective cross sectional area and therefore increasing the copper losses. This phenomenon, known as skin effect, is reduced by using small diameter wires. On the other hand, since every thread is covered by an insulation varnish layer, the slot fill factor will be reduced when small diameter wires are used, since a larger number of those is needed to carry the same amount of current assuming a constant current density.

Based on the previous considerations, a winding consisting on 16 turns, 17 parallel wires of 0.8 mm diameter with class H insulation (180 ℃ maximum temperature) is proposed. With this configuration, the nominal machine current is $39.3\,A(RMS)$, for a current density loading of $6.5\,A/mm^2$. The resulting slot fill factor is $K_f = 0.454$.

With a DC link voltage of $300\,V$ and series connected windings, the maximum reachable machine voltage in the rotor frame (x,y) calculated according to (2.2) equals $212.13\,V$. Then, the voltage drop per turn in rotor coordinates would be $13.26\,V$. Since the FE model assumes a single turn winding, this is the figure that should be used in the post processing routine in order to determine the base speed.

$$U_{s,max} = \cos\left(\frac{\pi}{6}\right)\ \sqrt{\frac{2}{3}}\ \ U_{DC} \tag{2.2}$$

2.4.7   Geometry optimization for overloading

Subsequent to the presentation and discussion of the simulation results for continuous operation, the focus is shifted to the overloading capabilities of the

machine. A vehicle equipped with the E-RWD unit works as a parallel hybrid, with the ICE delivering most of the average power needed, and the electric unit taking care of the transient loads, filling in when needed or feeding the excess of energy back to the battery when braking or going downhill. Besides, to take full advantage of the torque vectoring capability, the electric traction machine is required to deliver very high torque for a short period of time in order to contribute to vehicle stability when the driving conditions are unfavorable. For all these reasons, the electric traction machine loading profile is highly dynamic, and the peak torque value that the machine is able to deliver becomes very important. Hence, yet another update of the technical specifications is introduced (indicated with a blue interaction arrow in Figure 2.7 between machine geometries M2 and M3): it is strongly recommended that the peak output torque reaches at least $100\,Nm$.

Starting from the results obtained in 2.4.4, this second stage of the geometry optimization focuses on maximizing the peak torque capability of the electric traction machine, without compromising the performance at high speed. As for the previous optimization, both stator and rotor geometries are analyzed.

Stator geometry optimization for overloading

In order to boost the output torque up to the specified value of $100\,Nm$, the stator windings need to be loaded with a higher current than the continuous current rating obtained from the simulations. At such high current levels, magnetic saturation starts to occur in the stator laminations, preventing the torque to increase as desired. Two geometry modifications are investigated in order to avoid saturation in the stator: increasing the back yoke depth and increasing the teeth width. Both actions imply a reduction of the copper area in favor of the iron, broadening the path for the magnetic flux. However, due to the reduced slot area, higher current densities are required in order to keep the same total current loading, which affects the thermal performance of the machine negatively.

Designs with different values of K_s and K_y are simulated, while the rest of the geometry remains unchanged. The rotor geometry in this study is the one obtained in Section 2.4.4 optimized for continuous operation, characterized by $K_1 = 0.65$ and $K_3 = 0.60$.

Table 2.9 presents the torque and power values in continuous operation resulting from these simulations, while Table 2.10 shows the torque delivered by the machine when loaded with the rated continuous current multiplied by a factor of 1, 2, 4 and 6.

Table 2.9: T_n (Nm) / P_n (kW) for continuous operation for different stator geometry combinations. The rotor features $K_1 = 0.65$ and $K_3 = 0.60$.

	$K_s = 0.55$	$K_s = 0.70$
$K_y = 0.3$	28/11.4	28/15.5
$K_y = 0.4$	24/9.6	24/12.6

Table 2.10: T_n (Nm) at 1x, 2x, 4x and 6x the nominal current rating for different stator geometry combinations. The rotor features $K_1 = 0.65$ and $K_3 = 0.60$.

	$K_s = 0.55$				$K_s = 0.70$			
$K_y = 0.3$	28	56	84	98	24	54	76	88
$K_y = 0.4$	24	48	88	108	24	46	72	86

As the current loading of the machine increases, the magnetic flux across the stator lamination also increases, leading to magnetic saturation of the iron if the current is high enough. The saturation effects can be seen in the torque figures shown in Table 2.10. For example, for $K_s = 0.55$ and $K_y = 0.3$, when the machine current loading is doubled, the output torque is also doubled from 28 to 56 Nm, though, when the current is increased by 4 and 6 times, the torque reaches 84 Nm and 98 Nm respectively, i.e, 3 and 3.5 times the torque obtained at rated continuous loading.

From Table 2.9 it is clear that the higher torque and power at nominal load appears for the largest slot area as it is discussed in the previous section, since it allows for a higher continuous current loading of the machine. However, the overloading capabilities of such a machine are not optimal and saturation effects appear for fairly low current values. As suggested before, the highest torque is obtained for the geometry with thickest back yoke and teeth ($K_y = 0.4$, $K_s = 0.55$), which exhibits the lowest saturation effects. However, the combination $K_y = 0.3$, $K_s = 0.55$ gives 98 Nm at 6 times the rated current (thus presumably able to deliver the required 100 Nm) while having larger slot area, and therefore better nominal characteristics.

Figure 2.13 shows the torque multiplication factor when the machine is loaded with 2 (dark green), 4 (light green) and 6 (yellow) times the continuous current rating for the stator geometries considered.
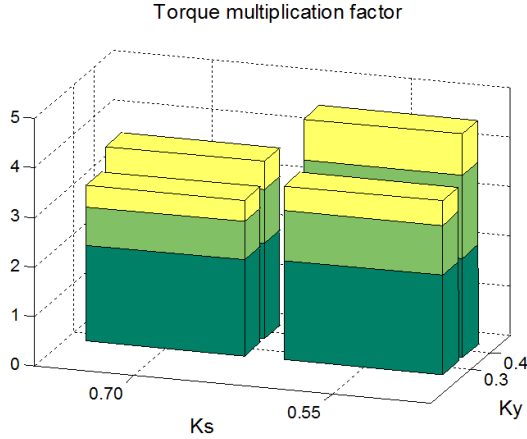
Figure 2.13: Torque multiplication factor for 2 (dark green), 4 (light green) and 6 (yellow) times the continuous current rating.

Rotor geometry optimization for overloading

The rotor geometry is also modified in order to improve the overloading performance of the machine. Two adjustments are considered at this stage in order to fulfill the maximum torque requirement: decreasing the distance between two contiguous magnets (marked as d_r in Figure 2.9b) aiming to increase the reluctance torque contribution, and increasing the magnet size by modifying the angular span covered by magnets (α as a function of K_1 in Figure 2.9b). The rest of the machine geometry remains unchanged in the simulations, corresponding to that obtained in section 2.4.4.

Table 2.11 presents the torque and power values in continuous operation resulting from the simulations, while Table 2.12 shows the torque delivered by the machine (Nm) when loaded with the rated continuous current multiplied by 1, 2, 4 and 6 times. From Tables 2.11 and 2.12 it can be seen that the initial predictions are right, and the output torque increases both with larger magnets (higher K_1) and with less distance between magnets (smaller d_r). However, as mentioned in the previous section, large magnets compromise the field weakening capabilities of the machine at nominal current loading. Besides, high permanent magnet flux linkage reduces the overloading capabilities of the machine at higher speeds [41, 42].

Table 2.11: T_n (Nm) / P_n (kW) for continuous operation for different rotor geometry combinations with $K_y = 0.3$ and $K_s = 0.7$.

	$d_r = 0.7$ mm	$d_r = 1.3$ mm
$K_1 = 0.75$	30/15.4	28/15.5
$K_1 = 0.82$	32/14.9	30/15.0
$K_1 = 0.90$	32/15.3	32/15.3

Table 2.12: T_n (Nm) at 1x, 2x, 4x and 6x the nominal current rating for different rotor geometry combinations with $K_y = 0.3$ and $K_s = 0.70$.

	$d_r = 0.7$ mm				$d_r = 1.3$ mm			
$K_1 = 0.75$	30	56	80	92	28	54	76	88
$K_1 = 0.82$	32	58	84	96	30	56	80	94
$K_1 = 0.90$	32	58	86	100	32	58	84	96

Figure 2.14 shows the torque multiplication factor when the machine is loaded with 2 (dark green), 4 (light green) and 6 (yellow) times the continuous current rating for the different rotor geometries considered.
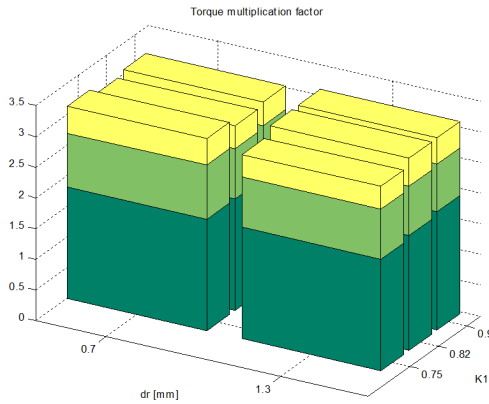

Figure 2.14: Torque multiplication factor for 2 (dark green), 4 (light green) and 6 (yellow) times the continuous current rating.

The optimization of both stator and rotor geometries focusing on the overloading capabilities of the machine is run in parallel, taking the geometry resultant from section 2.4.4 as starting point. Consequently, the only thing left is to merge the conclusions from the previous simulations into a new design and analyze it. Last, a fine tuning of the rotor magnets' size and position is carried out, aiming to reduce the magnets' size as much as possible. The parameters that characterize the final machine design are presented in Table 2.13.

Table 2.13: Final geometry characterization.

Param.	Value	Description
D_{so}	214.0	(mm) Stator outer diameter
D_{si}	139.7	(mm) Stator inner diameter
D_{ro}	138.5	(mm) Rotor outer diameter
D_{ri}	30.0	(mm) Rotor inner diameter
g	0.6	(mm) Airgap length
L_{fe}	80.0	(mm) Active machine length
L_{tot}	160.0	(mm) Total machine length
N_p	8	(-) Number of poles
K_y	0.30	(-) Stator yoke depth factor
K_s	0.55	(-) Stator slotting factor
N_q	24	(-) Number of slots
d_{sl}	2.0	(mm) Slot opening
K_1	0.87	(-) Ratio of the angular span covered by magnets
K_3	0.57	(-) Radial rotor proportion occupied by magnets
d_r	0.9	(mm) Half of the distance between adjacent magnets
d_1	1.3	(mm) Distance between the outer air pocket edge and the rotor end

Comparing the final design presented above with the results of the last optimization stage for overloading capabilities, there are a few differences that are worth noticing. The rotor magnet's size is slightly reduced (K_1 is decreased from 0.90 to 0.87 and K_3 is increased from 0.55 to 0.57). Furthermore, the parameter corresponding to half of the distance between adjacent magnets d_r is increased from $0.7\,mm$ to $0.9\,mm$. It is shown in the previous section

that smaller values of d_r lead to higher output torque, since the reluctance torque contribution is improved. However, the small iron bridges between the magnets are crucial for keeping the structural integrity of the rotor, particularly when the machine operates at high speed. A mechanical FE analysis of the rotor is performed, showing that $d_r = 0.7\,mm$ is not enough to guarantee the structural strength of the rotor when exposed to the maximum speed (assuming a safety factor of 50%), and an updated value of $0.9\,mm$ is suggested. The final drawings of the resulting rotor and stator geometries are found in Appendix A.

Although all the geometries simulated so far feature rectangular stator slots, several other alternatives are possible. Figure 2.15 shows the different slot shapes implemented in the Matlab design program. Based on BEVI's expertise, alternative 2 is preferred for a number of reasons, among which are the absence of sharp corners that make the thermal contact between the winding insulation paper and the stator laminations difficult, and the potential to reach higher fill factor with round copper conductors. The slot cross sectional area is kept constant.
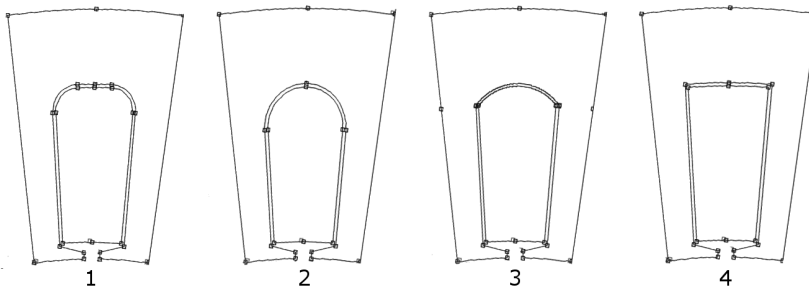

Figure 2.15: Different slot shapes implemented in the design program.

Figure 2.16 presents the most significant results obtained from the Finite Element simulation of the proposed geometry, namely the torque map (top left), the flux linkage map (top right), the efficiency map (bottom left) and the power characteristics (bottom right) where the input power (blue), the output power (black), the winding copper losses (green) and the stator core iron losses (red) are plotted. In order to compute the efficiency, the simulation model takes into account just copper losses in the windings and iron losses in the stator core of the machine. The iron losses in the rotor core and permanent magnets as well as mechanical friction and windage losses are neglected at this stage. Please refer to Appendix B and [26] for further details on the machine characteristics calculation process.

When looking at the power characteristics of the optimized machine, it is clear that the machine is not able to keep a constant power over base speed for the nominal current rating (compare the power characteristics in Figure 2.16 to that one on Figures 2.10b and 2.11b) . Why is it then selected as the best alternative, if the high speed performance is one of the most important design specifications? The reason is that at the time the optimization was performed, the voltage drop per turn (used in the post processing program) was miscalculated in the software, and the results showed a wider constant power region. The results presented in Figure 2.16 correspond to the optimized geometry, after the correction of this error. However, the manufacturing of the prototype started before the error was discovered, and therefore the prototype is built according to the geometry described in Table 2.13 although its simulated high speed performance is not optimal.
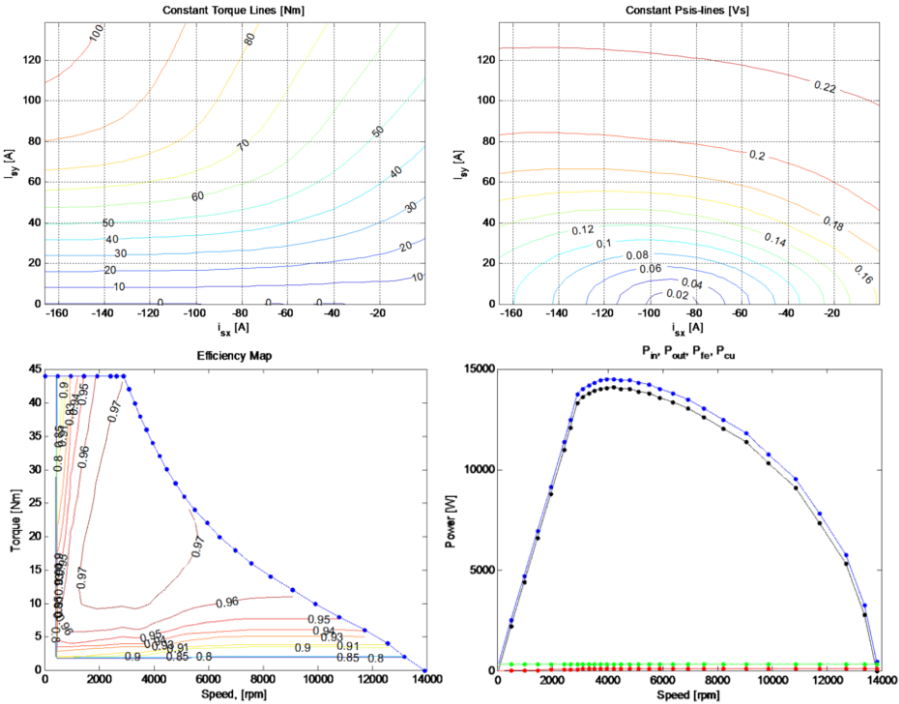

Figure 2.16: FE simulation results for the final geometry selected.

The prototype machine is manufactured with a double aim: validate the machine design software tool and demonstrate the functionality of the whole E-RWD unit both in a test setup and onboard the vehicle. However, during the testing of the prototype, the experimentally obtained torque vs. speed characteristic does not fully match the one presented in Figure 2.16, therefore some improvements are introduced in the simulation model.

The manufacturing of the prototype, as well as the comparison between experimental and simulated results for the improved model and a description of the model upgrading are detailed in section 2.5.

2.5 PMSM Prototyping and experimental testing

A prototype of the final machine design resulting from the optimization process is manufactured with two main aims: to test the functionality of the complete E-RWD unit and to validate the design tool developed. For the software validation, the machine is mounted in a separate test bench in order to characterize its performance and evaluate the efficiency of the stand-alone machine.

The rotor and stator laminations are cut by a CO_2 laser at LCD LaserCut AG (Densbüren, Switzerland) instead of punched, due to the limited number of units produced. Surahammars Bruk SURA M250-35A ($0.35\,mm$ thick with maximum loss of $2.50\,W/kg$ at $1.5\,T$ and $50\,Hz$) electrical steel is used [43]. A comparative study is performed at Surahammars Bruk in which the magnetic properties of the laser cut steel are compared to those of the conventional sheared steel. For this study, 12 normal Epstein strips ($305\,\times\,30\,mm$) are sheared in the longitudinal (rolling) direction and 12 in the transverse direction from the steel coil both before and after the coil section used for the machine laminations. LCD also provided $12 + 12$ Epstein strips cut with the same CO_2 laser used for the machine laminations. Testing of the Epstein samples was performed at Cogent Surahammars Bruk using a PMS 3000 instrument and according to EN 60404-2.

The results from the study are presented in Table 2.14. Shears 1 refers to the first steel sheet cut for the prototype manufacturing and Shears 2 to the last. From Table 2.14 it can be seen that the difference between these samples is very small, and hardly significant in view of the uncertainty of the test method. This indicates that there is almost no variation of the magnetic properties along the length of the coil. On the other hand, the laser cut samples

have higher losses at both 50 Hz and 400 Hz than the sheared ones. This is not uncommon for laser cutting and it is believed to be a result of thermally induced stresses during the laser cutting process. It is difficult to say how normally stamped machine laminations would have compared with the laser cut ones for the prototypes. Stamping could produce somewhat higher losses than the squaring shears, which are normally in a very good condition, but perhaps not as much as the laser cut samples in this case. Furthermore, there is also an effect of the distance between the cut edges, which is smaller (implying larger effect on the loss level) for the laminations compared to the Epstein strips. A guesstimate is that good quality stamped machine laminations would give a few percent lower iron losses compared to the laser cut laminations used in the prototypes.

Table 2.14: Loss comparison between shear and laser cut.

		Cutting Method		
		Shears 1	**Laser**	**Shears 2**
Loss at 1.0T/50Hz	(W/kg)	0.96	1.20	0.95
Loss at 1.5T/50Hz	(W/kg)	2.22	2.60	2.24
Loss at 1.0T/400Hz	(W/kg)	17.20	9.27	17.32
Loss at 1.5T/400Hz	(W/kg)	42.44	43.97	42.60
J_{2500} at 50Hz	(T)	1.53	1.53	1.53
J_{10000} at 50Hz	(T)	1.75	1.75	1.75

The magnets used in the rotor are graded N35SH from Sura Magnets [44]. This magnetic material can operate at temperatures up to 150 °C, and it is characterized by a remanent flux (B_r) equal to $1.22\,T$, the coercivity (bH_c) is $900\,kA/m$, the intrinsic coercivity (iH_c) is $1590\,kA/m$, and the energy product (BH_{max}) is $280\,kJ/m^3$.

As mentioned in 2.4.6, the machine is wound with $0.8\,mm$ diameter copper wire, insulation class H, manufactured by Dahréntråd, Sweden. A double layer distributed winding is used in order to shorten the length of the end windings.

An 8-pole variable reluctance Singlsyn resolver (by Tamagawa, Japan) is installed in the machine. The maximum rated error for the resolver is ±30' mechanical angle (i.e. ±2 electrical degrees for an 8-pole machine). [45]
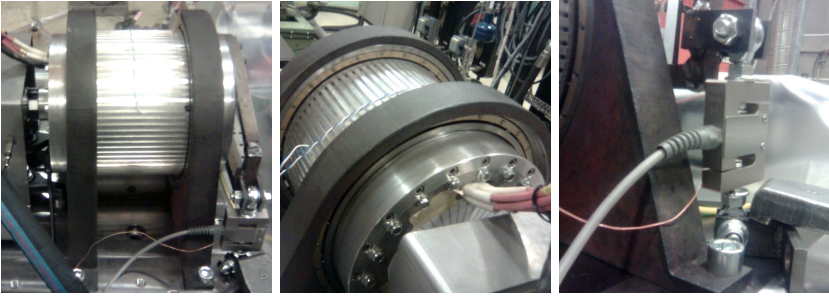
Figure 2.17: Torque measurement setup with a load cell.

Initially a torque measurement setup with a load cell is tried out. Figure 2.17 shows this setup, in which the electric machine is attached to the test bench with two large bearings, allowing movement in the circumferential direction. Although the system is simple both to operate and calibrate, it does not meet the expected accuracy despite the high accuracy of the load cell. The reason is that friction in the bearings increases substantially when the machine case temperature rises, due to the difference in the thermal expansion coefficients of aluminum and steel. In order to evaluate the torque deviation, a new setup is created, using two load cells as shown in Figure 2.18. The length of the input lever arm is $0.7030\,m$ and the length of the output lever arm is $0.2192\,m$.
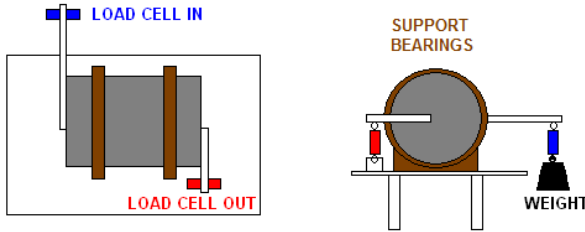

Figure 2.18: Torque friction measurement setup with two load cells.

Table 2.15 collects the friction torque measured with a cold machine. From the results, it can be seen that the error is between 0.6 and $2.1\,Nm$. The average of the error is $1.17\,Nm$, i.e. $1.2\,\%$ of the maximum torque specification of $100\,Nm$. Besides, there is no special relationship between the error and the input torque. With a cold machine, a good calibration of the load cell and accurate measurement of the lever arm, the torque offset (measured value when zero input torque is applied) is fairly stable, and the output torque value can be trusted if the $1-2\%$ friction torque is accounted for and compensated.

Table 2.15: Friction torque in the support bearings (cold machine).

Weight in (Kg)	Weight out (Kg)	Torque in (Nm)	Torque out (Nm)	Torque dif. (Nm)
2	6.095	13.8	13.1	0.7
5	15.465	34.5	33.3	1.2
7	21.885	48.3	47.1	1.2
10	31.785	69.0	68.3	0.6
12	38.025	82.8	81.8	1.0
15	47.455	103.4	102.0	1.4
17	53.565	117.2	115.2	2.1

If the same experiment is repeated with a warm machine the results differ significantly (outer case temperature around 80 ℃). Table 2.16 shows the results obtained in such case.

Table 2.16: Friction torque in the support bearings (warm machine).

Weight in (Kg)	Weight out (Kg)	Torque in (Nm)	Torque out (Nm)	Torque dif. (Nm)
2	1.55	13.8	3.3	10.5
5	9.65	34.5	20.8	15.7
7	15.70	48.3	33.8	14.5

From Table 2.16 it is clear that the load cell setup is completely unreliable when the machine temperature increases over the ambient temperature. As a consequence, a new torque measurement system is needed.

The torque is measured using a HBM T32FNA transducer rated for $500\,Nm$ together with the amplifier HBM MD18N. The expected accuracy from the torque transducer is $\pm 0.2\%$ at the nominal value and from the amplifier an error of $\pm 0.15\%$ could be expected [46]. In order to measure the DC power input to the power electronic module, as well as the AC power out to the machine, a power analyzer LEM Norma 5000 (now commercialized by Fluke) [47], equipped with four high performance current transducers LEM IT 150-S is used in the test bench [48].

The machine is tested against a speed controlled hydraulic break system. Figure 2.19 shows the experimental torque, flux linkage and efficiency maps obtained from the experimental measurements.
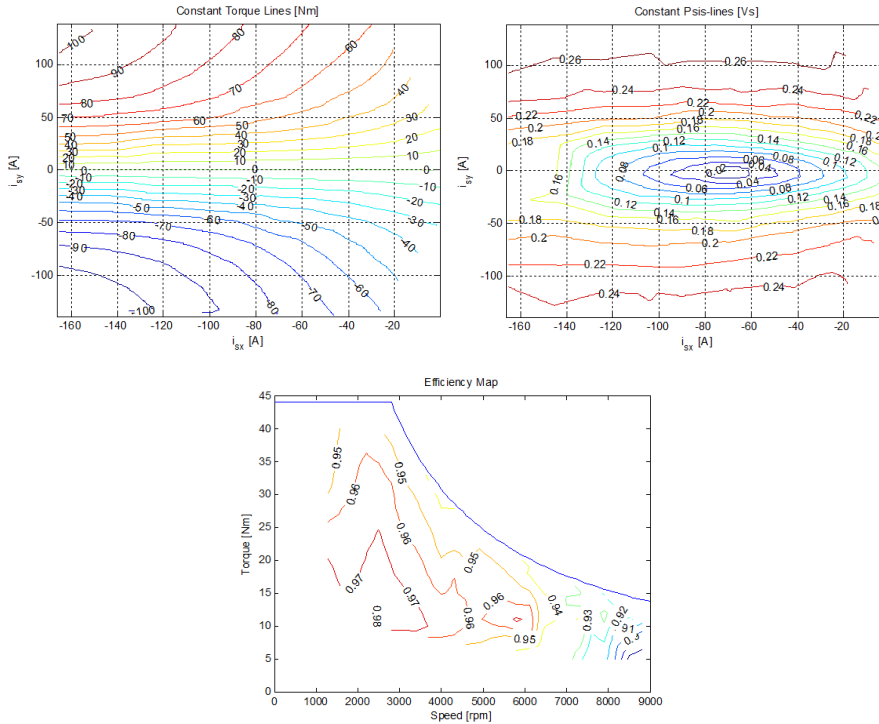

Figure 2.19: Experimental test results.

Comparing the FE simulation and the experimental results, a reasonable correspondence is observed between the simulated and the measured torque maps. However, the simulated flux map is not as accurate as expected. Looking at both Figures 2.16 and 2.19 it is clear that the simulated machine needs a higher field weakening current for a full demagnetization. One of the goals of the project is to validate the design tool against a real design. Therefore, it is interesting to explore the differences between the simulated and the experimental characteristics and try to find a motivation. A close comparison between the 2D FE simulation model and the manufactured machine reveals two possible aspects of the model that are susceptible of improvement in order to increase the accuracy of the results:

a. For mounting purposes, the hole in which the magnets are embedded is slightly bigger than the magnets themselves. That results in an airgap of 0.16 mm all around the magnet

b. The magnetic properties of the materials considered in the simulations do not exactly match those in the prototype

Concerning material properties, several differences can be found. The electric steel originally considered in the simulations was M235-35A ($0.35\,mm$ thick with maximum loss of $2.35\,W/kg$ at $1.5\,T$ and $50\,Hz$), which is replaced by M250-35A ($0.35\,mm$ thick with maximum loss of $2.50\,W/kg$ at $1.5\,T$ and $50\,Hz$) in the prototype due to the easier availability of the later. The B-H curve for these two electrical steel grades is just slightly different, and it is not likely to be the source of the observed differences. Nonetheless, the simulation model is updated to take into account the new steel grade.

Besides, a standard NdFeB magnet material is used in the design stage simulations before the magnet supplier was known. The model is updated with the magnetic characteristics of the actual magnet material in the machine (grade N35SH, Sura Magnets). Since temperature has a significant influence in the magnetic properties, a temperature of 80 ℃ is considered in the simulation model, based on the temperatures registered during the testing period.

Finally, an upgraded model considering all these modifications is simulated. The simulation results are shown in Figures 2.20 to 2.22, in which the experimental maps are superimposed for the sake of comparison [49].

From Figures 2.20 to 2.22 it is easily seen that the correspondence between the simulated and the experimental maps has improved significantly with the modifications introduced in the model. Nevertheless, small differences still exist between the numerical and the experimental results, which can be explained by the simplifications and assumptions made during the modeling process (i.e. 2D modeling, assumption of homogeneous and isotropic materials, modeling of the windings, etc.) and obey to a compromise between computation time and accuracy of the results. Comparing the measured efficiency map and the simulated one, the largest discrepancies are found at high speeds. Measuring efficiency is always difficult since the results are heavily dependent on the accuracy of the torque measurement. Several circumstances such as a slight misalignment of the torque transducer, mechanical vibrations of the set up or temperature drift of the electronic amplifier can cause disturbances on the measurement. As mentioned in section 2.4, the simulation model takes into account just copper losses in the windings and iron losses in the stator core of the machine. The iron losses in the rotor core and permanent magnets as well

as mechanical friction and windage losses are neglected at this stage, and they
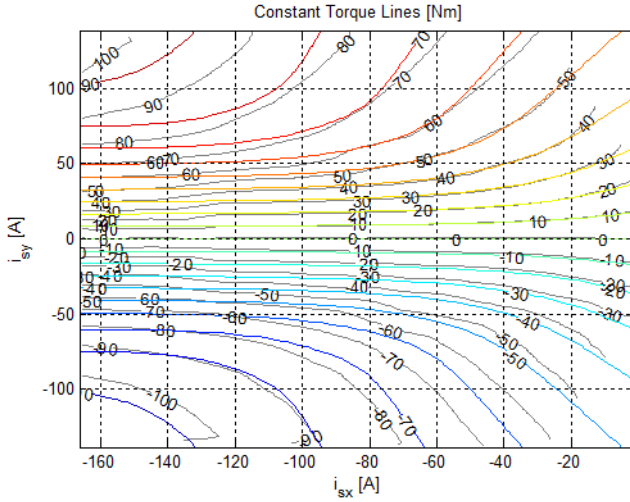are also more significant at higher speeds.
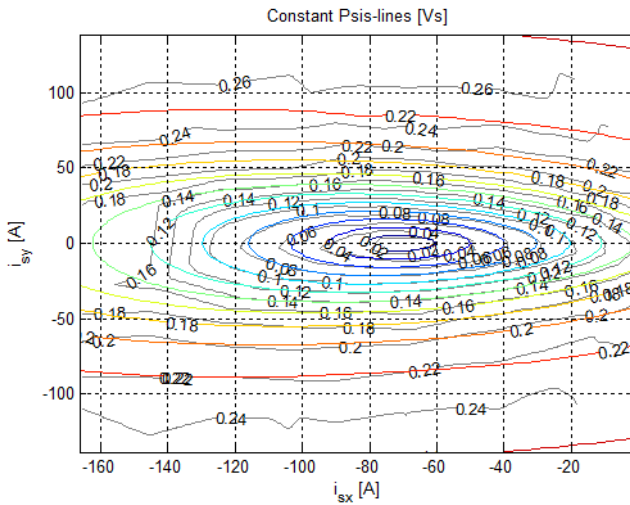

Figure 2.20: Experimental vs. simulated torque map

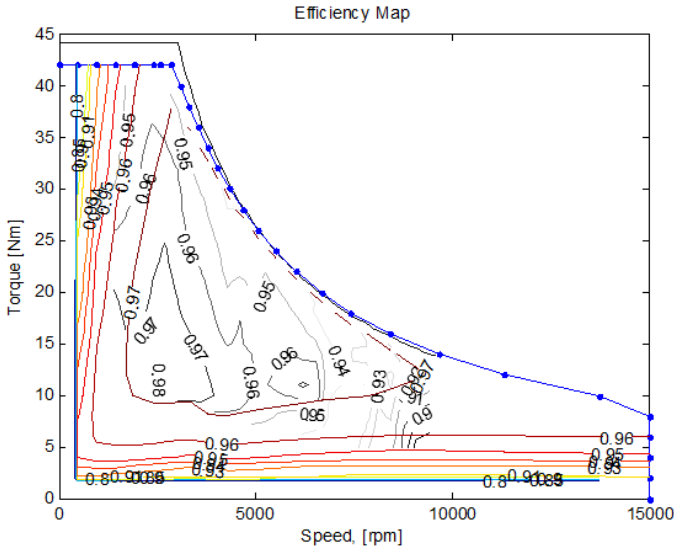**Figure 2.21:** Experimental vs. simulated flux linkage map

Figure 2.22: Experimental vs. simulated efficiency map

2.6   Dynamic Testing characterization

By a fortunate coincidence, a completely different method for characterizing electrical machines starts to be investigated within the research group just after the conclusion of the tests presented in the previous section. Timing is then perfect for a synergetic re-testing of the machine. Running the Dynamic Testing method on the E-RWD machine serves as a confirmation of the results obtained in the conventional test bench, and at the same time, proves the validity of this new approach by contrasting the result from both tests.

The Dynamic Testing method consists on accelerating the test machine back and forth, applying different current set-points. Assuming that the machine currents, voltages, and speed can be measured accurately (and with a sampling frequency high enough) and provided that the moment of inertia of the rotary part is known, the torque, flux linkage (and with some extra measurements, the efficiency maps) can be determined.

In a PMSM, if the currents remain constant for a certain interval of time, the torque over that time is also constant according to (2.3).

$$T = \Psi_m \, i_{sy} + (L_{sx} - L_{sy}) \, i_{sx} \, i_{sy} \tag{2.3}$$

Mechanically, the machine is not connected to any external load. Therefore, neglecting friction both with air and in the bearings and also the inherent losses in the machine, if a constant electromagnetic torque is applied the speed increases linearly, i.e. the time derivative of the speed is constant, and proportional to the applied torque, with the moment of inertia of the rotating mass as the proportion ratio (see (2.4)).

$$T = I_{ax} \frac{d\omega_{mech}}{dt} \tag{2.4}$$

Since the machine is not connected to anything, the effective moment of inertia I_{ax} is just the moment of inertia of the rotor and the shaft. Usually, for electrical machines in the range of 10 - 100 kW the value of I_{ax} is low, and therefore the speed will increase very rapidly for the torque levels under study. A fairly simple solution is to connect an extra flywheel to the shaft, increasing the moment of inertia of the rotating mass substantially. In this way, the rotor acceleration is reduced for a given torque, so it takes longer time to reach the maximum speed (limited by the DC voltage of the inverter). This implies also that for a given sampling frequency, there will be more samples available for the computation of the machine characteristics for that particular current set-point, which in general results in a higher accuracy.

However, it is worth noticing that the accuracy of the calculated torque relies on the accuracy of the speed measurements from the resolver and the estimation of the inertia of the rotating mass. It is then crucial to estimate the inertia of the rotating mass (rotor, shaft and added flywheel) as accurate as possible.

A drawing with the dimensions of the rotor, shaft and external flywheel as well as their corresponding moments of inertia are presented in Figure 2.23 and Table 2.17 respectively.

Table 2.17: Moment of inertia of the different rotating masses.

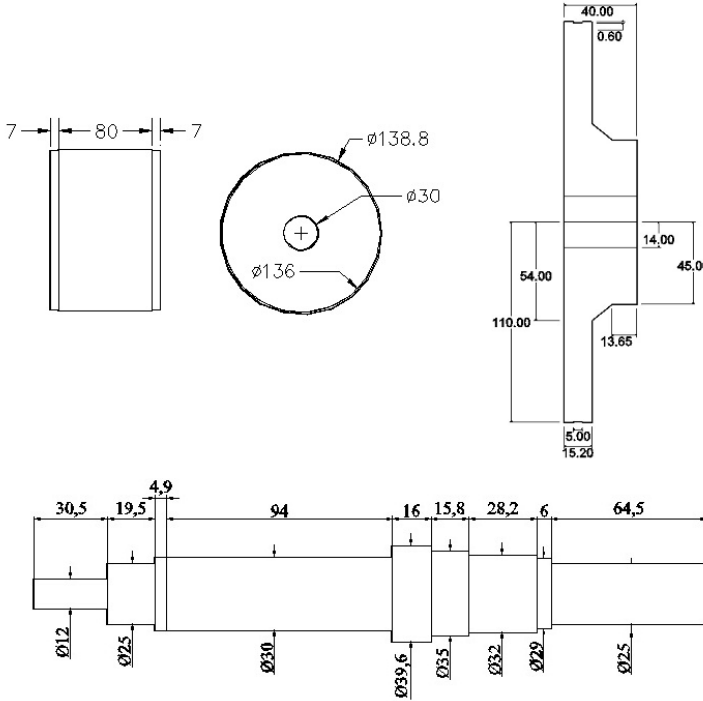| Moment of inertia	
Rotor block	0.02651600
Rotor shaft	0.00016217
External flywheel	0.02770000
Total inertia	0.05380400

Figure 2.23: Physical dimensions of the rotating masses for the inertia calculations.

The flux linkage characteristics are computed from the stator voltages in the rotor frame (U_{sx} and U_{sy} in (2.5)).Since the currents are kept constant over the acceleration time, and assuming constant stator resistance and inductances, the only time dependent component of the stator voltage is the induced back emf (the last term in (2.5)). Since the rotational speed ω is known, it is possible to calculate the stator flux linkage. [50]

$$U_{sx} = R_s\, i_{sx} + L_{sx}\, \frac{\partial i_{sx}}{\partial t} - \omega\, \Psi_{sy}$$

$$U_{sy} = R_s\, i_{sy} + L_{sy}\, \frac{\partial i_{sy}}{\partial t} + \omega\, \Psi_{sx} \tag{2.5}$$

In order to obtain the torque and flux linkage characteristics of the E-RWD machine, it is accelerated several times from 0 to 2500 rpm in order to keep a

certain voltage margin at all times. Each time a different current set-point is
applied. The values of the x-axis current (i_{sx}) vary from 0 to 70 A in steps of
5 A while the values of the y-axis current (i_{sy}) vary from 5 to 70 A in steps of
5 A. Note that only motor operation (and not generator) is studied.

Figure 2.24 shows the torque and flux linkage maps resulting from the
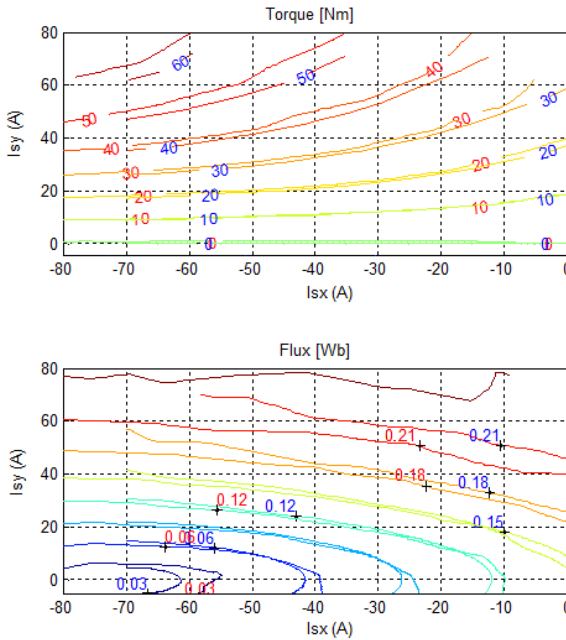Dynamic Testing together with those previously obtained.

Figure 2.24: Dynamic Testing (blue) vs. traditional test bench results (red).

When comparing the Dynamic Testing results with the ones obtained in
a traditional test bench they appear to be smoother. The reasons for this
can be a higher accuracy of the new method, since every current set-point
is calculated as the average of many samples, together with a much smaller
temperature deviation from one set-point to another, since the Dynamic Testing
sequence executes in just a few minutes, not enough to affect the rotor magnet
temperature significantly.

Nevertheless, the correspondence between the results from both tests is
reasonably high. The machine appears to be stronger in the Dynamic Testing

results (less current is needed for the same output torque) which could actually
be due to the lower magnet temperature during the tests. [51]

Calculating efficiency from the Dynamic Testing results available is some-
what more complicated, since all measurements are made just between 0 and
a limited speed just below base speed (2500 rpm in this case). While copper
losses are mostly dependent on the current loading and the winding resistance,
iron losses depend on the magnetic field frequency, and therefore in order
to include them in the measurements the speed limit needs to be increased.
This introduces added complexity to the whole test, since for high speeds the
PMSM must be operated in field weakening. For this reason, the efficiency map
obtained from the Dynamic Testing measurements is not presented, waiting
for further development of the method.

From the comparison of the results shown in Figure 2.24, it can be concluded
that the initial objectives of confirming the results previously obtained in the test
bench plus proving the validity of the Dynamic Testing method implementation
are both fulfilled.

2.7   Full unit and vehicle testing

Once confirmed that the performance of the standalone electrical machine
corresponds to what the simulations predict, it is time to assess the full E-RWD
unit. First the unit is evaluated at the Haldex - BorgWarner facilities in
Landskrona (Sweden). The unit is coupled to a test rig in which the left and
right axles can be loaded independently. There is a torque sensor in both shafts
in order to evaluate the torque vectoring capabilities of the unit. Figure 2.25
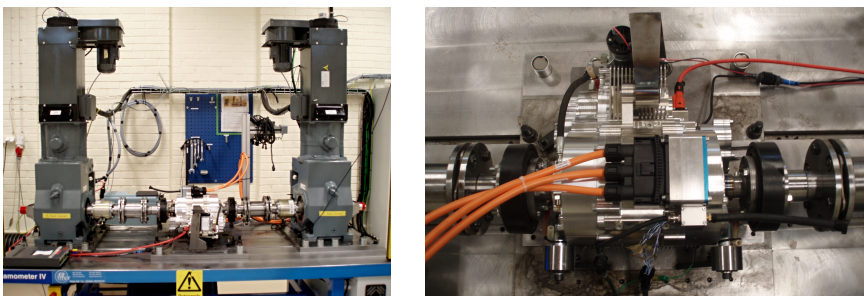shows the full unit in the test rig.

Figure 2.25: Full E-RWD unit test.

During these tests, the torque vectoring function is demonstrated and the capabilities of the system are assessed, both in terms of the maximum available torque per axle and the dynamic response of the E-RWD unit.

Figure 2.26: First test vehicle Saab 93.

Subsequently, the unit is installed on a Saab 93 which is slightly modified to accommodate the system (see Figure 2.26). The vehicle equipped with the E-RWD unit is first tuned up at Haldex - BorgWarner facilities in Landskrona (Sweden). The E-RWD unit controller needs to be integrated with the main control system in the vehicle and the parameters of the current controllers for the traction and torque vectoring motor are also adjusted at this time. After this initial preparation, the vehicle is shipped to the winter test facilities in Arjeplog, in northern Sweden, where professional test drivers and experts from several car manufacturers have the opportunity to try out the concept, and give valuable feedback that motivates the redesign proposed in Chapter 3 and the development of a new prototype.

2.8   PMSM Thermal modeling

The thermal model plays an essential role in the process of designing an electrical machine since the power rating of a machine, both for continuous and intermittent operation, is most commonly limited by its thermal capabilities. Besides, some components of the machine such as winding insulation and permanent magnet materials are very sensitive to temperature, and can be irreversibly damaged when operated over the rated temperature. Consequently, it is advisable to be able to either measure or estimate the sensitive temperatures when operating the machine.

2.8.1   Model development

Due to time constrains during the design stage, only the stationary FE analysis already included in the design software is considered for the thermal dimensioning of the electrical machine. This analysis assumes that all the heat generated inside the machine is dissipated through the outer surface of the machine case by convection cooling, assuming a convection coefficient at the outer case surface of $h_{ca} = 15\,W/(m^2 K)$. However, due to the 2D nature of the FE model used, only the outer convective area corresponding to the machine's active length is taken into account, and therefore the resulting current loading is underestimated (around $3.8\,A/mm^2$ for most of the machines simulated) according to previous design experiences. As stated in section 2.4.4, a current loading of $6.5\,A/mm^2$ is regarded as suitable for this machine size during the design process. The thermal model presented in this section is used, together with the experimental measurements registered, to verify this assumption and to evaluate the overloading capabilities of the machine.

The developed model is a lumped-parameter model, in which those parts of the machine which are likely to have similar temperatures are grouped together in a single node, and nodes are interconnected through thermal resistances representing the heat conduction, convection, and/or radiation between the different parts of the machine geometry. Thermal capacitances are coupled to each node in order to include the transient behavior of the corresponding components.

In the lumped-parameter model, the different thermal elements are computed based on the analytical equations governing the different heat transfer mechanisms. However, these equations can be difficult to solve for complex geometries, and some simplified conditions must be assumed for the calculations [52]. Additionally, the heat transfer at some particular places in the machine becomes difficult to compute analytically, either due to the difficult characterization of the geometry involved or to the presence of several heat transfer mechanisms at the same time. Examples of this are the interface between the stator lamination stack and the outer case, the convection and radiation heat transfer at the end windings, the convection at the rotor ends or the radiation heat transfer inside the machine. In this cases, the computation of the corresponding thermal elements in the model relies upon experience from previous designs and experiments in form of empirical correlations. To be able to compute the thermal elements, some simplifications of the machine geometry are assumed. The initial geometry is presented in Figure 2.27a together with the simplified one in Figure 2.27b. The final model, consisting on 9 nodes in total, is shown in Figure 2.28.
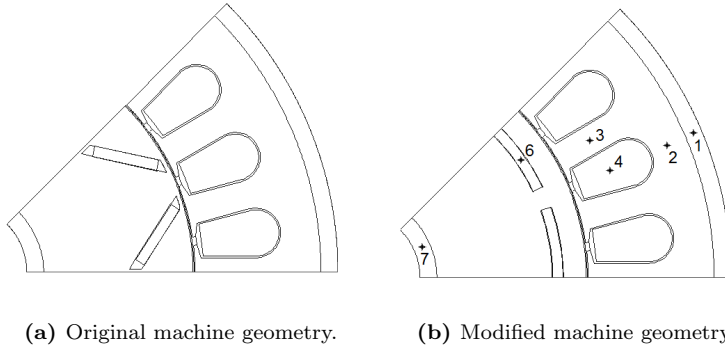
(a) Original machine geometry.   **(b)** Modified machine geometry.

Figure 2.27: Original and modified rotor geometry for the thermal model.

As seen in Figure 2.27b, the nodes (marked with a star) are located in the midpoints of the outer aluminum case, the stator yoke, the stator teeth, the stator winding, the rotor magnets and the rotor shaft in the cross section of the machine. Additionally, there are nodes placed in the end windings and in the bearings, and an extra node representing the ambient air temperature.
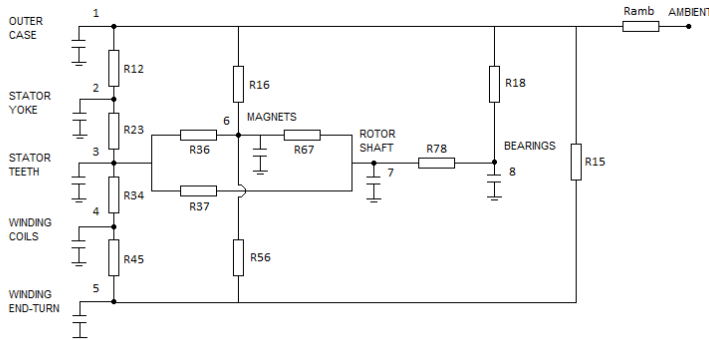
Figure 2.28: Thermal network for the electric traction machine.

The model developed within the project is mostly based on the work by J. Lindström [53] and G. Kylander [54], although some of the thermal elements are also evaluated using alternative approaches in order to quantify the sensitivity of the final results to some of the most uncertain parameters. The thermal resistances corresponding to the outer case, the stator yoke, the upper and lower section of the rotor yoke, the permanent magnet insulation, the permanent

magnets and the rotor shaft can be modeled as radial conduction in a section
of a cylinder according to (2.6), where r_o and r_i are the outer and inner radius
of the geometry part, L is the length in the axial direction and λ is the thermal
conductivity of the material.

$$R_{th} = \frac{ln(r_o) - ln(r_i)}{2\pi L \lambda} \tag{2.6}$$

The thermal behavior inside the stator slots is not easy to model due
to the random disposition of the winding wires inside the slot, combining
copper wires, insulation coating and air as shown in Figure 2.29. Extensive
research is available on how to model the heat transfer inside the slots and
its thermal interaction with the rest of the machine. Different solutions are
presented, increasing in complexity as more detailed results are required [55–58].
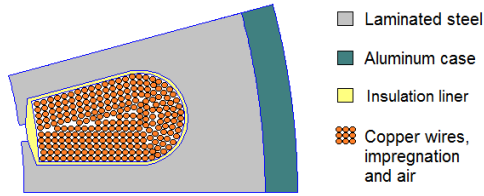

Figure 2.29: Winding configuration inside a stator slot.

In this work the temperature distribution inside the slot is not as important
as the overall temperature distribution in the machine, hence a fairly simple
approach with just one node is adopted. The thermal elements are calculated
assuming a rectangular slot with the same cross sectional area as the original
one according to the model proposed in [53, 54]. The original and the resultant
slot are shown in Figure 2.30. The equivalent slot volume is filled with a
homogeneous material, with no air pockets inside and uniform heat generation.
The conductivity of this material (λ_Q) can be calculated as a function of
the geometry, the slot fill factor and the thermal conductivity of the winding
impregnation as stated in [54]. The following equations describe the calculation
of the equivalent slot dimensions.

$$d = d_I + d_A \tag{2.7}$$

$$b = \frac{x_{Q3} + x_{Q2}}{2} - 2\,d \tag{2.8}$$

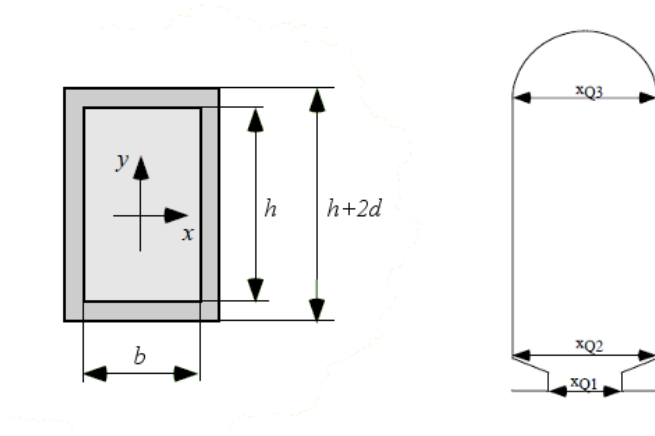$$h = \frac{2\,A_Q}{x_{Q3} + x_{Q2}} - 2\,d \tag{2.9}$$

Figure 2.30: Equivalent rectangular slot for the thermal model [53].

A_Q is the slot cross sectional area, x_{Q2} and x_{Q3} are the slot widths as shown in Figure 2.30 and d is an equivalent insulation thickness consisting on the slot insulation thickness d_I and the equivalent air film thickness d_A. A value of $d_A = 0.3\,mm$ is suggested in [54] for a 15 kW machine.

The thermal resistance between the winding coils and the stator teeth is calculated as (2.10), assuming that the temperature in the boundary of the equivalent rectangular slot is uniform and equal to the average stator teeth temperature.

$$R_{th} = \frac{R_x R_y}{Q_s\,l_u\,(R_x + R_y)}\left(1 - \frac{R_{x0}\,R_{y0}}{720\,(R_{x0} + R_{y0})}\right) \tag{2.10}$$

The per unit-length resistances are defined by

$$R_x = \frac{1}{2}\left(R_{ix} + \frac{R_{x0}}{6}\right) \tag{2.11}$$

$$R_y = \frac{1}{2}\left(R_{iy} + \frac{R_{y0}}{6}\right) \tag{2.12}$$

The slot material contributes with

$$R_{x0} = \frac{h}{b\,\lambda_Q} \tag{2.13}$$

$$R_{y0} = \frac{b}{h\,\lambda_Q} \tag{2.14}$$

and the slot insulation and air pockets contribute with

$$R_{ix} = \frac{d_I}{h\,\lambda_I} + \frac{d_A}{h\,\lambda_A} \tag{2.15}$$

$$R_{iy} = \frac{d_I}{b\,\lambda_I} + \frac{d_A}{b\,\lambda_A} \tag{2.16}$$

The thermal resistance of the stator teeth is calculated from integration along a tooth in the radial direction, assuming that the resistances of all the individual teeth are in parallel. Considering a tooth geometry like the one in Figure 2.31, the teeth thermal resistance is computed by (2.17).
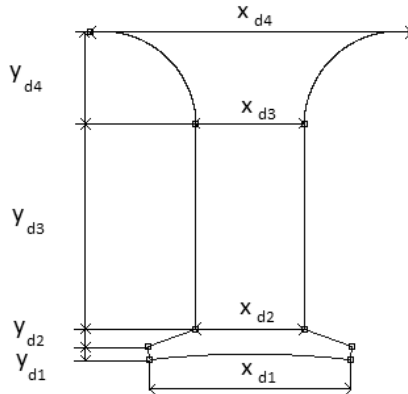

Figure 2.31: Geometry of a stator tooth.

$$R_{th} = \left[\frac{y_{d_1}}{x_{d_1}} + \frac{y_{d_2}}{x_{d_1} - x_{d_2}} \left(ln \left| \frac{x_{d_1} \, y_{d_2}}{x_{d_1} - x_{d_2}} \right| - ln \left| y_{d_2} - \frac{x_{d_1} \, y_{d_2}}{x_{d_1} - x_{d_2}} \right| \right) \right.$$

$$\left. + \frac{y_{d_3}}{x_{d_3}} - \frac{\pi}{4} + \frac{a}{\sqrt{a^2 - 1}} \; \arctan \left(\frac{a + 1}{\sqrt{a^2 - 1}} \right) \right] \frac{1}{\lambda_{Fe} Q_S l_u} \qquad (2.17)$$

with

$$a = \frac{x_{d_3} + 2 \, y_{d_4}}{2 \, y_{d_4}} \qquad (2.18)$$

From the thermal management point of view, the end windings are one of the most important parts of the machine. When the machine is loaded with a certain current, copper losses (also called resistive or Joule losses) are generated within the conductors. The coil sides, inside the slot, have been analyzed already, and from their study it is concluded that the heat generated in the coil sides flows out by conduction through the slot insulation to the stator teeth and core, to be finally dissipated through the outer case. However, for most designs, the end windings are hanging outside the stator lamination pack, which eliminates the possibility of radial conduction. Hence, the heat generated in the end windings is partly transferred into the slots by conduction -and then follows the radial path out of the machine- and the rest is dissipated by convection to the internal air enclosed inside the machine and radiation to other machine parts.

The thermal resistance corresponding to the heat conduction between the end windings and the coil sides can be calculated as

$$R_{th} = \frac{l_{av}}{3 \, A_{Cu} \, \lambda_{Cu}} \qquad (2.19)$$

where l_{av} represents the average length of half a turn, and can be calculated as (2.20), A_{Cu} and λ_{Cu} are the copper cross sectional area in the slot and the thermal conductivity of copper respectively. L_{Fe} is the active length of the machine, r_{top} and r_{bot} are the radial distance to the top and bottom of the slot and σ is an experimental constant equal to 1.6.

$$l_{av} = L_{Fe} + \sigma \, \pi \left(\frac{r_{top} + r_{bot}}{N_p} \right) \qquad (2.20)$$

From a thermal point of view, all coils are parallel connected, and therefore the total thermal resistance between the end windings and the coil sides is obtained dividing the expression in (2.19) by two times the number of slots N_q.

Modeling convective heat transfer at the end windings is usually a difficult task. Due to the complex nature of the conductor and insulation lining arrangement in this area, noteworthy differences appear between different machines, and hence developing a general model is hardly possible. In this study, the convective flow is modeled assuming that the end windings are enclosed in a cylinder, and the convection coefficient is obtained from an empirical correlation. Two correlations have been considered, (2.21) cited in [54] and (2.22) cited in [59].

$$h_{et} = 6.5 + 5.25\, u_r^{0.6} \tag{2.21}$$

$$h_{et} = 41.4 + 6.22\, u_r \tag{2.22}$$

where u_r denotes the rotor peripheral speed in m/s. The validation of the thermal model with the experimental measurements will determine which of these correlations applies better for the test machine.

Since all the empty space inside the machine enclosure is actually filled with air, convective heat transfer takes place at several other regions inside the machine. Besides the end windings, the internal air exchanges heat with the inner side of the machine case and the rotor end rings. In some of the reviewed literature the air inside the machine is assigned a node in the lumped-parameter circuit model. Nevertheless, the temperature of the internal air itself is not relevant, and the model proposed in [53] uses star-to-delta transformation in order to reduce the order of the model eliminating the internal air node, thus interconnecting the outer case, the rotor side surfaces and the end windings. As for the end windings case, it is hard to find a general model that characterizes the convective heat flow inside the machine. The following empirical correlations are used in the thermal model developed, according to [53] and [54].

$$h_{ica} = 15 + 6.75\, u_r^{0.65} \tag{2.23}$$

$$h_{rr} = 16.5\, u_r^{0.65} \tag{2.24}$$

where h_{ica} represents the convection coefficient at the inner surface of the outer case, and h_{rr} at the rotor end rings.

Heat transfer through the airgap plays a very important role in the thermal management of the machine. During operation, a fraction of the total losses is generated in the rotor mostly in form of iron losses (eddy current losses and hysteresis losses) both in the rotor laminations and in the permanent magnet material, but also windage losses as the rotor spins. In those machines in which there is no alternative cooling of the rotor, most of the heat generated in the rotor either flows through the airgap to the stator or is dissipated by convection at the rotor end rings.

The heat transfer in the airgap is described by the Taylor-Couette theory by means of the Taylor number or modified Taylor number [54, 60, 61]. For pure laminar flows (low Taylor numbers), the air velocity lacks a radial component and therefore most of the heat transfer in the airgap consists of conduction and radiation between the rotor and the stator. However, over a certain rotor speed, the air flow becomes unstable, leading to the formation of Taylor vortex first and turbulent flow subsequently, promoting convection as the main heat transfer mechanism. The airgap length, the roughness of the rotor and stator surfaces, as well as the peripheral speed of the rotor have a large impact on the heat convection in the airgap. The modified Taylor number can be expressed as

$$Ta_{rr} = \frac{\omega_r^2 \, r_\delta \, \delta^3}{\nu_A^2} \tag{2.25}$$

where ω_r is the mechanical angular speed of the rotor, r_δ is the airgap radius, δ is the airgap length and ν_A is the kinematic viscosity of air. If the modified Taylor number is smaller than 1740, the air flow between the stator and the rotor is regarded as laminar and the Nusselt number is equal to 2. For higher Taylor numbers, the flow becomes turbulent and the Nusselt number can be calculated based on the (modified) Taylor number as

$$Nu = 0.409 \, Ta^{0.241} - 137 \, Ta^{-0.75} \tag{2.26}$$

The calculation of the convection coefficient based on the Nusselt number, the airgap dimensions and the heat conductivity of the air (λ_A), is straight forward.

$$h = \frac{Nu \, \lambda_A}{2 \, \delta} \tag{2.27}$$

Once that all the convection coefficients have been estimated, the associated thermal resistance can be calculated according to

$$R_{th} = \frac{1}{A \, h} \tag{2.28}$$

where A is the area where the heat exchange takes place.

The rotor is also thermally connected to the outer case through the rotor shaft and the bearings. Conduction in the rotor shaft is fairly simple to model, however, the thermal behavior of the bearings is much more complicated and empirical correlations provided by the bearing manufacturer SKF are proposed in [53]. Equations (2.29) and (2.30) are used for conduction in the shaft and in the bearings respectively.

$$R_{th} = \frac{L_{bb}}{\pi \, r_{sh}^2 \, \lambda_{sh}} \tag{2.29}$$

$$R_{th} = 0.45 \, (0.12 - d_b)(33 - \omega_r \, d_b) \tag{2.30}$$

L_{bb} is the axial distance between bearings, r_{sh} and λ_{sh} are the shaft radius and conductivity respectively, d_b is the average diameter of the bearing and ω_r is the mechanical angular speed of the rotor.

Particularly difficult is the evaluation of the thermal resistance of the contact surface between the stator lamination stack and the outer case of the machine. [54] states that for machines in which the frame is directly cast on the core this resistance is negligible. However, for shrink-fitted frames, the temperature drop between the stator lamination and frame can be significant. The same reasoning applies for the contact surface between the rotor lamination stack and the shaft. The most accepted approach is to define an average equivalent gap between the two surfaces [53, 56, 57, 59]. In this study, an equivalent air gap of 0.01 mm is considered for both cases. The corresponding thermal resistance is easily computed using (2.6) and the heat conductivity of air.

If heat conduction to the test bench through the outer case fasteners is neglected, the heat generated inside the machine is dissipated to the ambient by convection and radiation at the outer case. There are empirical correlations available to calculate the heat dissipation for simple geometries [62] that can be used as first estimates; nevertheless for more complex geometries of the outer case it is advisable to refer to experimental results in order to improve the accuracy [56, 57, 63]. Following the guidelines in [63], the average convection coefficient h_{ca} for the whole outer case surface is estimated in $9\,W/(m^2 K)$, which takes also into account the effect of radiation.

The calculated values for each of the thermal elements in the model are presented in Table 2.18.

Table 2.18: Calculated thermal elements.

Element	K/W	Element	J/K
R12	0.00947	C1	11803
R15	0.45138	C2	1885
R16	0.36689	C3	1802
R18	0.09552	C4	969
R23	0.02182	C5	1261
R34	0.05173	C6	227
R36	0.49414	C7	4075
R37	3.54210	C8	180
R45	0.02213		
R56	4.61860		
R67	0.14570		
R78	1.34380		
Ramb	0.24386		

2.8.2   Experimental validation

In order to validate the thermal model presented in the previous section, several thermal runs are carried out in the test bench. The test machine is equipped with 22 PT100 temperature sensors distributed within the coil sides (3 units per phase), the end windings (3 units on each side, spanned 120 degrees), the outer case (3 units) and the bearings (2 units on each side).

Two thermal situations are presented in this study to verify the accuracy of the thermal model. For each of them the predicted and the measured temperature of the outer case, the winding coil sides and the end windings is compared, and the model is adjusted according to the obtained results.

Natural cooling at standstill

In this experiment, the starting temperature of the machine winding is around 80 ℃, and it cools down for over 90 minutes at 22 ℃ ambient temperature. This experiment is particularly useful to verify the accuracy of the calculated value for the convection/radiation coefficient between the outer case and the ambient. The green curves marked with a circle represent the simulated temperatures while the black ones with a triangle represent the experimental measurements.
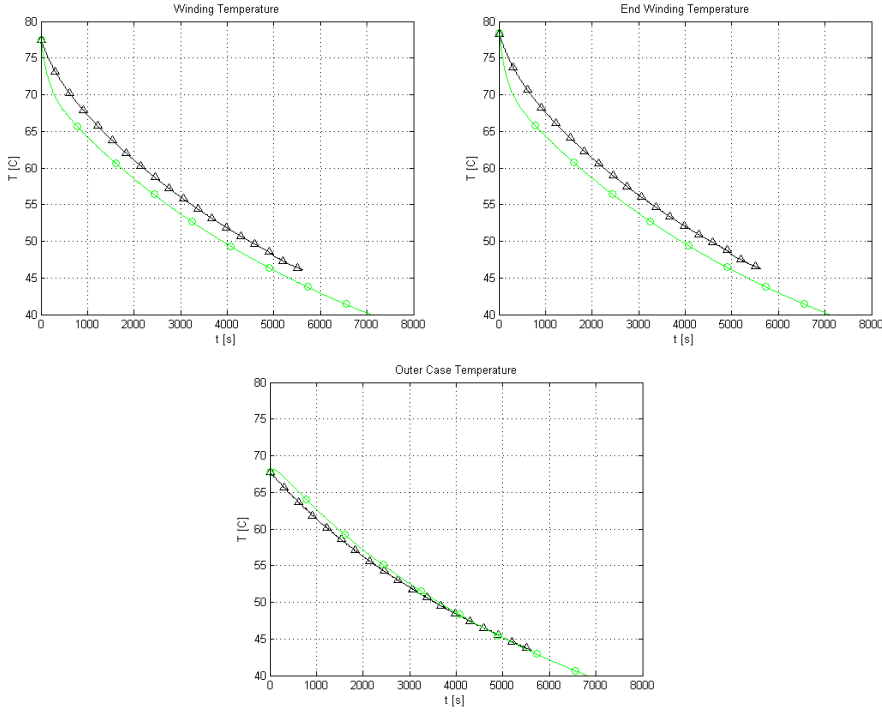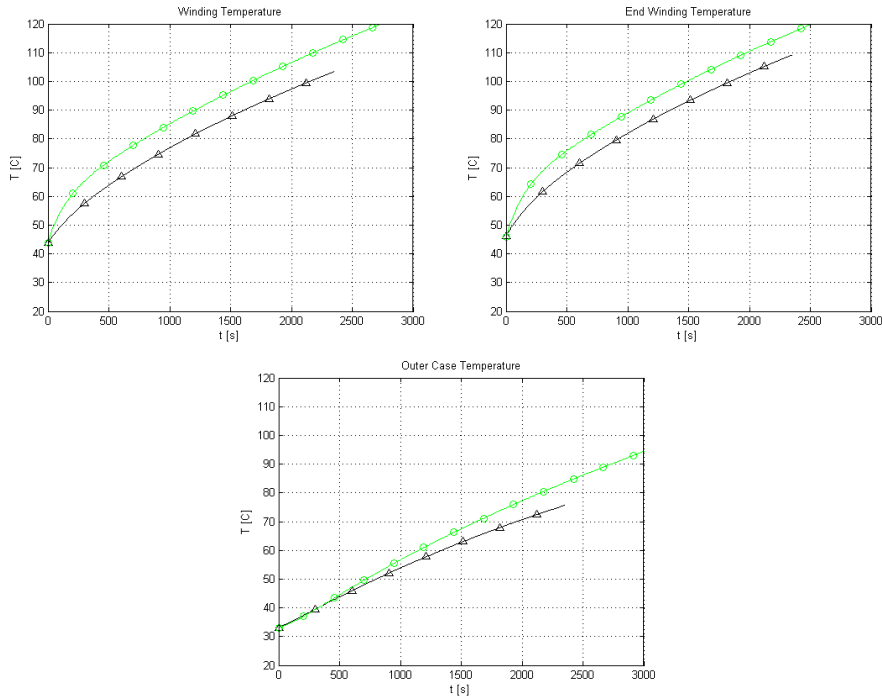
Figure 2.32: Experimental vs. simulated temperatures. Cooling case.

The maximum deviation, both in ℃ and percent of the maximum temperature Θ_{max} (assumed 150 ℃) is 2.2 ℃ (1.5% of Θ_{max}) for the windings, 2.4 ℃ (1.6% of Θ_{max}) for the end windings and 0.5 ℃ (0.3% of Θ_{max}) for the outer case. Based on the comparison between the simulated and the experimental temperatures, the value of the convection/radiation coefficient in the outer case h_{ca} is updated from $9\,W/(m^2K)$ to $7\,W/(m^2K)$, which leads to a change in $Ramb$ from $0.2439\,K/W$ to $0.3121\,K/W$. The plots in Figure 2.32 are for the updated value.

Nominal operation

In the second experiment, the machine is operated close to its nominal operation point until the hot-spot temperature reaches 120 ℃ . The machine spins at 2780 rpm (electrical frequency $f_{el} = 185.3\,Hz$), loaded with $44\,Nm$ @ $47\,A$. The green curves marked with a circle represent the simulated temperatures

while the black ones with a triangle represent the experimental measurements.

Figure 2.33: Experimental vs. simulated temperatures. Nominal operation.

In this case, using the updated value of the outer convection coefficient ($7.03\,W/(m^2 K)$), the maximum deviation, both in ℃ and percent of the maximum temperature Θ_{max} (assumed 150 ℃) is 9.8 ℃ (6.5% of Θ_{max}) for the windings, 7.9 ℃ (5.3% of Θ_{max}) for the end windings and 7.9 ℃ (5.3% of Θ_{max}) for the outer case. It is worth noticing the increased error in the outer case, which only depends on the outer convection coefficient if the estimation of the amount of losses generated is correct. The following figures show the estimated temperature error for three different values of the convection/radiation coefficient in the simulation model, the value obtained from the previous experiment $7.03\,W/(m^2 K)$, a higher value of $15\,W/(m^2 K)$ and an intermediate value of $12\,W/(m^2 K)$.

When looking at the rightmost plots (outer case temperature error) it can be seen that for $h_{ca} = 7.03\,W/(m^2 K)$ the simulated temperature error is diverging from 0 as the time increases. The simulated temperature becomes

larger than the experimental one and the difference increases with time. On the contrary, for $h_{ca} = 15\,W/(m^2K)$ the temperature error is also continuously diverging from 0, although this time the simulated temperature becomes lower than the experimental one. An intermediate value of $h_{ca} = 12\,W/(m^2K)$ yields to a steady temperature error around 0. Figure 2.37 shows the comparison between the simulated and the experimental temperature evolution for the updated value of $h_{ca} = 12\,W/(m^2K)$.
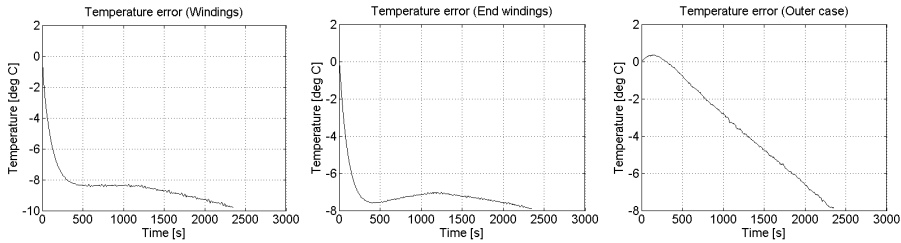
Figure 2.34: Simulated temperature error. $h_{ca} = 7.03\,W/(m^2K)$.

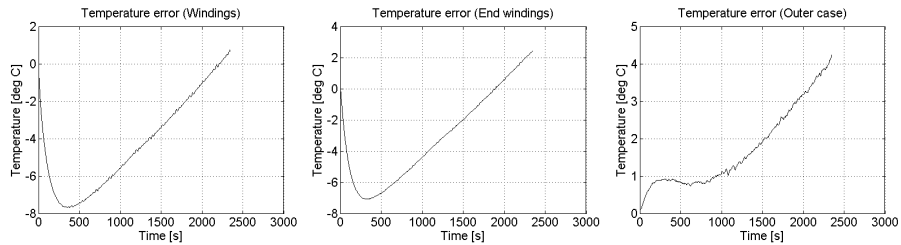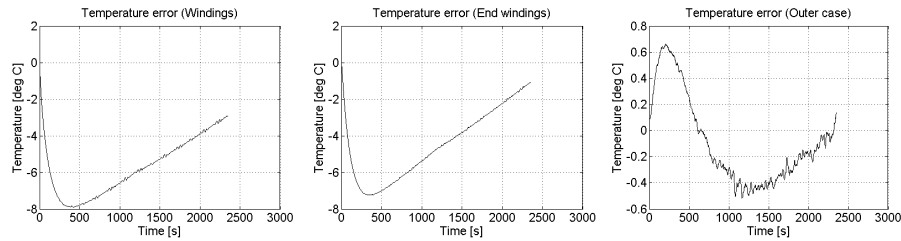**Figure 2.35:** Simulated temperature error. $h_{ca} = 15\,W/(m^2K)$.

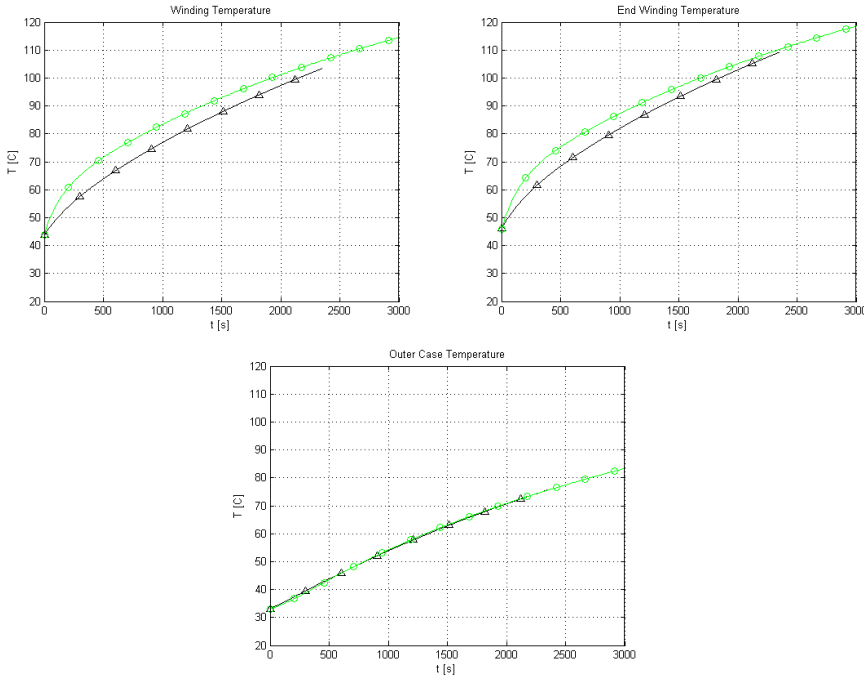**Figure 2.36:** Simulated temperature error. $h_{ca} = 12\,W/(m^2K)$.

Figure 2.37: Experimental vs. simulated temperatures. Nominal operation
and $h_{ca} = 12\,W/(m^2K)$.

The difference between the values of the convection/radiation coefficient in
both experiments ($7\,W/(m^2K)$ for the natural cooling at standstill and around
$12\,W/(m^2K)$ for the nominal operation) stresses the difficulty of obtaining a
good estimation of this parameter. Besides, finding a clear motivation to this
difference is not an easy task [64]. It is the author's opinion that several reasons
can contribute to the drift in the coefficient value:

- all thermal elements in the model are assumed to be constant, but in fact
  there is a temperature dependence to be taken into account. As the heat
  exchange surface becomes warmer, air properties change accordingly and
  air velocity increases, favoring natural convection.

- the amount of losses considered in the model is computed from the
  efficiency measured during the experiments. However this measurements
  may not be accurate enough, and the losses were overestimated in the
  nominal operation case (losses are zero in the first experiment), requiring
  for a higher convection coefficient in order to match the experimentally

measured outer case temperature.

- during the experiments the machine is mounted in two large ball bearings, and then fixed to a massive iron bench (see Figure 2.17). This provides an additional conduction path for the heat, which is not taken into account in the simulation model

2.9 Synchronous Reluctance Machine study

The Synchronous Reluctance Machine (SynRM) appears as an interesting machine topology for many reasons. The rotor construction is simple and rugged, consisting just in a stack of steel laminations with the right layout of flux barriers. The absence of magnets makes the machine less expensive than the PMSM alternative, and also reduces the cooling requirements since there is no risk of degradation of the permanent magnet material. Besides, there are no windings in the rotor, avoiding the use of slip rings and hence the need for maintenance. The stator of a SynRM is identical to that of a PMSM or an induction machine.

In order to evaluate the potential of the SynRM for the E-RWD unit, a parametrized geometry model of the rotor is created. The rotor geometry together with the description of the main geometric parameters are shown in Figure 2.38.
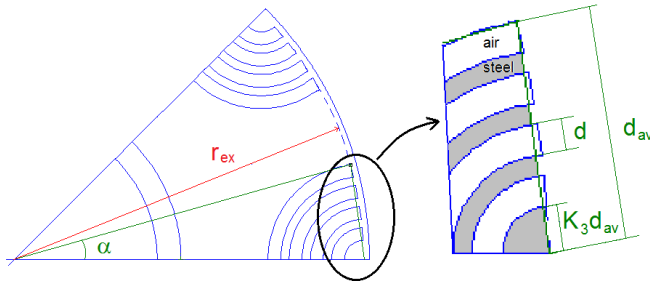

Figure 2.38: Synchronous Reluctance rotor geometry.

The main geometric parameters characterizing the SynRM rotor are:

- K_1 defined as the proportion of the rotor angular width occupied by the flux barriers to the pole pitch angle. The angle α in Figure 2.38 can be expressed as:

$$\alpha = K_1 \frac{\pi}{N_p} \tag{2.31}$$

- d_1 defined as the distance in millimeters from the outermost face of the flux barriers and the rotor outer radius. The radius r_{ex} and the length d_{av} in Figure 2.38 are then:

$$r_{ex} = r_{ro} - d_1 \tag{2.32}$$

$$d_{av} = 2\ r_{ex} \sin(\alpha/2) \tag{2.33}$$

- K_3 defined as the ratio between the radius of the inner side of the smallest flux barrier and the length d_{av}.

- K_2 defined as the proportion between the thickness of the flux barriers and the steel stripes in between them. If d represents the thickness of the flux barriers as shown in Figure 2.38 then the thickness of the steel stripe between two consecutive flux barriers is d/K_2.

When simulated, all the SynRM geometries exhibit a similar behavior independently of the combination of parameters considered: over the base speed the torque decays faster than $1/\omega$, and therefore the output power decays as well. This effect is clearly seen in Figure 2.39, representing the input power (blue), output power (black), stator winding copper losses (green) and stator iron losses (red) vs. speed for one of the geometries simulated.
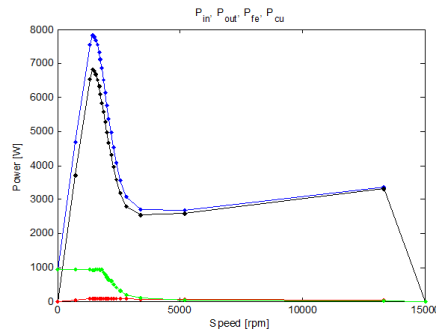

Figure 2.39: Synchronous Reluctance machine power characteristics.

Several attempts are made in order to increase the output power of the SynRM. The most successful one is to extend the flux barriers all the way to the

border of the rotor, i.e. set $d_1 = 0$ mm. In this way the output torque increases and the torque reduction over the base speed smoothes out. The output power in the constant region increases about 50%. However, this construction is physically unfeasible unless the rotor is bandaged and the flux barriers are filled with a non-magnetic material.

After discarding the bandaged alternative for its added complexity, the SynRM is analyzed mechanically to confirm that it withstands the centrifugal forces at maximum speed. A finite element model of the rotor geometry is simulated, and as a consequence, some changes are introduced in the arrangement of the flux barriers in order to increase the rotor's mechanical strength. A sketch of the final rotor geometry is presented in Figure 2.40.
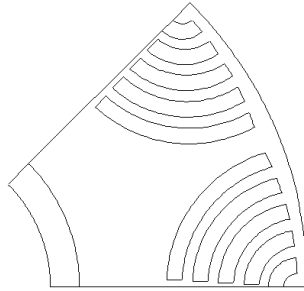

Figure 2.40: Modified Synchronous Reluctance rotor geometry.

The semicircular flux barriers are divided in two, with a steel bridge in the middle to hold them in place at high speeds. Besides, the distance to the rotor outer border (designated by d_1 in Figure 2.38) is no longer constant, and it increases as the flux barriers move inwards.

Although this geometry is not comparable to the PMSM alternative presented in the previous sections in terms of specific torque and power, a SynRM rotor is manufactured in order to broaden the scope of the project and increase the competence in this type of machines. The experimental results obtained from the SynRM tests are not part of this thesis.

2.10   Summary of the design and prototyping process

This section compiles a number of thoughts and conclusions over the work presented in this chapter.

Regarding the design process described, one clear (and also predictable) conclusion is the importance of a well-defined comprehensive set of specifications for a successful outcome. However, gathering such specification set has proven to be a difficult task, particularly for electric traction applications, since there is little expertise available when compared for example to electrical machines for industrial applications.

In the design of a new electric traction machine there is an important trade off to be made between the continuous power rating and the peak power capability of the machine. A good example of this is the configuration of the stator geometry, where a large slot cross sectional area leads to better thermal performance but less margin for magnetic saturation, favoring continuous power rating over peak power capability. Other significant compromises the designer needs to make are between peak torque and speed range, mostly reflected in the rotor design and magnets' size and layout; and between cost and efficiency, mostly affecting material qualities and manufacturing techniques.

A detailed FE model of a PMSM is somewhat complex, involving tenths of parameters between geometric, electromagnetic and mechanical parameters. A design software with pre-parameterized machine geometries like the one described in Appendix B appears as a very helpful tool when optimizing an electrical machine. With it, the most tedious design work is automated and the designer is left with the creative and intellectual tasks: analyzing the influence of the different parameters in the machine characteristics and decide the best way to proceed in order to reach the design goal.

A prototype of the traction machine is manufactured in order to test it and validate the design software tool. Based on the experimental test results, the original FE model is upgraded in order to account for aspects such as the magnet temperature that were initially disregarded. The correspondence between the FE predicted machine characteristics and the measured ones is thus improved.

A good learning from the testing experience is that measuring torque accurately is not an easy task. The load cell set up initially planned did not

work as expected, and a rotary torque transducer is installed. The accuracy of such transducer is greatly affected by its alignment with the shaft of the machine. Hence, significant work should be put into the installation of the transducer, to achieve as good an alignment as possible.

Measuring energy efficiency is not straightforward either, since the accuracy of the measurements rely directly on the accuracy of the torque and speed measurements. The output power of the machine is obtained as the product of output torque and speed, while in order to compute the input power to the machine the phase voltages and currents should be measured. Due to the switching nature of the voltages applied by the inverter, a suitable instrument is needed. Probably, the most direct and accurate approach is to use a power analyzer, which measures the voltages and currents and calculates the power on-line. If such equipment is not available, the current measurements from the inverter together with the voltage references resulting from the current controller in order to estimate the power fed to the machine. The voltage reference values can be compensated for the dead-band time and the voltage drops in the inverter in order to improve the accuracy of the power estimation. A third, and somehow rougher approach is to measure the input power to the dc-link of the inverter, and assume a constant value for the inverter efficiency, between 97 and 98% for this power range based on the measurements realized.

A thermal model is developed in order to assess the thermal performance of the machine. The continuous power rating of the machine is defined based on its thermal capabilities. Moreover, there are some parts in the machine that are very sensitive to high temperatures, such as the winding insulation and the rotor permanent magnets. Therefore it is of great importance to have an accurate thermal characterization of the machine. However, there are certain aspects of the machine construction that are difficult to model accurately, and they have to be estimated from empirical correlations and validated with experimental tests. Examples of this are the heat conduction inside the stator slots, the convection due to the air enclosed in the electrical machine and the contact region between the stator core and the outer case.

Chapter 3

Redesign of the E-RWD unit traction machine based on driving cycles

3.1 Motivation

In Chapter 2 the design, manufacturing and testing of an electric traction machine is presented for a particular HEV application: an Electric Rear Wheel Drive (E-RWD) unit. From the feedback gained during the extensive testing of the prototype vehicle shown in Figure 2.26, two main conclusions are drawn:

- The system will benefit from a higher peak torque and power values, in order to enhance the effect of the torque vectoring unit under difficult (low grip) driving conditions.

- The machine works most of the time either at the maximum possible torque or at nearly zero torque, hence it is hard to make a good design based on "nominal ratings". The design should then be based on a more realistic load assumption, such as a driving cycle.

In fact, it is observed that the traction machine presented in Chapter 2 can operate at the maximum power for several minutes before reaching the limit temperature. This suggests that the evaluated machine may not be completely optimal for the E-RWD application, and an alternative design with a lower nominal power rating but potentially higher peak-to-average power ratio could be a more suitable solution.

The question that arises naturally from the previous reasoning is how to find the optimal value of the peak-to-average power ratio for the E-RWD application. To that end, a new design methodology is proposed in the following sections, in which the machine nominal power and the peak-to-average power ratio are derived from simulations of the complete vehicle over certain driving cycles, and most design efforts are devoted to achieving good overloading performance.

3.2   Power level assessment

In order to account for the more realistic load profile, as well as the control strategy and the powertrain configuration, a Matlab-Simulink model is used. The model is essentially the same that is described by K. Johansson and M. Alaküla in [65, 66], and it is described in Appendix C. The top layer of the model is presented in Figure 3.1.
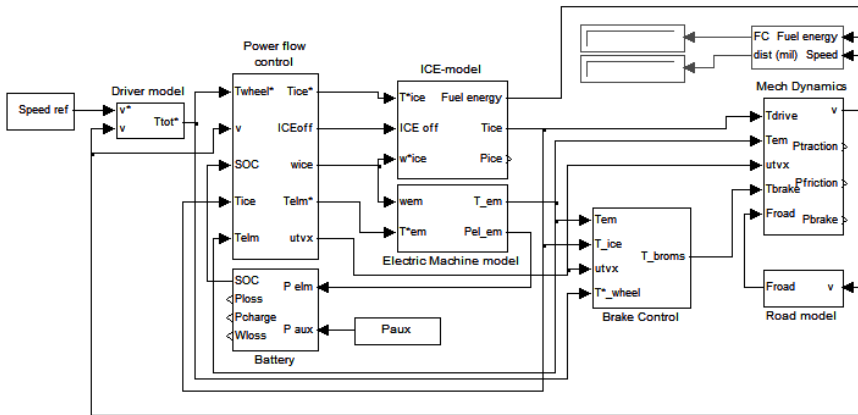

**Figure 3.1:** Simulink model of a Parallel Hybrid Electric Vehicle.

The input to the Simulink model is the driving cycle (speed, altitude and road slope). A Proportional-Integral (PI) controller models the driver's behavior, and generates the requested torque signal, which could be seen as the pressure on the gas or brake pedals, based on the difference between the desired speed coming from the driving cycle specification and the actual vehicle speed. This is in fact the torque (positive or negative) that the driver wants in the wheels, which may be produced by either the electrical machine, the ICE, the mechanical brakes or a combination thereof. The actual torque splitting is decided in the *Power Flow Control* block, based on the battery state of

charge (SOC), the vehicle speed and the characteristics of the ICE and the electrical machine. The control strategy used in the simulations is fairly simple yet powerful. First, the optimal ICE operation point is selected based on its efficiency map, and the most suitable gear is selected aiming to operate the ICE as close to the optimal point as possible. If the battery SOC and the electrical machine power limit allow for it, the electrical machine delivers the difference between the requested torque and the torque delivered by the ICE. However, should the electrical machine be power limited for the actual vehicle speed or the SOC be out of the operational limits, then either the ICE or the mechanical brakes must support.

The system is completed with a number of other blocks modeling the ICE itself, the electrical machine and the battery, plus the *Road Model* block which calculates the drag force (air and rolling resistance) and the *Mech Dynamics* block, in which all forces are added and the actual vehicle acceleration and speed is computed based on Newton's second law.

To find out the best combination of nominal power and peak-to-nominal power ratio for the electric traction machine, a $1800\,kg$ gasoline electric hybrid vehicle with a parallel configuration and a total tractive power of $100\,kW$ is considered. The electric tractive power in the vehicle varies between 0 to $50\,kW$ and the ICE rated power is the remaining up to the total tractive power of $100\,kW$. This vehicle simulated over two different driving cycles: the New European Driving Cycle [67] (which resembles city driving mostly) and the more aggressive US06 [68]. Simulations are run for electric drives thermally designed for 10 to $50\,kW$ nominal power, with an over load capacity spanning from 1 to 4 times.

Figure 3.2a and 3.2b show the fuel consumption (in liters per $10\,km$) obtained for the different electrical machine alternatives over both driving cycles. It should be noticed that the optimal design varies depending on the driving cycle considered, as well as with other aspects such as the driver behavior or the power flow control strategy. Therefore, it is important to know as many of these system details as possible to take most advantage of the simulation model. Looking at the simulation results, a machine rated for $20\,kW$ with a peak-to-nominal power ratio of 3 appears as a good candidate in both driving cycles.
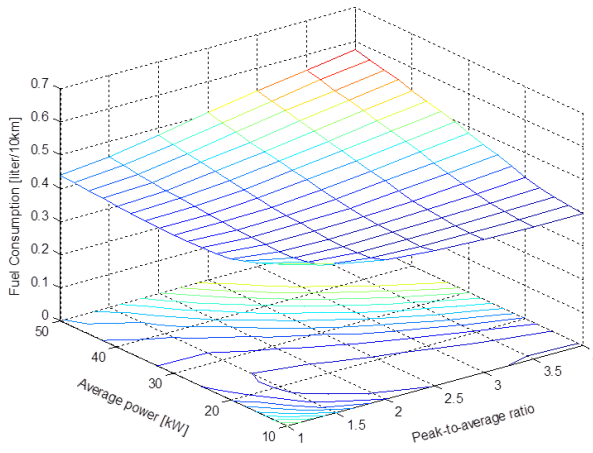
(a) NEDC
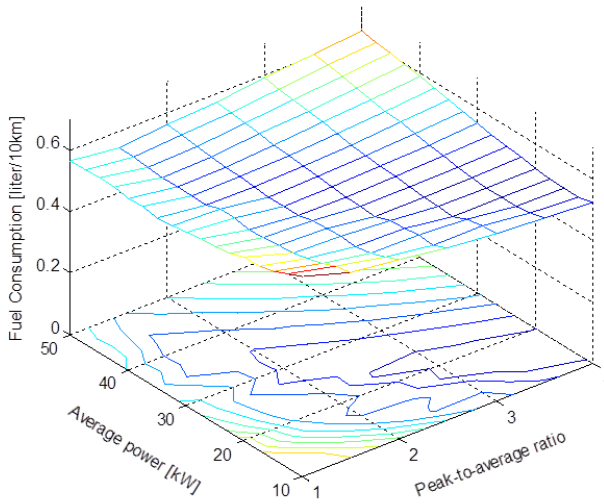
(b) US06

Figure 3.2: Fuel consumption obtained from the Simulink model.

3.3 Electromagnetic redesign

3.3.1 Stator geometry study

When analyzing the machine presented in Chapter 2 operating at high currents both in the FE calculations and in the experimental tests, it is observed that the output torque cannot increase much further than $100\,Nm$ mostly due to magnetic saturation of the stator laminations. Since all technical specifications other than the nominal power rating and peak-to-nominal power ratio are kept the same (see section 2.2), a redesign of the stator geometry is proposed, as an attempt to improve the overloading capabilities of the initial machine.

An intuitive way to reduce the effect of magnetic saturation in the stator laminations is to reduce the slot size, allowing more effective area for the magnetic flux paths. A number of different machine geometries are simulated to investigate the effects of slot size reduction, both in length and width, on the overloading capabilities. All simulated machines are identical, except for two stator characteristics: the slotting factor K_s and the yoke depth factor K_y, both defined in Table 2.3 and Figure 2.6. The larger K_s becomes, the wider the stator slots, hence the narrower the stator teeth. On the contrary, a high K_y implies a thick stator back yoke, therefore reducing the radial length of the slots. Figure 3.3 shows the appearance of the four most extreme cases, corresponding to the corners of the parametric space analyzed, as well as two intermediate points.
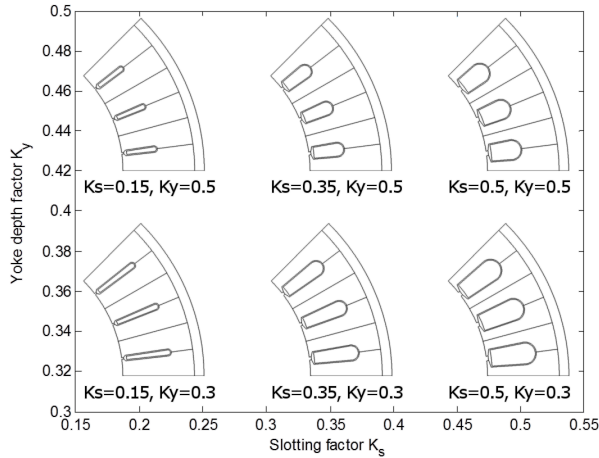

Figure 3.3: Appearance of the stator geometries simulated.

The redesign of the machine is supported by the same software tools described in Appendix B and [26]. For each simulated geometry, i.e. each (K_s, K_y) combination, a first set of 2D stationary thermal analysis determines the nominal current density loading of the windings, for a given maximum temperature of 130 ℃ and natural cooling conditions. Subsequently, the characteristics of the machine are obtained as a function of the stator currents by a second set of stationary electromagnetic FE analysis. Figure 3.4 shows the nominal current density and the total slot current assuming a single-turn winding obtained from the 2D FEA.
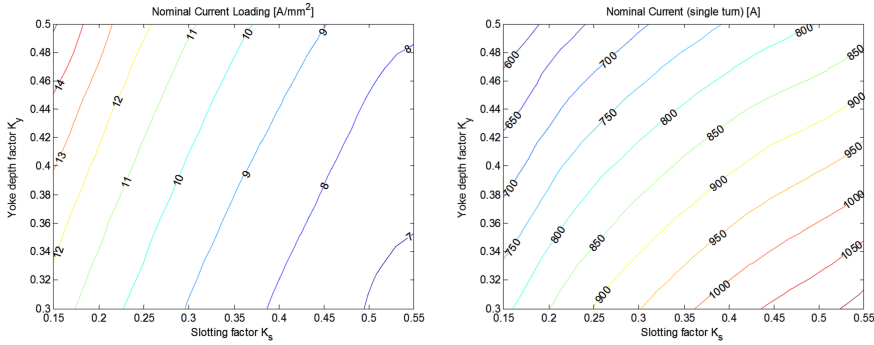

Figure 3.4: Thermal FEA results for the different stator geometries.

From these plots it can be seen that smaller slot areas lead to higher current density loading in the winding. This is an expected result. Since the conduction path for the heat generated inside the slot towards the stator iron is shortened, the cooling of the winding improves. However, the effective copper area is significantly reduced, and even if the current density increases, the total current in the stator winding decreases with the slot size.

Looking at the output torque of the different machines at nominal current in Figure 3.5, it appears that those geometries with larger slots are able to deliver a higher torque. The explanation is straight forward. In a PMSM the torque is produced by the interaction of the stator currents with the magnetic field created by the rotor magnets, plus the reluctance torque component (see equation 2.3). Since the rotor is the same for every machine in this study, and magnetic saturation in the stator laminations is moderate at nominal current loading, a higher winding current produces a higher output torque.
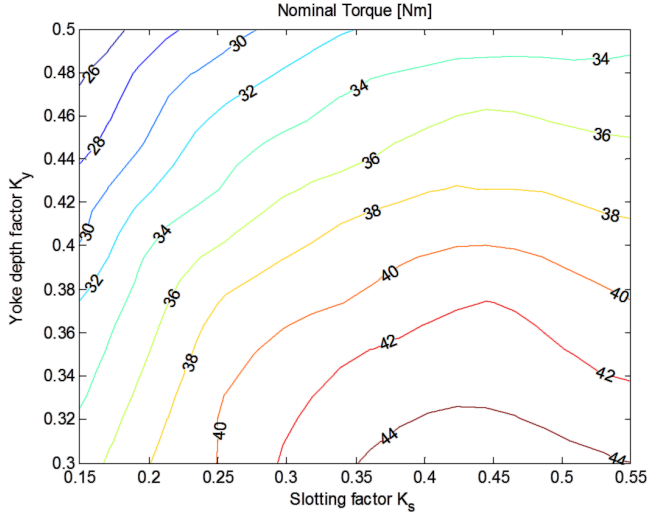
Figure 3.5: Output torque at nominal current.

The situation changes at higher currents though. When the current loading is increased, those machines with large slots become saturated at lower current values, since the effective iron area for the magnetic flux is smaller, and therefore their output torque is lower than that of the smaller slot machines. Saturation can occur in the stator teeth, for those geometries with a high slotting factor (K_s), or in the back yoke when K_y is small. Figure 3.6 shows the output torque of the different machines when loaded with 2, 3, 4 and 5 times the nominal current.

The plots in Figure 3.6 evince that there is an optimal stator geometry for each overloading case, i.e. a combination of tooth width (related to K_s) and back yoke depth (K_y) that gives the maximum output torque, even though other geometries with larger slots are loaded with higher currents. The plot corresponding to 4 times the nominal loading can serve as an example. The optimal stator geometry in this case is defined by $K_s = 0.33$, $K_y = 0.43$. Moving to the right in the plot will imply thinner stator teeth, which will be more saturated and therefore reduce the output torque. In a similar way happens when moving down towards smaller values of K_y, reducing the depth of the stator yoke and making it prone to magnetic saturation. Moving either left or up implies smaller slots. In this case, the reason for the lower output torque is not magnetic saturation, but the reduction of the current due to the smaller slot area.
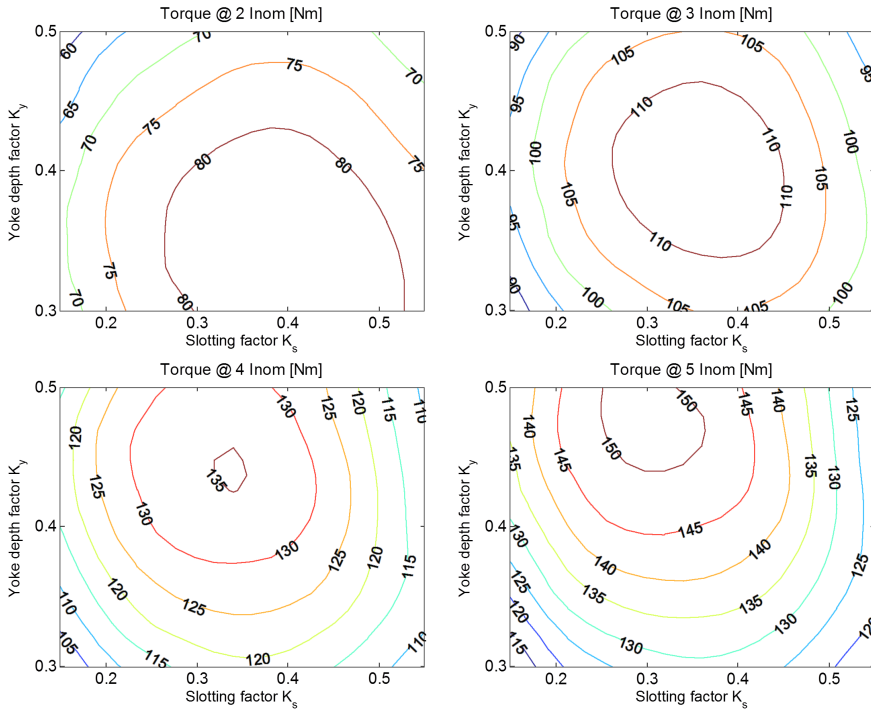
Figure 3.6: Output torque at 2, 3, 4 and 5 times the nominal current.

Another interesting way of analyzing how magnetic saturation of the stator laminations affect the output torque for the different machines is to plot the torque boost ratio, defined as the output torque divided by the nominal torque, when the machines are overloaded. Figure 3.7 presents the torque boost experienced when the different geometries are overloaded by a factor of 2.

It is worth noticing that those geometries with larger slots do not deliver twice the nominal torque when the current is doubled. On the other hand, those machines with smaller slots are able to produce a torque higher than two times the nominal under the same conditions. The thick line in the plot, called the Linear behavior Limit Line (LLL) divides the parameter plane in two, leaving the machines suffering from saturation in the stator core in the lower right part, and those who are not affected by saturation in the upper left part. The LLL actually represents those alternatives that behave linearly, delivering 2 times the nominal torque at double the nominal current loading. Figure 3.8 shows the LLL's resulting from 2, 3, 4 and 5 times the nominal current loading.
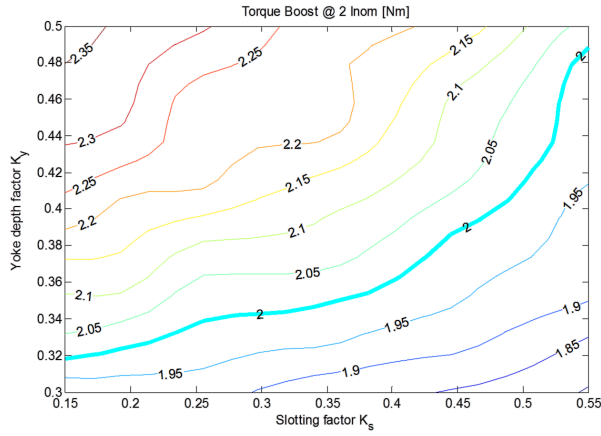
Figure 3.7: Torque Boost at 2 times the nominal current.
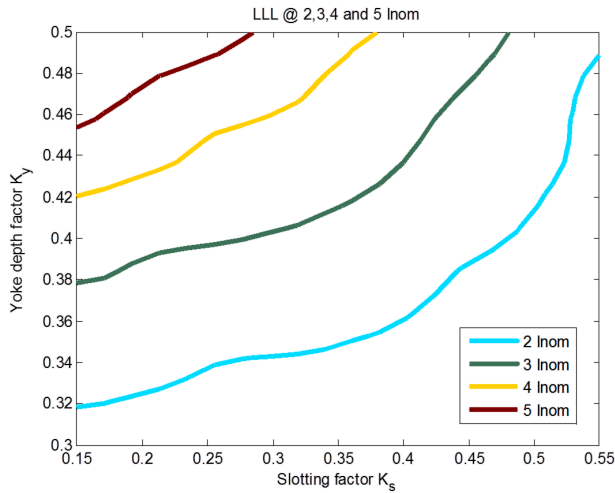

Figure 3.8: Linear Limit Lines (2, 3, 4 and 5 times overloading).

Although saturation in the stator lamination must be reduced to reach a high output torque, in order to maintain the average efficiency as high as possible the slot size cannot shrink too much. Too small slots will lead to high current density values, hence high copper losses. It is the designer's goal to find

a compromise solution, which operates at high efficiency for low power levels while it is still able to deliver a high peak torque when overloaded for short periods of time. Based upon these premises, the selected stator geometry is characterized by a slotting factor $K_s = 0.36$ and a yoke depth factor $K_y = 0.40$, corresponding to the optimal design for a three times overload, as suggested in section 3.2.

3.3.2   Winding configuration

Since the slot size is reduced, the stator winding configuration must be modified consequently. One requirement emerging from the tests in the prototype vehicle is to be able to deliver the peak torque up to a higher speed. Given a certain DC link voltage, this can be achieved by reducing the number of turns, at the expense of a higher current demand to the power electronic converter. If the slot size was kept constant, a lower number of turns should be compensated by a higher number of wires in parallel, to keep the slot fill factor as high as possible. However, the slot size is reduced when compared to the stator geometry presented in Chapter 2, so the number of turns and parallel wires of the winding need to be recalculated.

In order to keep the slot fill factor around 0.45 (see comments in section 2.4.6), the new winding is still a 3-phase winding consisting of 18 parallel wires with 0.8 mm diameter in 9 turns, resulting in a slot filling factor of 0.45. Table 3.1 summarizes the characteristics of the new winding configuration, compared to the previous one.

Table 3.1: Stator winding configuration summary.

	Previous design	New design
Number of turns, N_t (-)	16	9
Number of wires, N_w (-)	17	18
Slot fill factor, K_f (-)	0.454	0.453
Slot area, A_{slot} (mm²)	301.3	180.0

3.4   Thermal modeling of the redesigned machine

So far only 2D FE simulations are used to determine the nominal current loading of the different machine geometries under study. Learning from the previous

design experience, the convection coefficient in this simulations is modified to account for the extra outer case area. Nevertheless, a more accurate description of the heat transfer phenomena inside the machine can be obtained with the thermal model presented in section 2.8.1. This model accounts for 3D effects such as the end winding losses, heat conduction paths from the end windings to the active part of the winding or cooling of the end windings and rotor end rings.

Figure 3.9 shows the temperature evolution at different locations inside the machine calculated with the lumped parameter model, assuming that all the heat is dissipated through natural convection in the outer case surface. The convection-radiation coefficient (h_{ca}) is set to $9\,W/(m^2K)$ following the guidelines exposed in [63]. The plot on the left considers a current density loading in the winding of $8.7\,A/mm^2$, which is the value obtained from the previous FE thermal analysis. In the plot on the right, the current density loading is decreased by 19.5% down to $7.0\,A/mm^2$ in order not to exceed the maximum temperature of $130\,℃$.
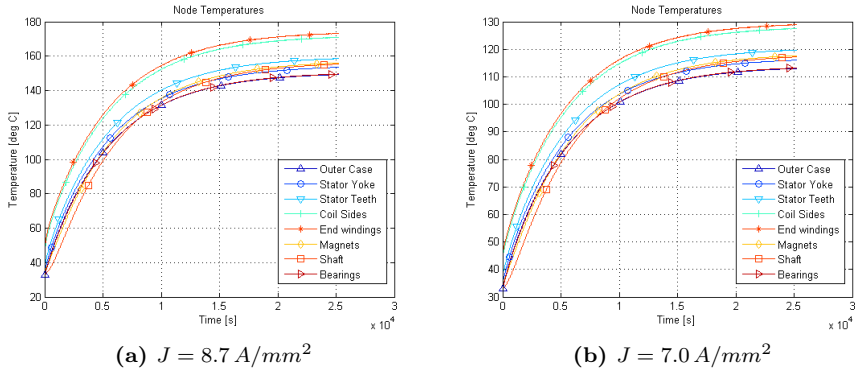

(a) $J = 8.7\,A/mm^2$ **(b)** $J = 7.0\,A/mm^2$

Figure 3.9: Machine temperatures obtained from the lumped parameter model for $h_{ca} = 9\,W/(m^2K)$.

Looking at figures 2.34 to 2.36 in section 2.8.2, in which the measured temperatures are compared to the simulated ones, it seems that a value of $h_{ca} = 12\,W/(m^2K)$ suits better when the machine is in operation, particularly for the outer case temperature. Figure 3.10 shows the results from the lumped parameter thermal model for this new value of h_{ca}.

In this case, just a reduction of 6.5% of the initial current density loading is enough to keep the hot spot temperature below $130\,℃$. As it has been already discussed, the principal differences between the FE thermal model and the

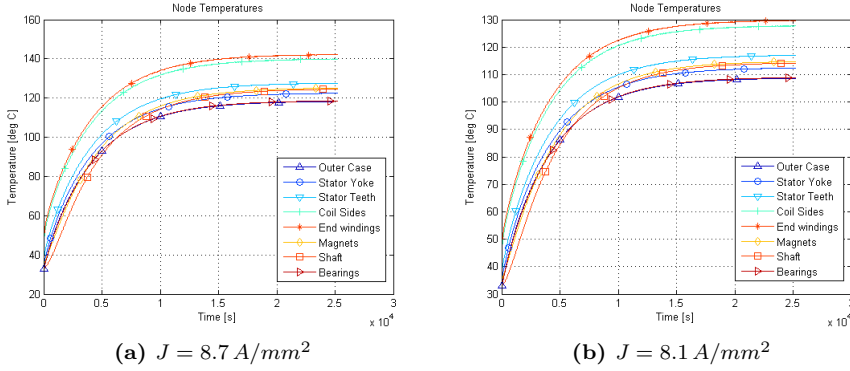**(a)** $J = 8.7\,A/mm^2$ **(b)** $J = 8.1\,A/mm^2$

Figure 3.10: Machine temperatures obtained from the lumped parameter model for $h_{ca} = 12\,W/(m^2 K)$.

lumped parameter model are related to the 2D nature of the first one. The FE model does not consider the end windings, neither the copper losses generated in them, nor their cooling by convection, radiation or conduction of the heat to other parts of the machine. However, since the length of the end windings is closely related to the stator dimensions and these do not vary, the error introduced by the 2D simplification is very similar in all machines analyzed.

The discussion at the end of section 2.8.2 highlights the difficulty of finding an accurate value of the convection coefficient h_{ca}. The experimental measurements on the original machine produce a value of $h_{ca} = 12\,W/(m^2 K)$ with the machine in operation and $h_{ca} = 7\,W/(m^2 K)$ for the natural cooling experiment with the machine at standstill. In the rest of the redesign process, an intermediate value of $h_{ca} = 9\,W/(m^2 K)$ is used, which also corresponds to what is obtained using the empirical correlation proposed by M. Marković et al. in [63].

3.5   Characteristics of the redesigned machine

The proposed redesign stator geometry is characterized by the parameters compiled in Table 3.2. The rotor remains unchanged from the original design, as described in Table 2.13.

From the lumped parameter thermal model, the nominal current loading of the winding is $7\,A/mm^2$, considering just natural convection cooling. With the new winding configuration (see section 3.3.2) the nominal current of the

machine is $44\,A$ (RMS), the nominal torque is $30\,Nm$ and the nominal speed $4550\,rpm$ for a DC link voltage of $300\,V$.

Table 3.2: Redesign stator geometry characterization.

Param.	Value	Description
D_{so}	214.0	(mm) Stator outer diameter
D_{si}	139.7	(mm) Stator inner diameter
L_{fe}	80.0	(mm) Active machine length
L_{tot}	160.0	(mm) Total machine length
N_p	8	(-) Number of poles
K_y	0.40	(-) Stator yoke depth factor
K_s	0.36	(-) Stator slotting factor
N_q	24	(-) Number of slots
d_{sl}	2.0	(mm) Slot opening

The torque, flux and efficiency maps, as well as the output torque and power characteristics and Maximum Torque Per Ampere (MTPA) line are shown in Figure 3.11. The currents are expressed in the rotor reference frame (x,y), taking into account the actual winding configuration. Please refer to Appendix B and [26] for further details on the machine characteristics calculation process.

It is worth noticing how the MTPA line behaves linearly up to approximate $241\,A$, $100\,Nm$, which is approximately 3 times the nominal torque. This is a clear improvement when compared to the original design, which suffered from saturation already at two times the nominal current. However, when looking at the output power, the redesigned machine is able to provide $14.3\,kW$ at nominal speed ($30\,Nm$ @ $4550\,rpm$) and a somewhat higher $16.2\,kW$ @ $7020\,rpm$, which is lower than the $20\,kW$ suggested by the power level assessment in section 3.2. In the next section, different ways of increasing the nominal power are discussed, and a modification of the machine described here is proposed to that end.
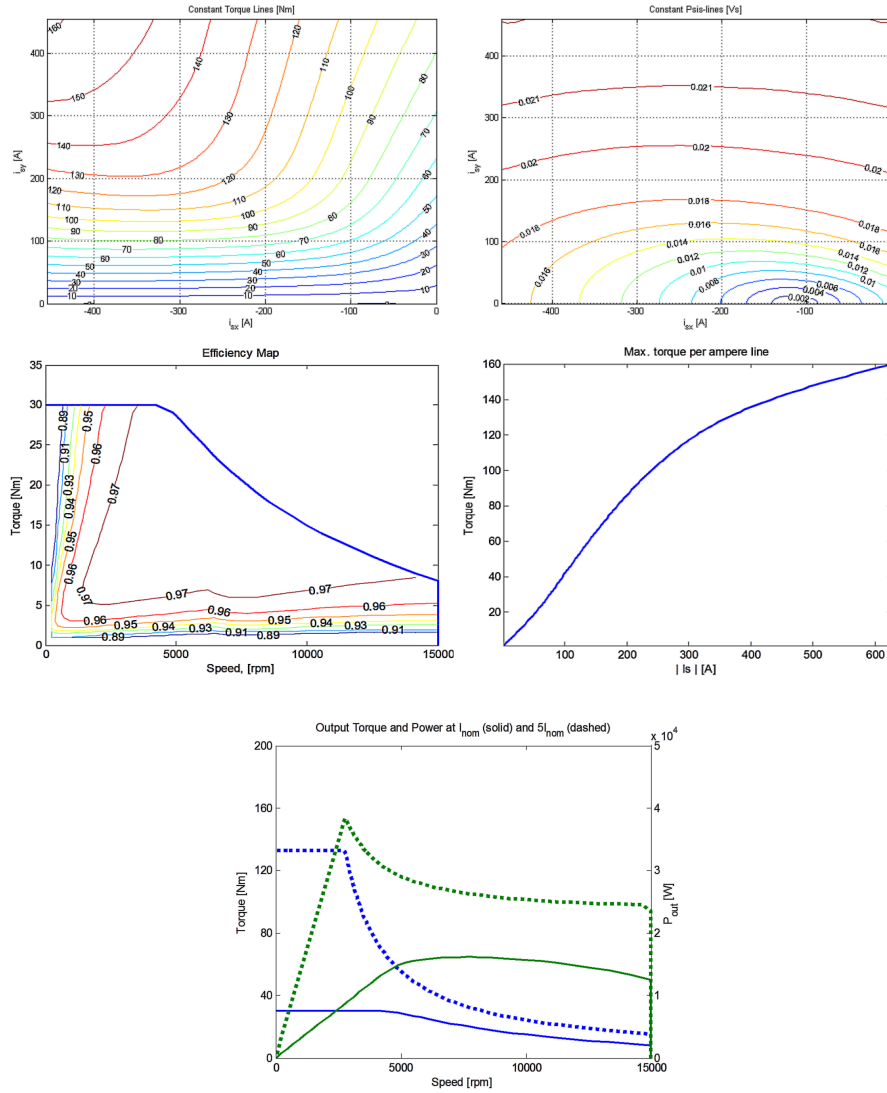
Figure 3.11: FE simulation results for the redesigned machine.

3.6 Redesigned machine with enhanced cooling

The main limitation hindering the increase in nominal power comes from the cooling capabilities of the machine. The calculation of the nominal current loading is discussed in the previous section, in which a thermal model is used to ensure that the maximum temperature is not exceeded anywhere in the machine. Therefore, it comes clear that if the cooling conditions are enhanced, the nominal performance of the machine, understood as the torque or power that could be delivered indefinitely without overheating, will improve.

Moreover, if it is not possible to improve the cooling of the machine, a possible way of increasing the nominal power is to strengthen the excitation field from the rotor, either increasing the amount of permanent magnet material or exchanging it for another one with higher remanence. For the same winding current, a machine with a stronger excitation field will produce a higher output torque. However, although the copper losses will not change since the current is the same, the higher excitation field will most likely result in higher iron losses, thus reducing the nominal current rating. This means that it is not sufficient to just strengthen the excitation field in order to increase the output power, but the machine should also operate more efficiently.

In this section, a new modification of the stator geometry is proposed in order to improve the cooling conditions of the machine, while the rotor remains unchanged. In every design considered so far in this thesis all the losses generated are dissipated by natural convection through the outer casing. Perhaps, the most immediate way to improve the cooling capabilities of such machines is to add cooling fins to the outer surface, hence increasing the effective cooling area. Another alternative is to use forced convection, providing air at a certain speed by means of a fan or a compressor. In this way the convection coefficient will increase significantly, improving the cooling capabilities of the machine as well. If this is not sufficient, a liquid could be used as a cooling fluid instead of a gas. Due to their physical properties, liquids are more effective coolants than gases, however, they require a number of extra components that, even if their installation is feasible, add an extra cost to the system. Besides, there are other advanced cooling concepts like, for example those based upon phase changing cooling media, that are not considered for this application.

In the E-RWD unit there is already an oil tank to provide lubrication for the mechanical transmission parts. With minor modifications in the original system, this oil could also be used to cool the electric traction machine. The

most common approach for liquid cooling of electrical machines consists on circulating the coolant, usually a mixture of water and glycol, through channels cut in the outer casing in a so called water jacket. In this case, the heat generated in the windings inside the stator slots has to travel a long way out of the machine, first to the edge of the slot, then through the slot insulation liner to the stator lamination, moving out radially to the outer casing, and finally dissipated by convection inside the cooling channels. Along this conduction path, there are several thermal resistances that add up, resulting in a significant temperature difference between the hotspot and the coolant.

To reduce this temperature difference and cool the machine more effectively, the heat conduction path may be shortened, moving the heat sink (i.e. the coolant) as close as possible to the heat source (i.e. the windings). Integrating the cooling circuit inside the stator slots seems a difficult task. Even if the coolant fluid is not conductive, so safety is not compromised in case of leakage, the cooling channels will take some place inside the slots, affecting the fill factor negatively. For this reason, it is decided to move the cooling channels from the outer case down to the stator laminations instead. By doing so, the thermal resistance corresponding to the contact region between the stator laminations and the outer case is eliminated from the conduction path.

The first questions to be sorted are the number of cooling channels and their location. From a cooling perspective, it is desirable to have one channel as close as possible to each heat source, i.e. each stator slot. However, there are a few aspects that should be taken into account:

- a cooling circuit with fewer channels is definitely easier to implement. When the number of channels increases, distributing the coolant evenly among the different channels becomes more difficult and it may require extra design effort, incorporating fluid dynamic analysis to the already existing thermal and electromagnetic ones.

- when placed in the stator laminations, the cooling channels will reduce the effective area available for the magnetic flux circulation. If placed incorrectly, the cooling channels could cause local magnetic saturation of the laminations, impairing the performance of the machine.

- the thermal conductivity of the stator laminations along the lamination plane is high, meaning that there is some freedom in the placement of the cooling channels. Moving the channel away from the slot will result in a little increase in the thermal resistance, hence a small temperature increase as long as the heat only travels through the laminated steel.

Two alternative channel arrangements are implemented in the design

software, and simulated to further investigate the effect of the cooling channels both on the nominal power rating of the machine and on its overloading capabilities. While the power rating is expected to be higher due to enhanced cooling, the overloading potential could be negatively affected if saturation of the stator laminations increases. In both cases the cooling channels are placed in the stator back yoke, just on top of a tooth; this is where the cross sectional area for the magnetic flux is the largest, and therefore the negative effects of the channels on the magnetic saturation are minimized.

Figure 3.12 shows both layouts. In both cases the channels are distributed evenly along the 360 degree circumference and antiperiodic boundary conditions apply, allowing to simulate just one eighth of the complete machine.
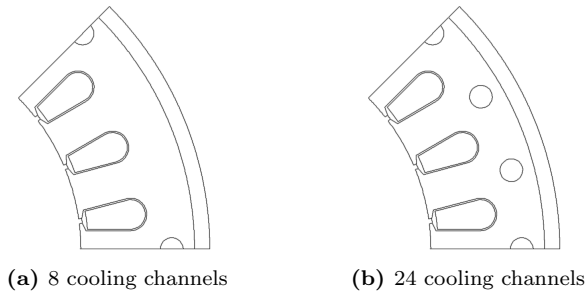

(a) 8 cooling channels   (b) 24 cooling channels

Figure 3.12: Stator geometry models for enhanced cooling.

A quick analysis of the simulation results reveals that cooling is more effective in the 24-channel alternative. It is not difficult to understand that if the same conditions are assumed for both cases (i.e. same convection coefficient inside the cooling channels) in order to dissipate the same amount of heat, the diameter of the channels in the 8-channel alternative must be larger than its 24-channel counterpart. The effects of the larger channels in the overloading capabilities of the machine is noticeable, and therefore it is decided to continue with the 24-channel design, despite its higher complexity.

A new design parameter labeled K_{cd} is introduced now to characterize the size of the cooling channels. K_{cd} is defined as the ratio between the diameter of the cooling channel and the stator yoke depth, denoted with a in Figure 2.6a. Both stator geometries in Figure 3.12 feature $K_{cd} = 0.5$.

A comparative analysis for different sizes of the cooling ducts is carried out, assuming a constant convection coefficient inside the ducts of h_{cd} of

$600\,W/(m^2K)$ for all cases. The methodology for this analysis is analogous to the previous studies and it is detailed in Appendix B. The results from this comparative analysis are summarized in Table 3.3 below.

Table 3.3: Comparative study for different cooling channel size.

K_{cd}	J_{nom} (A/mm^2)	$I_{s,nom}$ (A)	T_{nom} (Nm)	$T @ 3I_{s,nom}$ (Nm)	$T @ 5I_{s,nom}$ (Nm)
0.3	10.88	115.2	48	125	152
0.4	11.00	116.6	48	123	149
0.5	11.14	118.0	48	118	144
0.6	11.21	118.8	47	111	137

In light of the figures in Table 3.3 some conclusions can be drawn. Looking at the values obtained for the nominal current density (and/or the nominal current, since neither the slot size nor the winding layout are changed) it is clear that, for a constant value of the heat convection coefficient, doubling the size of the cooling channel from $4.46\,mm$ diameter for $K_{cd} = 0.3$ to $8.92\,mm$ for $K_{cd} = 0.6$ has very little impact in the cooling of the machine, with just 3% increase of the nominal current loading according to the thermal FE simulation results. However, as it was pointed out before, larger cooling ducts will reduce the effective cross sectional area of the magnetic flux path, which leads to magnetic saturation of the stator core at high loading. This is also noticed in Table 3.3, since those machines with larger cooling ducts are able to deliver lower torque when overloaded to 3 and 5 times their nominal current. Another way of illustrating this saturation effect is by looking at the MTPA line. In Figure 3.13, the MTPA line for the four alternatives considered is plotted together with the original geometry without cooling ducts. In the plot, the torque boost ratio is presented instead of the absolute torque value for the sake of comparison.

Looking at Figure 3.13, the first remarkable thing is the significant difference existing between the original machine geometry (without cooling channels) and the other alternatives. This difference becomes more apparent because the plot presents the torque boost ratio instead of the absolute torque value.
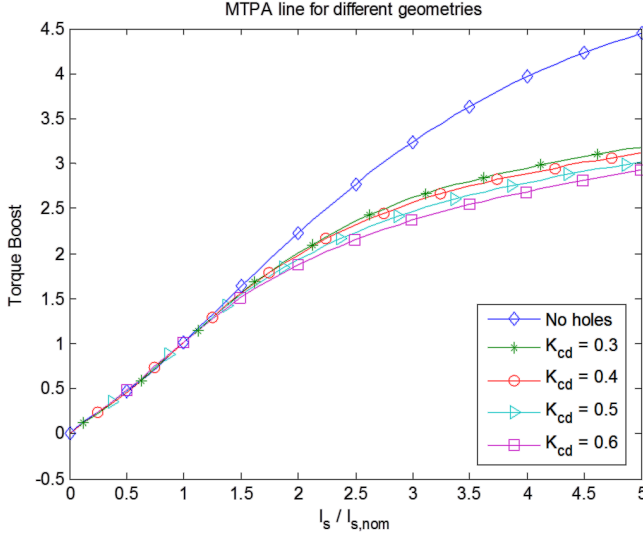
Figure 3.13: MTPA lines for the different cooling channel sizes.

Both the stator tooth and back yoke sizes are selected for behaving linearly up to 3 times the nominal current loading, which was estimated in $8.7\,A/mm^2$ from the 2D FE thermal simulations. Hence, saturation will occur when the current density increases over $26.1\,A/mm^2$. However, since the machines featuring enhanced cooling start from a higher nominal current density value (around $11\,A/mm^2$ according to the figures presented in Table 3.3) they will reach saturation at approximately 2.5 times the nominal current. Besides, the reduction of effective cross sectional area for the magnetic flux due to the cooling channels brings this value further down. This effect motivates as well the differences between the different machines simulated, as it has been already discussed.

Since large cooling ducts compromise the torque capabilities of the machine without improving significantly the nominal operation conditions, the machine with $K_{cd} = 0.3$ is the preferred alternative among the ones simulated. Smaller cooling channels could be simulated, nevertheless there is a lower limit for their cross sectional area, due to the underlying increase in pressure drop. In fact, in order to know in detail the characteristics of the fluid flow inside the cooling channels a Computational Fluid Dynamics (CFD) model is created. In all the previous simulations the same value of $600\,W/(m^2 K)$ was assumed for the convection coefficient inside the channels h_{cd}. However, this is not the case in reality. The convection coefficient is dependent on the cross sectional

area of the channel, as well as the velocity and nature of the flow and the properties of the coolant fluid [62]. The CFD simulations provide a more accurate value of the convection coefficient for different coolant flows, as well as the corresponding pressure drop along the channel. Two different coolants are considered in the simulations for the sake of comparison, Statoil TransWay (a mechanical transmission oil, which is already used in the E-RWD system) and DOWTHERM J (a heat transfer fluid) [69, 70]. The results of the CFD analysis are presented in Table 3.4.

Table 3.4: CFD simulation results for different flow rates.

Coolant	Flow rate	Velocity	Δp	h_{cd}
	(l/min)	(m/s)	(Pa)	(W/m^2K)
Statoil TransWay	0.4	0.018	15.60	246
	0.6	0.027	23.82	273
	0.8	0.036	32.13	294
	1	0.044	39.60	312
	2	0.089	82.98	381
	3	0.133	127.62	430
	5	0.222	224.66	505
DOW THERM J	0.4	0.018	1.25	233
	0.6	0.027	2.08	262
	0.8	0.036	3.00	286
	1	0.044	3.89	305
	2	0.089	9.97	386
	3	0.133	17.36	446
	5	0.222	35.80	539

Looking at the figures in Table 3.4 it can be concluded that there are no significant differences between the values of the convection coefficient for both coolants. Nevertheless, there is a significant difference in the pressure drop along the channel, mostly due to the difference in viscosity. This will affect the power needed to pump the coolant fluid through the channels, therefore it should be taken into account when calculating the overall system efficiency. Since transmission oil is already available in the system, and a suitable oil pump is a common component in the automotive industry so it does not involve much extra design work, the rest of the analysis will consider TransWay transmission oil as a coolant, with a flow rate of $0.4\,l/min$.

Similarly to the previous designs, in addition to the 2D FE thermal analysis performed, a 3D lumped parameter model of the electrical machine is used to compute the temperature distribution more accurately. The resulting thermal network is shown in Figure 3.14. Compared to the model presented in Figure 2.28 a new thermal resistance is added, connecting the temperature of the stator yoke to the coolant temperature (highlighted in Figure 3.14).
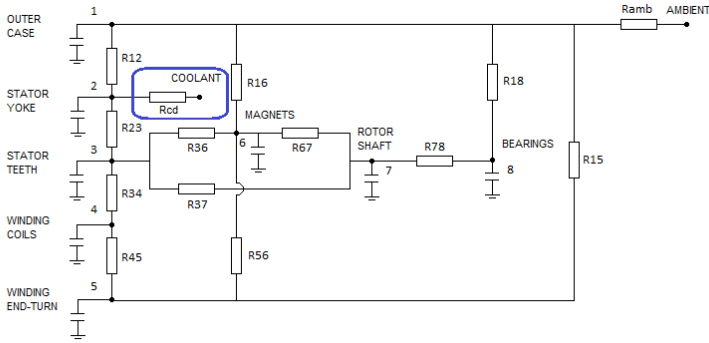

Figure 3.14: Thermal network including cooling channels.

The new thermal resistance R_{cd} represents the convective heat transfer inside the channels, and it is calculated from the convection coefficient h_{cd} and the inner area of the channels A_{cd} according to equation (2.28). With $h_{cd} = 246\,W/(m^2K)$ from the CFD simulations, and considering 24 cooling channels of $4.46\,mm$ diameter, the calculated thermal resistance corresponding to convection inside the channels is $R_{cd} = 0.15074\,K/W$.

From the lumped parameter model simulations, the nominal current density of the machine with enhanced cooling reaches $9.7\,A/mm^2$, increasing about 38.6% compared to the natural cooling alternative. Figure 3.15 presents the temperature evolution at different locations inside the machine calculated with the lumped parameter model, assuming that part of the losses are dissipated inside the cooling channels and the rest through natural convection in the outer case surface, with a convection coefficient of $h_{ca} = 9\,W/(m^2K)$ as in the previous case.
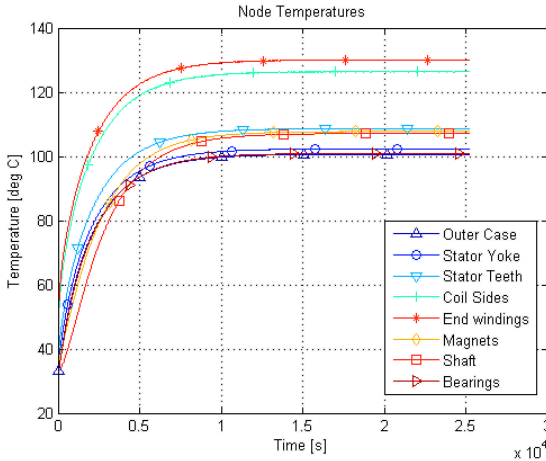
Figure 3.15: Machine temperatures obtained from the lumped parameter model with enhanced cooling. $J = 9.7\,A/mm^2$

Taking into account the winding configuration described in section 3.3.2, the nominal current of the machine with enhanced cooling is $62\,A$ (RMS), the nominal torque is $44\,Nm$ and the nominal speed $4035\,rpm$ for a DC link voltage of $300\,V$.

Figure 3.16 shows the torque, flux and efficiency maps, as well as the output torque and power characteristics and Maximum Torque Per Ampere (MTPA) line. The currents are expressed in the rotor reference frame (x,y) as for the previous cases.

Looking at the output power resulting from the simulations, the machine with enhanced cooling is able to provide $18.6\,kW$ at nominal speed ($44\,Nm$ @ $4035\,rpm$), being able to reach $22.5\,kW$ @ $12600\,rpm$, which fulfils the requirements posed in section 3.2. On the other hand, the overloading capabilities of the machine are not as good as before. From the MPTA line it can be seen that the torque behaves linearly up to approximately 2.4 times the nominal current ($105\,Nm$ @ $258\,A$). The reasons for this are discussed previously in this section.
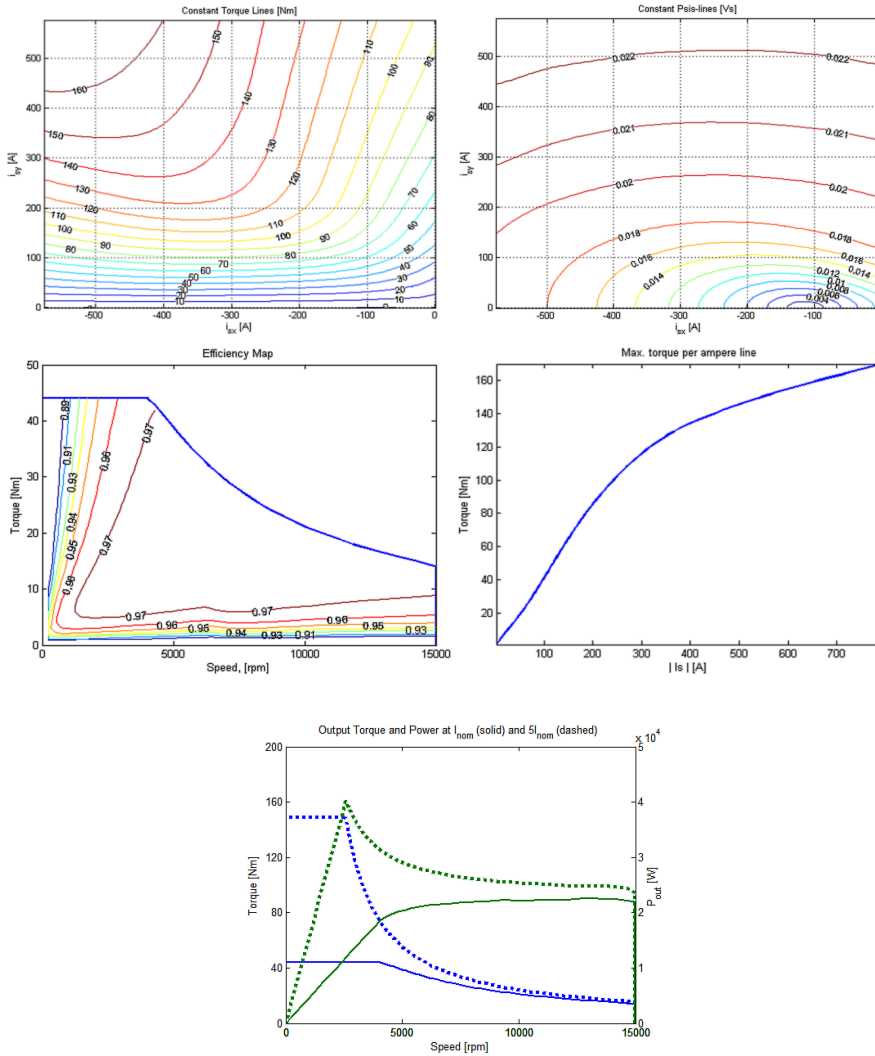
Figure 3.16: FE simulation results for the machine with enhanced cooling.

3.7   Summary of the redesign process

The electric traction machine for the E-RWD unit presented in Chapter 2 is redesigned in response to the feedback received during the vehicle tests. The redesign is based on simulations of the complete vehicle, which are believed to provide more accurate estimations of the real power needs and the peak-to-average power ratio [71]. However, more detailed knowledge of the driving cycle, the system topology and the control strategy adopted are required in order to succeed. This information is not always easy to find, therefore it is advised that the designer works in collaboration with the final customer or user when possible, and asks for it already at the earliest design stages.

A first redesign is carried out assuming only natural convection cooling of the machine, resulting in a reduction of the stator slot size to allow for higher flux linkage with reduced saturation, thus improving the overloading capabilities of the initial design in Chapter 2. The new machine is able to provide 3 times the nominal torque when overloaded with 3 times the nominal current as suggested from the complete vehicle simulations, although the nominal output power does not reach the $20\,kW$ target value.

A higher nominal power is achieved through further modification of the stator geometry. The objective now is to improve the cooling of the machine in order to be able to increase the current loading of the winding without exceeding the specified maximum temperature. In the proposed solution, cooling channels are cut from the stator laminations, and a coolant fluid is circulated through them. Different channel sizes and locations are investigated, as well as two different coolants. The enhanced-cooling design delivers up to $22.5\,kW$ but its overloading characteristics are slightly derated, and saturation effects start to be noticeable after 2.4 times the nominal current. Table 3.5 compiles the most significant characteristics of the three machine designs, the initial one from Chapter 2, the first redesign with just natural convection cooling and the enhanced-cooling one.

In addition, it is worth remembering that only the stator is modified along this chapter, while the rotor remains unchanged. Nevertheless, a redesign of the rotor could also help to achieve both the $20\,kW$ nominal power and the peak-to-average power ratio of 3 suggested from the driving cycle simulations. [41, 72]

Table 3.5: Redesign process summary.

	Initial	**Redesign**	**Enh. cooling**
$\mathbf{J_{nom}}$ (A/mm^2)	6.5	7.0	9.7
$\mathbf{I_{nom}}$ (A, RMS)	39	44	62
Win. (N_t/N_w)	16/17	9/18	9/18
$\mathbf{P_{nom}}$ (kW)	12.3	14.3	18.6
$\mathbf{T_{nom}}$ (Nm)	$42\,(@2800\,rpm)$	$30\,(@4550\,rpm)$	$44\,(@4040\,rpm)$
$\mathbf{T_{3Inom}}$ (Nm)	$94\,(@2100\,rpm)$	$97\,(@3060\,rpm)$	$120\,(@2890\,rpm)$
$\mathbf{T_{5Inom}}$ (Nm)	$114\,(@1870\,rpm)$	$133\,(@2740\,rpm)$	$149\,(@2560\,rpm)$

Chapter 4

E-RWD unit traction machine: direct cooling alternative

4.1 Laminated winding history

As it is discussed in the last sections of Chapter 3, an effective way of improving the cooling of an electrical machine is to bring the heat sink as close to the heat source as possible. Although feasible, it is very difficult to integrate the cooling elements inside the windings in a conventional machine. Particularly in a conventional radial flux machine with a laminated stator, such as those presented in Chapters 2 and 3, one of the main struggles is to fit as many copper wires as possible into the stator slot, in order to increase the slot filling factor, reduce the current density in the wires hence the copper losses, and reduce the amount of air inside the slots hence improving the thermal conductivity. Placing cooling channels inside the stator slots will leave less available space for the winding, and even though the cooling is improved, further reducing the already low slot filling factor does not seem a good idea. [73–75]

At the same time as the work presented in this thesis is carried out, in the Industrial Electrical Engineering and Automation division (Lund Faculty of Engineering) Tech. Lic. Conny Högmark, in the course of his research on production techniques for pre-assembled windings for molded electrical machines, developes the laminated winding concept. In a laminated winding, instead of a bundle of wires, the current flows in a wound strip of a good electrical conductor, most commonly copper or aluminum. The manufacturing

process for such a coil has the potential to be rather simple, the slot filling factor can be significantly increased and what is most important for molded machines, the resulting winding has extremely good geometric tolerances. [76, 77]

From a thermal perspective, the laminated winding opens the door for a revolutionary cooling approach: direct winding cooling. If a small space is allowed between consecutive turns forming channels in the axial direction of the machine, it is possible to circulate a cooling gas through them, removing the heat directly from the heat source, i.e. the winding. This proves to be a very effective way of cooling the machine, as shown in the following sections. In fact, by varying the cooling conditions (i.e. the coolant gas flow or its inlet temperature) different nominal operation points can be defined, understood as those loading points that can be sustained indefinitely without exceeding the maximum temperature limit. This actually means that the machine can be overloaded (i.e. operated above its rated torque and/or speed) for as long time as needed, however to the cost of the extra cooling which has an impact on the overall system efficiency when overloading.

An electric traction machine for a vehicle application must be designed for the worst load case, which is usually driving uphill with a certain slope, at a specified speed and with a given weight load, no matter what type of vehicle is targeted. This usually results in oversized machines, that very seldom deliver full output power; implying that most of the time the vehicle may be carrying an electric traction machine which is larger, heavier, less efficient and more expensive than what is actually needed. However, with the direct cooling alternative the design could be downsized to maximize the efficiency under the most common load demands, and if the maximum power is ever needed, it can be delivered providing extra cooling to the windings, although at an efficiency slightly lower than the oversized alternative. This possibility has an analogy in the combustion engine world where the development trend is towards smaller and more efficient combustion engines with increased overload capabilities by supercharging.

4.2   Geometry description

The main idea behind the laminated winding concept is to create a concentric wave winding from a conductor strip, either copper or aluminum, cutting from it the holes in which the stator teeth will fit, from one and the other edge of the strip alternatively. Since the strip is later rolled up to form a coil, the distance between the teeth holes increases with the number of turns.

Once the winding is formed, it is placed on rubber supports. These supports hold the winding in place, avoiding undesired movements that could cause short-circuits between the different conductive parts, either the winding turns or the stator core, and even destroy the machine. Moreover, they ensure that the turns are correctly spaced so that the coolant gas is evenly distributed between the different channels. It is important that the electrical conductivity of these supports is low, since the windings are excited with high voltages, and otherwise current will leak from the windings to the stator teeth.

The stator teeth fit inside the rubber supports. They can be manufactured from laminated steel if they are designed as an extruded 2D geometry, or from a soft magnetic composite (SMC) by sintering or molding if more complex geometries are desired. The stator teeth are also integrated in the stator yoke, completing the magnetic circuit. The stator yoke can also be made of either laminated electrical steel or SMC.

The order of assembly varies depending on the geometry of the different parts. Figure 4.1 shows a sector of a laminated winding stator, illustrating the different parts and how they fit together.
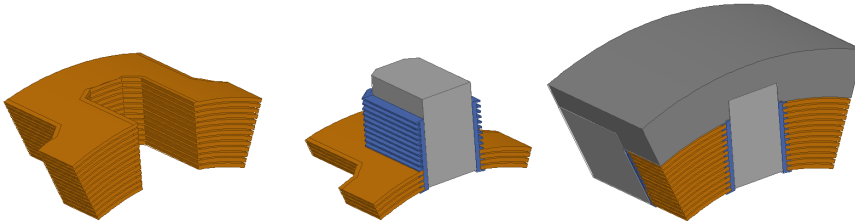

Figure 4.1: Laminated winding stator parts.

In the rest of this chapter, the stator teeth and yoke and the rotor stack are assumed to be made of laminated electrical steel M250-35A ($0.35\,mm$ thick with maximum loss of $2.50\,W/kg$ at $1.5\,T$ and $50\,Hz$) unless stated otherwise [43]. The stator yoke laminations are stacked in the axial direction, while the teeth are stacked in the circumferential direction, although other alternatives are also possible [77]. The winding supports are modeled as thermal conductive silicone based material (SC-320 produced by LORD Corp. [78]), while the winding turns and the outer machine case are made of aluminum. The permanent magnets are assumed of grade N35SH from Sura Magnets [44], as for the previous cases described in section 2.5.

The parameters that characterize the laminated winding stator geometry are listed below. Figure 4.2 graphically illustrates some of these.

Laminated winding stator parameters (see Figure 4.2):

r_{si} Inner stator radius (m).

r_{so} Outer stator radius (m).

h_{lam} Winding lamination thickness (m).

h_{air} Height of the channel between turns (m).

h_{rub} Total rubber support thickness (m).

d_{rub} Effective rubber insulation thickness (m).

d_{thy} Length of the tooth insert in the yoke (m).

L_{seg} Active length of the stator segment (m).

K_y Stator yoke depth factor $K_y = a\,/\,b$ $(-)$.

K_s Stator slotting factor $K_s = \alpha\,/\,\delta$ $(-)$.

K_{th} Portion of the stator segment length covered by a tooth $(-)$.

K_{thl} Tooth bevel form factor in axial direction $(-)$.

K_{thw} Tooth bevel form factor in circumferential direction $(-)$.

Calculated values:

V_1 Tooth axial length (m). $V_1 = K_{th}\,L_{seg}$

V_2 Tooth bevel axial length (m). $V_2 = K_{thl}\,V_1$

H_1 Tooth width (m). Derived from the slotting factor K_s

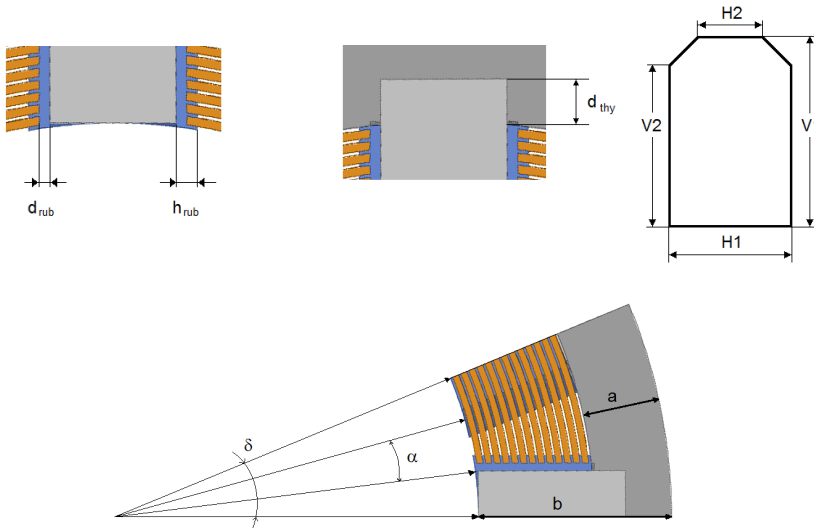H_2 Tooth bevel width (m). $H_2 = K_{thw}\,H_1$

Figure 4.2: Laminated winding stator geometry details.

4.3 Design objective

The laminated winding concept is a new development, therefore there is very little experience and limited data supporting its suitability for electric traction machines so far. The work published by Högmark to date focuses mostly on the production and manufacturing aspects while Kjellstrand and Akujärvi deal with the cooling capabilities of such windings. In addition, Andersson proposes a laminated winding design as a traction machine for a heavy vehicle application. [76, 77, 79–81]

The objective of this chapter is to evaluate the performance of a laminated winding machine in an E-RWD application, subjected to the same technical specifications and constraints used in Section 2.2. The new design is also benchmarked against the previous alternatives presented in Chapters 2 and 3.

Analogously to Chapter 3, the rotor design remains unchanged, equal to the one resulting from the optimization process in Chapter 2, thus only the influence of the stator is analyzed. Moreover, in the case of the laminated winding configuration, for each design there are two situations to be considered: when no direct cooling is applied (i.e. there is no gas circulation between the turns) and when maximum direct cooling is applied.

4.4   Thermal analysis

As for the previous designs, the maximum current that a certain laminated winding machine can withstand is determined through its thermal analysis. In this particular case, a wide range of different cooling conditions can apply, depending on the coolant flow and inlet temperature mostly. Since the most remarkable thermal feature of the laminated winding concept is the possibility to dissipate the conductor losses directly where they originate, in the stator windings, the thermal analysis is initially limited to this type of losses and the direct winding cooling.

Due to the high computational cost of 3D FE simulations, a Matlab program based on analytical and empirical correlations is created. This model roughly analyzes the cooling capabilities of a laminated winding stator and helps fast-identifying the most promising stator configuration, i.e. that one that allows for maximum current loading for the given conditions. Subsequently, that geometry is modeled in 3D FE in order to have a deeper understanding of the temperature distribution in the stator and to validate the machine selection.

4.4.1   Theoretical model

This model constitutes the first step in the thermal analysis of the laminated winding concept. As mentioned above, the computation time of this model is several orders of magnitude shorter than for the 3D FE model. Therefore it is used to investigate the influence of different design parameters on the loadability of the machine, allowing for a fast identification of the most promising design from a direct cooling point of view.

The model considers just one cooling sector, defined as the space between two adjacent stator teeth, the equivalent to the stator slot in a conventional machine. In turn, one sector comprises several cooling channels, which are the gaps between two consecutive turns (see Figure 4.3). A lumped parameter model of each turn is derived, in order to calculate the temperature in the conductors, and ensure that the maximum temperature limit is not exceeded.
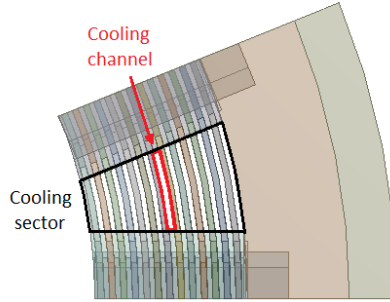
Figure 4.3: Illustration of the cooling sector and cooling channel.

Since both the coolant and the winding material properties are dependent on the temperature values at the different points and these are unknown from the beginning, an iterative process is required. The winding temperatures are initially assumed, and the following sequence is repeated until convergence.

1. *Convection coefficient and friction factor calculation.* Based on the physical dimensions of the design, the coolant flow and the properties of both the coolant gas (assumed to be air) and the winding laminations (aluminum) the convection coefficient and friction factor are calculated based on empirical correlations.

   The correlations used are:

   a) Laminar flow ($Re < 2300$). The relative distance λ is defined as

   $$\lambda = \frac{x}{D_h \, Re \, Pr} \tag{4.1}$$

   where x is the distance along the flow path, D_h is the hydraulic diameter of the channel, and Re and Pr are the Reynolds and Prandtl numbers respectively. The Nusselt number is given by the following equations, adapted from the Shah correlation for thermally developing, hydrodynamically developed laminar flow with uniform wall heat flux, for non-circular ducts [82]:

   $$Nu = 2.7646 \, \lambda^{-1/3} \qquad \text{if } \lambda < 0.03 \tag{4.2}$$

   $$Nu = 6.49 + \frac{0.0722}{\frac{x}{D_h} \, Re \, Pr} \qquad \text{if } \lambda \geq 0.03 \tag{4.3}$$

The friction factor in the laminar case is given by:

$$f_d = \frac{96}{Re} \tag{4.4}$$

b) Turbulent flow ($Re \geq 2300$). The Nusselt number is calculated according to the Gnielinski equation, applicable for constant heat flux boundary conditions when $0.5 < Pr < 2000$ and $2300 < Re < 5\ 10^6$ [62]:

$$Nu = \frac{\frac{f_c}{8}\,(Re - 1000)\,Pr}{1 + 12.7\,\sqrt{\frac{f_c}{8}}\,(Pr^{2/3} - 1)} \tag{4.5}$$

Where f_c is an approximation to the friction factor given by:

$$f_c = (0.79\,\ln(Re) - 1.64)^{-2} \tag{4.6}$$

The Darcy friction factor, used to estimate the pressure drop over the channel, is calculated directly from the implicit Colebrook equation, where ε is the surface roughness height. [83]

$$\frac{1}{\sqrt{f_d}} = -2\,\log\left(\frac{\varepsilon}{3.7\,D_h} + \frac{2.51}{Re\,\sqrt{f_d}}\right) \tag{4.7}$$

2. *Air temperature evolution.* As the air flows through the channel it absorbs the heat from the winding laminations, thus increasing its temperature. If the channel is divided axially in smaller sections, and the lamination temperature is assumed constant over each section, the total heat transferred to the air in each of these sections can be calculated as:

$$Q = A\,h\,(T_s - T_b) \tag{4.8}$$

where A is the heat transfer area, h is the convection coefficient resulting from the Nusselt numbers previously calculated, T_s is the lamination surface temperature, assumed constant over the section, and T_b is the coolant bulk temperature. Note that the bulk temperature is unknown, since the coolant increases its temperature as it travels along the channel. However, if the sections are small enough, the bulk temperature in a section can be approximated by the coolant temperature at the entrance of that section.

The increase in the coolant bulk temperature after one section is then obtained from:

$$\Delta T_b = \frac{Q}{\dot{m}\,c_p} \tag{4.9}$$

where $\dot{m}$ and c_p are the coolant mass flow and specific heat capacity respectively.

3. *Ideal cooling power calculation.* In order to cool the winding laminations a coolant gas is circulated between them. Ideally, the power needed to circulate this gas equals the mass flow times the total pressure drop experienced by the gas along the channel (Δp_{total}) as in equation (4.10). Since one channel is divided in a number of sections, the total pressure drop is calculated as the entrance shock pressure drop (Δp_{ent}), plus the sum of the pressure drops for each of the sections (Δp_{sec}) (see equations (4.11) to (4.13)).

$$P_{cool} = \dot{m}\,\Delta p_{total} \tag{4.10}$$

$$\Delta p_{total} = \Delta p_{ent} + \sum \Delta p_{sec} \tag{4.11}$$

$$\Delta p_{ent} = 0.5\,\frac{\rho\,v^2}{2} \tag{4.12}$$

$$\Delta p_{sec} = f_d\,\frac{L_{sec}\,\rho\,v^2}{2\,D_h} \tag{4.13}$$

where f_d is the Darcy friction factor previously calculated, ρ is the coolant gas density, v is the gas velocity, L_{sec} is the section length and D_h the hydraulic diameter.

4. *Maximum current estimation.* Finally a lumped parameter model is assembled for each lamination turn. The model is fed with the losses generated in each section of the conductor for a certain current level. These losses are calculated assuming that the current flows uniformly along each and every section as shown in Figure 4.4, which is an approximation to reality. Besides, convection is modeled for each section based on the heat transfer coefficients and coolant gas temperatures previously calculated. Figure 4.5 shows the lumped parameter model for one turn, divided in 5 sections plus the end windings. It is worth noticing that since the coolant temperature and flow conditions are similar at both sides of the lamination, convection at the upper and lower surface is lumped into a single element. In this element, the average of the convection coefficients and coolant temperatures in the upper and lower side of the conductor are used.
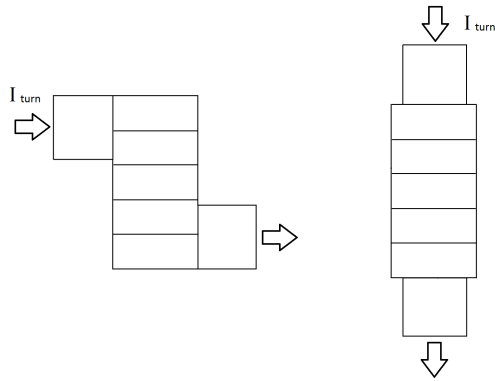
Figure 4.4: Simplification of the wave winding turn in the theoretical model.
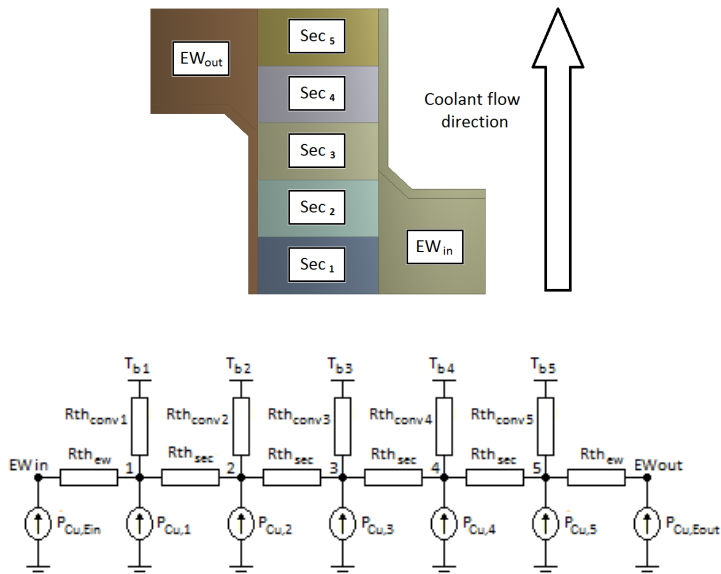

Figure 4.5: Lumped parameter model of a single turn.

Once the models for all turns are ready, an iterative process is carried out to find the maximum current that can be fed to the machine without exceeding the maximum temperature limit at any point. With this current loading, the temperatures in the different sections of the conductor are calculated and compared to the ones assumed in the first step, in order to determine whether to carry out another iteration step.

The model is used to investigate the influence of the slot fill factor and the coolant flow in the load capabilities of the machine. A high fill factor is one of the most significant advantages of the laminated winding concept. On one hand, having a higher fill factor impacts the conductor losses positively. A larger conductor cross sectional area results in lower resistance, and therefore reduced losses for the same current loading. On the other hand, increasing the fill factor leaves less distance in between turns for the coolant circulation.

Figure 4.6 shows how the convection coefficient at the conductor surface and the current density of the winding result, for different slot fill factor and coolant flow values. Looking at the right plot in Figure 4.6 it appears that the winding current density increases both with the coolant flow and with the slot fill factor. It is clear that for a constant geometry the cooling effect is improved for increased coolant flow. However, the influence of the fill factor in the cooling for a constant coolant flow is even more significant. As mentioned before, an increased fill factor leaves less space for the coolant circulation between turns. If the coolant flow is kept constant, a reduced cross sectional area of the cooling channels implies that the fluid moves with higher velocity, thus improving the cooling effect. The counterpart is a rise in the pressure drop over the cooling channel, which affects the design of the rest of the cooling circuit. It is not within the scope of this work to analyze the cooling circuit beyond the electrical machine; nevertheless, care is taken so that the pressure drop over the cooling channel is kept at reasonable levels. Figure 4.6 also presents the temperature distribution for each turn obtained from the theoretical model for $K_f = 0.8$ when $2000\,l/min$ of air flow per phase segment are applied. Turn number 1 is the innermost turn (the closest to the airgap). The cooling air flows upwards in the turns depicted. It is worth noticing that the hotspot temperature is kept to 180 °C.

From the results presented in Figure 4.6 it is clear that the design with the highest fill factor performs best. There are however some practical limits to the parameters analyzed. From the winding prototypes already manufactured and the experiments conducted on those, a distance smaller than $0.3\,mm$ between turns is difficult to realize (corresponding to a slot fill factor $K_f = 0.8$). Besides, an air flow in the range of $1500 - 2000\,l/min$ per phase segment seems reasonable to achieve with the appropriate fan.
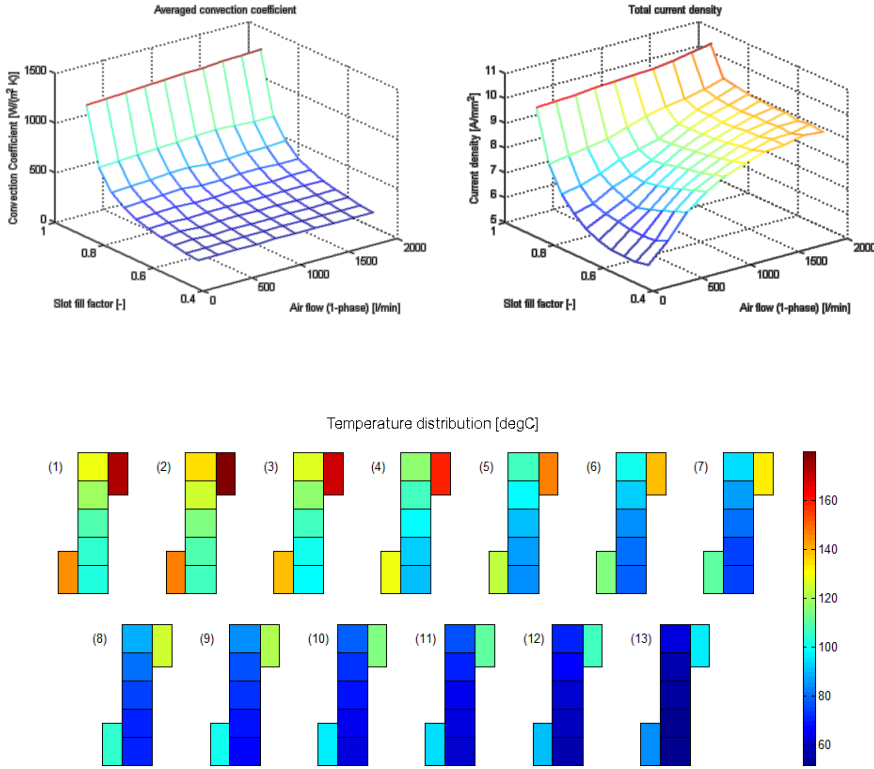
Figure 4.6: Theoretical model results. The top plots represent the averaged convection coefficient (left) and the current density (right) as a function of the slot fill factor and the coolant flow. The lower plots show the resultant temperature distribution for $K_f = 0.8$ and $2000\,l/min$ of air flow per phase.

Since the proposed winding configuration, with three axially distributed phase segments and without magnetic flux collectors at the tip of the teeth, is expected to link less magnetic flux from the rotor permanent magnets than the conventional distributed winding configuration presented in the previous chapters, the number of turns is initially increased to 13 turns instead of 9. This figure can be later revised based on the results from the electromagnetic simulations. The slotting factor K_s and the yoke depth factor K_y remain unchanged from the values obtained in Chapter 3, $K_s = 0.36$ and $K_y = 0.40$. The physical dimensions of the stator are also the same.

Table 4.1 compiles the main geometry parameters. Rotor parameters are presented as well for clarity, although they are not changed.

Table 4.1: Laminated winding stator characterization.

Param.	Value	Description
D_{so}	214.0	(mm) Stator outer diameter
D_{si}	139.7	(mm) Stator inner diameter
D_{ro}	138.5	(mm) Rotor outer diameter
D_{ri}	30.0	(mm) Rotor inner diameter
g	0.6	(mm) Airgap length
L_{seg}	46.6	(mm) Phase segment length
L_{tot}	160.0	(mm) Total machine length
N_p	8	(-) Number of poles
K_y	0.40	(-) Stator yoke depth factor
K_s	0.36	(-) Stator slotting factor
K_{th}	0.70	(-) Stator tooth length factor
N_q	8	(-) Number of slots
K_1	0.87	(-) Ratio of the angular span covered by magnets
K_3	0.57	(-) Radial rotor proportion occupied by magnets
d_r	0.9	(mm) Half of the distance between adjacent magnets
d_1	1.3	(mm) Distance between the outer air pocket edge and the rotor end

4.4.2   3D Finite Element model

A 3D FE model of the stator design selected from the previous analysis is made with a double purpose:

(a) take into account certain aspects of the real machine that were not incorporated in the lumped parameter model, such as the non-uniform loss distribution in the winding, the conductive paths for the heat provided by the winding rubber supports and the stator teeth and yoke and the possible natural convection cooling of the outer case surface.

(b) verify that the maximum temperature limit is not exceeded anywhere in the complete stator.

First, a FE model of the winding turns is simulated electromagnetically in Ansys-Maxwell for the current value obtained from the theoretical model, in order to obtain the distribution of ohmic losses in the conductors. Then, these losses are fed to a thermal FE model of the whole stator geometry, together with the convection coefficients and the coolant temperatures calculated from the empirical correlations. Figure 4.7 illustrates this process.

Electromagnetic FEA
Losses distribution

$$Nu = f(Re, Pr, D_h)$$
$$h = \frac{Nu\,\lambda}{D_h}$$
$$Q = A\,h\,(T_s - T_b)$$
$$\Delta T_b = \frac{Q}{\dot{m}\,c_p}$$

Analytical - Empirical Model
Convection coef. + Coolant temp.

Thermal FEA
Temperature distribution
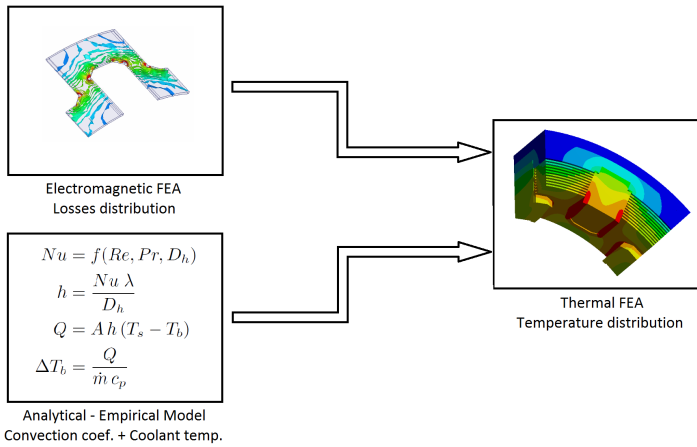
Figure 4.7: 3D thermal analysis process.

As well as for the lumped parameter model, the axial length of a phase segment is divided into sections (see Figure 4.5). Five sections of equal size are considered in this case. Convection happens only at these sections' surface, previously defined as cooling channels, and not over the end windings. The

convection coefficient is assumed constant over each section, so is the coolant bulk temperature. With these assumptions, the heat generated in the end windings needs to travel along by conduction to the cooling channel, where it can be dissipated by convection.

The next figures show the current density vectors and the ohmic loss distribution resulting from the electromagnetic FE simulation of the winding conductors, as well as the temperature distribution in the stator when $2000\,l/min$ of air flow per phase segment are applied in different cases: considering only the laminated winding conductors (as in the theoretical study in the previous section); the winding conductors plus the rubber supports which provide a radial path for heat conduction in between the turns; adding the stator teeth to the previous case; and finally considering the full stator assembly. In every case, a current of $356.4\,A$ is fed to the winding turns corresponding to a current density in the slot of $8.96\,A/mm^2$, as calculated from the lumped parameter model for a hotspot temperature of $180\,℃$.
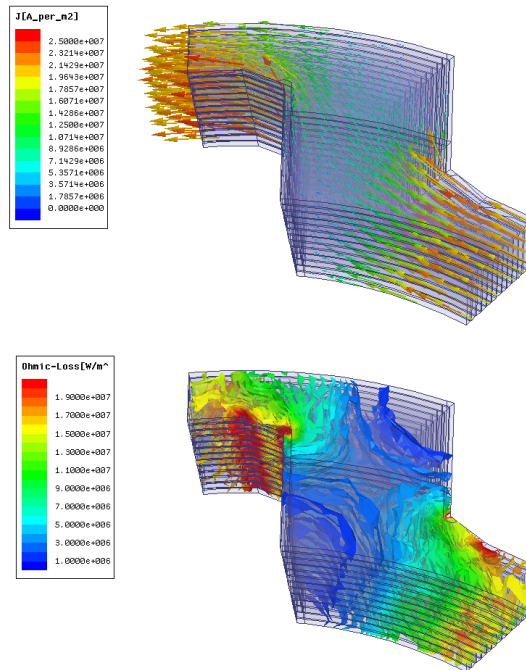
Figure 4.8: Electromagnetic FE simulation results. Current density vector and ohmic loss distribution in the winding conductors.
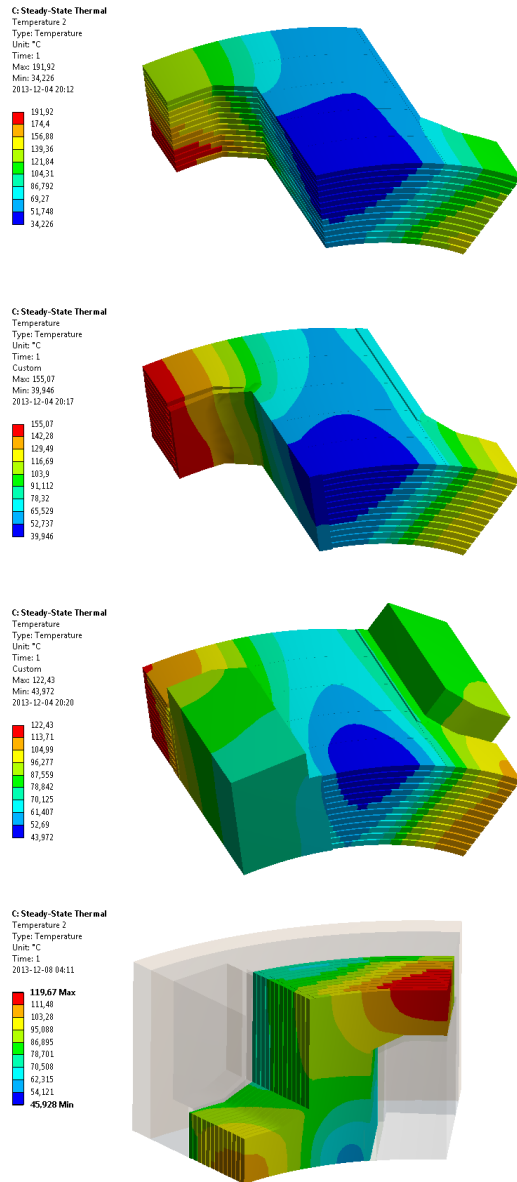
Figure 4.9: Thermal FE simulation results. From top to bottom: only winding conductors; winding conductors and rubber supports; conductors, supports and stator teeth; and full stator assembly.

Some conclusions are drawn from the FE simulation results. The temperature distribution from the uppermost plot can be compared to the analytical-empirical model results from the previous section (see Figure 4.6). Despite the simplifications made, the maximum temperature obtained from the FE simulation corresponds fairly well with the one considered in the Matlab model: 192 ℃ vs. 180 ℃. In both models, the warmest point is the end winding of the second innermost turn on the coolant output side, and the temperature decreases when moving radially, towards the outer turns.

Comparing the first and second plots starting from above in Figure 4.9, it is seen that by adding the rubber supports, the maximum temperature is decreased by more than 35 ℃ while the minimum temperature increases by nearly 6 ℃. This is a very interesting result, since it reveals the importance of choosing as good a heat conductor material as possible for the winding rubber supports. The better the conductivity of the support material is, the more evenly spread the heat is among the turns, which allows for higher conductor losses, i.e. higher current before the limit temperature is reached somewhere in the winding. Improving these conduction paths by adding the stator teeth, whose heat conductivity is over ten times higher than that of the rubber supports, further reduces the maximum temperature in the stator by another 32 ℃, as seen in the third plot.

Besides the direct forced convection of the winding conductors, there is also natural convection taking place on the outer surface of the machine housing. Although this natural convection cooling is not significant when full cooling power is applied to the winding conductors, it becomes the only cooling mechanism in case of failure of the winding coolant supply. Therefore, it is important to investigate the thermal performance of the machine taking the natural convection cooling of the outer case into account, both with and without direct cooling of the winding conductors.

If both direct convection cooling of the winding conductors (with $2000\,l/min$ of air) and natural convection over the outer case are taken into account, $514\,A$ can be fed into each turn without exceeding 180 ℃ at any point, as shown in Figure 4.10. This current value corresponds to a current density of $12.91\,A/mm^2$ with respect to the slot cross sectional area (this figure is significantly higher at the end windings). On the other hand, if no direct cooling at all is applied, and the machine is cooled only by natural convection over the outer case, the current is limited to $69.3\,A$ per turn; correspondingly $1.74\,A/mm^2$. The temperature distribution in this case is presented in Figure 4.11. It is interesting to notice how temperature span in the stator is remarkably reduced when compared to the previous case: 3 ℃ instead of 123 ℃. If only natural convection at the

outer case is consider, the heat generated in the windings must travel all the way to the outer case, heating up all the machine more evenly.
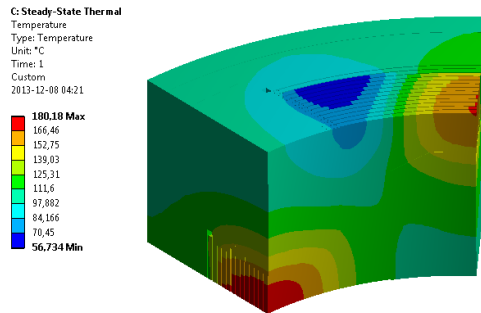

Figure 4.10: Stator temperature distribution for $514\,A$, direct winding cooling ($2000\,l/min$ of air) and natural convection at the outer case ($h = 12\,W/(m^2K)$).
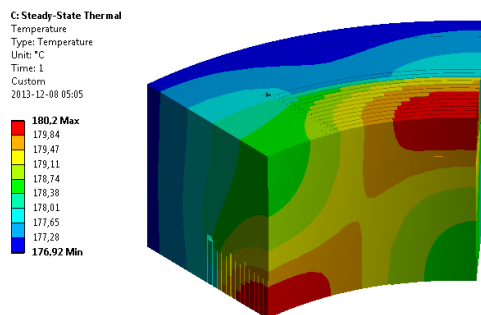

Figure 4.11: Stator temperature distribution for $69.3\,A$ and natural convection at the outer case ($h = 12\,W/(m^2K)$).

The current calculated for the last case, in which only convection cooling of the outer case is considered seems low when compared to other machine designs of the same size. For example, the machine presented in Chapter 2 which is also cooled only by natural convection over the outer case features a nominal current density of $6.5\,A/mm^2$. However, in this case the winding laminated turns are just surrounded by still air, which is not a good heat conductor, and all the heat generated in the winding has to travel to the stator teeth and further to the yoke and the outer case through the fairly low conductivity rubber material of the winding supports. One difficult aspect in the thermal

modeling of electrical machines is the interface between two solid parts, as it is discussed in Section 2.8.1. In the laminated winding stator, there are contact interfaces between the winding turns and the rubber supports, between these and the stator teeth, between the stator teeth and the stator yoke and also between the yoke and the outer case. Since the focus in this section is on the direct cooling of the winding, all these contact interfaces are modelled as ideal, i.e. assuming perfect contact between the two solid parts. Although these interfaces do not have a significant influence when full cooling power is applied to the winding turns, since most of the heat is already dissipated there, they become more relevant as more heat is dissipated through the outer case.

A natural thought is to consider that, if the machine is not sealed, there is some sort of air movement inside it due to the differences in density created by the temperature gradients. Hence it seems appropriate to investigate the effect of natural convection at the winding turns. In order to calculate the corresponding heat transfer coefficients, the winding turns are approximated by horizontal hot plates, which is a bit less favorable from a cooling perspective than vertical hot plates, and therefore yields conservative results. Nevertheless, it should be noticed that this is a fairly rough approximation. In reality, when the two winding turns are close to each other, they behave more like a channel than single plates. The air velocity field then will be different and that has a direct effect on the convection. Besides, the turns are not straight plates but more like cylinders, and depending on how the machine is installed, the curvature of the cylinder may help the air movement. A more accurate estimation of the convection coefficients due to natural convection at the winding turns will require either experimental measurements or detailed CFD simulations.

The correlations used are (4.15) and (4.16) for the convection coefficient of the top surface of a hot plate and (4.17) for the bottom one. [62]

$$Ra_L = g\,\beta\,(T_s - T_{amb})\,D^3/(\nu\,\alpha) = Gr_L\,Pr \tag{4.14}$$

$$Nu = 0,54\,Ra_L^{1/4} \qquad \text{for } 10^4 \leq Ra_L \leq 10^7 \tag{4.15}$$

$$Nu = 0,15\,Ra_L^{1/3} \qquad \text{for } 10^7 \leq Ra_L \leq 10^{11} \tag{4.16}$$

$$Nu = 0,27\,Ra_L^{1/4} \qquad \text{for } 10^4 \leq Ra_L \leq 10^{10} \tag{4.17}$$

where Ra_L is the Rayleigh number, Gr_L is the Grashof number, g is the gravity acceleration, β is the thermal expansion coefficient, α is the thermal

diffusivity, ν is the kinematic viscosity, T_s is the hot surface temperature and T_{amb} is the ambient temperature.

The convection coefficient values obtained from the correlations are very similar for all turns, and their mean value is $h_{top} = 8.29\,W/(m^2K)$ and $h_{bottom} = 1.35\,W/(m^2K)$. In order to simplify the 3D FE model, the average of these two values, $h_{nc} = 4.82\,W/(m^2K)$ is applied to all winding conductor surfaces, regardless of their position and orientation. The resulting temperature distributions for a winding current of $69.3\,A$ per turn $(1.74\,A/mm^2$ in the slot) and $129.5\,A$ per turn $(3.25\,A/mm^2)$ are presented in Figure 4.12.
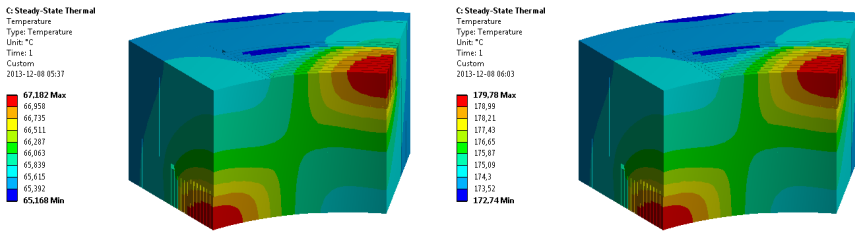
Figure 4.12: Stator temperature distribution for $69.3\,A$ (left) and $129.5\,A$ (right) with natural convection cooling both at the outer case ($h = 12\,W/(m^2K)$) and at the winding conductors ($h = 4.82\,W/(m^2K)$).

Table 4.2: 3D FE thermal simulation results summary.

	Radial conduction	Direct winding cooling	Natural winding cooling	Natural convection on case	Current density (A/mm^2)
1	✗	✔	✔	✗	8.95
2	✔	✔	✔	✗	12.88
3	✔	✔	✔	✔	12.91
4	✔	✗	✗	✔	1.74
5	✔	✗	✔	✔	3.25

Table 4.2 summarizes the results of the different simulation cases described above. In it, the current density (in A/mm^2) that gives a hotspot temperature of 180 ℃ is presented. The different simulation cases take into account different heat transfer mechanisms, which are:

- Radial heat conduction between the winding turns, through the winding rubber supports and the stator teeth

- Direct winding forced convection cooling, with an air flow of $2000\,l/min$ per phase segment

- Natural convection cooling of the winding turns

- Natural convection over the outer case of the machine

4.5 Electromagnetic Characterization

At this stage, a 3D FE model is developed in Ansys-Maxwell in order to assess the electromagnetic performance of the proposed laminated winding machine. To keep the model as light as possible, hence minimizing the computation time, just one pole is modeled (corresponding to one eight of the total machine) for only one phase segment. If several simulations are run for different current loading and different rotor positions relative to the stator, the 3-phase magnitudes can be subsequently synthesized from the single phase results as shown in [79]. Antiperiodic boundary conditions of the form $H(r, \tau, z) = H(r, \tau + \pi/4, L_{seg} - z)$ in cylindrical coordinates are applied to the sides of the rotor and stator sectors, as well as the free airgap boundary. Ansys-Maxwell does not allow to assign master-slave boundary condition in cylindrical surfaces, therefore the airgap is segmented in intervals of $\pi/48$ radians.
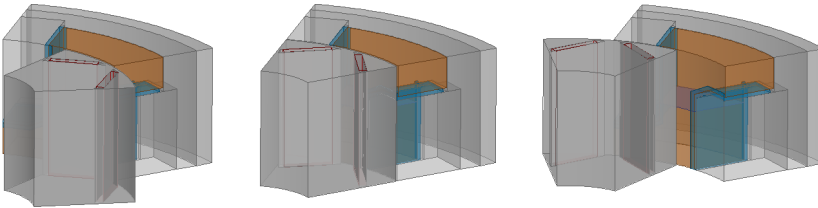

Figure 4.13: 3D FE model of one eighth of a laminated winding machine phase segment for different rotor positions.

Since the goal is to evaluate the torque production and flux linkage capabilities of the machine, only magnetostatic simulations are conducted. In such simulations, the thin laminated winding turns can be replaced by a solid

winding supplied with the total current going into the slot, i.e. the current per turn times the number of turns, thereby reducing the mesh requirements on the winding. Figures 4.14 and 4.15 show the magnetic flux density vector field distribution (B in Vs/m^2 or T), the torque and the winding flux linkage for different rotor positions at no load. The flux linkage presented is the integral of the flux density field over the stator yoke cross section represented as a line in Figure 4.13.

To evaluate the torque production capabilities of the laminated winding machine, the most advantageous position (excluding reluctance torque) for a single phase segment is analyzed. This position corresponds to a 90 electrical degrees phase shift between the rotor poles and the stator poles (the stator teeth). Figure 4.14 shows the torque produced on the simulated rotor sector, i.e. one eighth of the total torque on the rotor for one phase segment (solid blue) and the corresponding flux linkage (dashed green) for different current loadings. It is worth noticing that torque produced by the 3-phase winding is not three times that of one phase segment, since the relative position of the rotor to the different phase segments differs in 120 electrical degrees in each case.
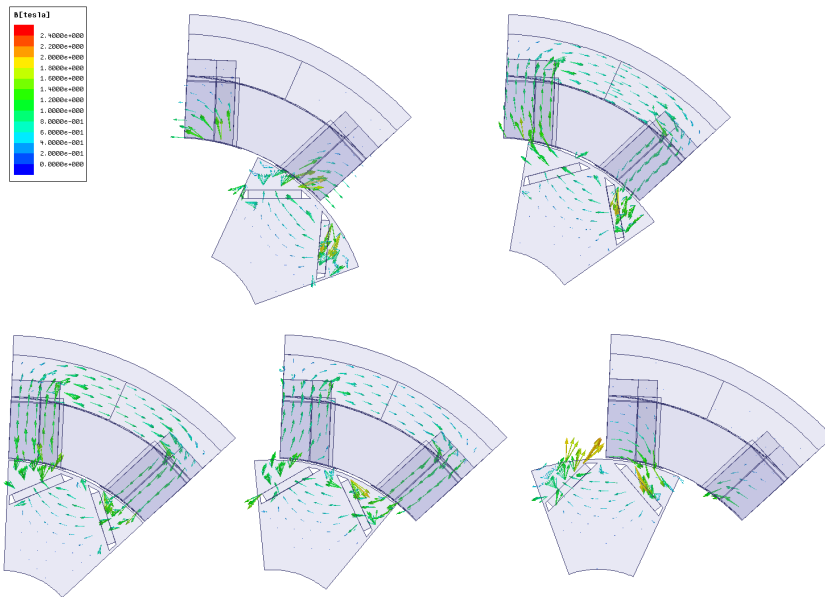

Figure 4.14: Flux density distribution from the 3D FE simulation of one phase segment at no load.
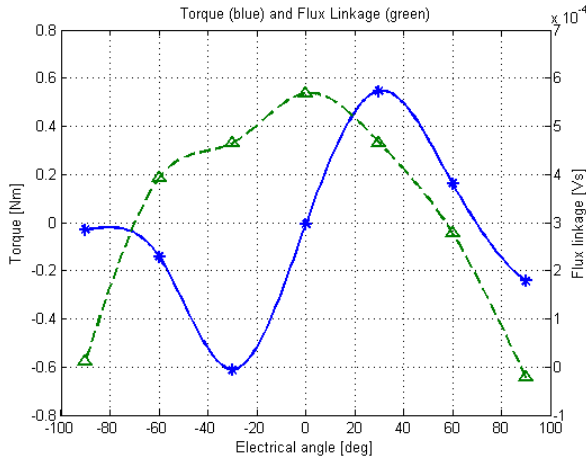
Figure 4.15: Torque (solid blue) and flux linkage (dashed green) results from the 3D FE simulation of one eighth of a phase segment at no load.
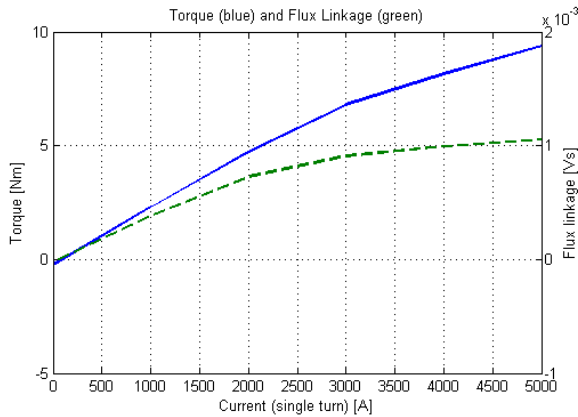

Figure 4.16: Torque (solid blue) and flux linkage (dashed green) results from the 3D FE simulation of one eighth of a phase segment (max. torque position).

When looking at Figure 4.16, particularly at the flux linkage curve, it can be observed that magnetic saturation effects start to be noticeable for a current of $2000\,A$ (single turn), which corresponds to a current density of $3.9\,A/mm^2$. As it is discussed in Chapter 3, this magnetic saturation effect reduces the torque production capabilities of the machine when the current is increased. Since from the thermal point of view, this geometry withstands much higher current

density loading, it follows that this stator configuration is not the optimal one.

In order to asses the output torque level, simulations for different current and different rotor positions are needed. The torque produced by the 3-phases can be synthesized from the results of these simulations, as shown in Figure 4.17 for the no-load torque. Due to schedule constraints, a more comprehensive batch of simulations cannot be conducted at this stage. However, it seems reasonable to evaluate first the impact of the magnetic saturation effects with the help of a significantly shorter simulation batch, as previously shown.
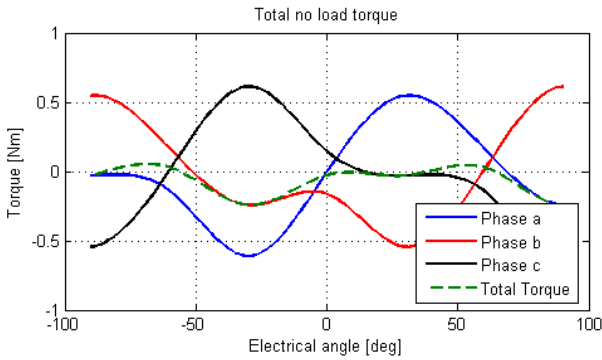
Figure 4.17: No load torque synthesized from the 3D FE simulation of one phase segment.

4.6   Reflections on the laminated winding machine geometry

The discussion in Section 4.4 shows the potential of the laminated winding configuration to withstand remarkably high currents for unlimited time without overheating. This is, of course, a very desirable feature for an electrical machine, especially for traction applications, for all the reasons already exposed in this thesis. However, when analyzing the electromagnetic capabilities of the machine, i.e. its ability to convert between electric and mechanical energy, some issues come up.

First, the geometry proposed in Section 4.2 aims for the easiest and fastest manufacturing and assembly processes possible. For this reason, the stator teeth and yoke are extruded profiles, so they can be easily manufactured from laminated steel. Unfortunately, this simple tooth geometry does not

link as much magnetic flux from the rotor as it could, since there is no field concentration effect, due to the lack of flux collectors (tooth tips) covering neither the active part of the turn (extending the teeth circumferentially) nor the end winding parts (extending the teeth axially) as seen in Figure 4.2.

Besides, to make the best out of the machine, it has to be designed to match the highest efficiency point to the most frequent operation point. The challenge is the same as in Chapter 3: reach a balance between the cross sectional area of the slots and the area left for the magnetic flux to circulate, so the copper losses remain low and the effects of magnetic saturations are limited.

If a simple geometry like the one presented is to be used, and the complete machine is obtained by stacking three phase segments together with an angular shift of 120 electrical degrees, each of these segments contributes with a certain end winding length, where the flux from the rotor is not linked to the windings, and therefore does not contribute to the torque production. Although an exact value of how much of the total length of a phase segment is actually not active is not calculated here, it seems clear that this machine configuration becomes more suitable the longer the machine is.

Finally, the computational cost in terms of time and memory for running this type of 3D magnetostatic simulations increases enormously as the adaptive meshing algorithm results in a vast number of elements when materials become saturated. As an example, the number of tetrahedra needed for the different current loadings presented in Figure 4.16 is presented. The simulations are conducted in Ansys-Maxwell 16 under Windows 7 64-bit, in an AMD FX™4170 Quad-Core processor @ $4.20\,GHz$ and $16\,Gb$ installed memory (RAM).
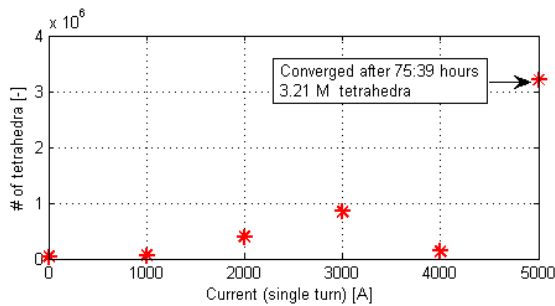

Figure 4.18: Number of tetrahedra needed in the calculations for Figure 4.16.

Chapter 5

Conclusions and future work

5.1 Conclusions

In this thesis, the design process of an electric traction machine for a HEV application is presented, describing its evolution in detail as the technical requirements posed by the customer change. The highly dynamic load profiles together with the tight requirements on torque and power density, weight, efficiency and cost make the design process of such a machine to be in many ways different from that of a machine for a conventional industrial application. Therefore, a new design methodology is proposed based upon driving cycles, which try to match the real traction application.

The traction machine designer usually faces a compromise between the nominal power rating of the machine and its overloading capabilities. A machine that is optimized to operate at its nominal power rating makes the best use of the materials in the magnetic circuit already at this point, and saturation effects come up easily, even at very light overloading. On the other hand, a machine designed to operate linearly deep into the overloading region suffers from a lower efficiency at nominal power. The new design methodology aims to find not only the nominal power rating but also the peak-to-average power ratio that gives the lowest fuel consumption for a given driving cycle.

For the same driving cycle, both the nominal power rating and the peak-to-average power ratio largely depend on the application considered. In a pure EV the electric traction machine is the only source of tractive force, hence it has

to cover the full torque and power range required over that particular driving cycle. However, in a HEV the electrical machine and the ICE work together to deliver the required tractive power. Depending on the control algorithm implemented in the vehicle, the power demand at any time is covered either by the ICE, the electrical machine or both. In this way, the electrical machine does not need to cover the whole range needed over the driving cycle, and it can be designed to match the highest efficiency region with the most frequent operation points.

The design experiences presented reveal the importance of the thermal aspects of the machine on its final performance. While the overloading capabilities of a machine for a short time are usually limited by magnetic saturation effects, the nominal power rating is directly related with the machine's ability to dissipate the heat losses generated. Both FE models and lumped parameter models are used to assess the thermal behavior of the new designs, although 3D effects must be taken into account if 2D FE models are used for the results to be applicable. Bringing the heat sink closer to the losses source has proven a good way to increase the thermal performance of an electrical machine.

The laminated winding configuration appears as a very promising alternative, allowing for significantly higher current loading. It offers a great cooling potential since the losses are dissipated directly at the winding conductors, where they are generated. However, the whole machine geometry needs to be redesigned to allow for the higher magnetic flux resulting from the increased current.

5.2   Future Work

As mentioned in Section 2.5, a rotor prototype featuring oil spraying over the end windings for cooling is manufactured and tested. However, due to limited time and resources at the moment, the set of measurements conducted is incomplete and no reliable results are obtained. In order to increase the level of understanding of the effects and potential of oil spraying over the end windings, it is proposed to extend the measurement set with new experiments, in order to find a suitable way of modeling the oil spraying phenomena. Subsequently, the lumped parameter thermal model presented in Chapter 2 can be upgraded, including the effect of oil spraying.

On a different matter, when analyzing the laminated winding alternative

the computational cost of the 3D FE simulations needed is remarkably larger than that of the 2D models for traditional laminated machines; increasing drastically when the materials become magnetically saturated. This makes the design process slow, and sometimes even impossible, if the computing resources are not sufficient. As a continuation to the work presented here, it is proposed to further develop the electromagnetic design process of the laminated winding geometry, minimizing the number of 3D FE simulations needed. A good approach is to create an equivalent 2D FE model and tune it with a minimum set of 3D FE simulations in order to cut down the computation requirements. Then, most of the design work can be done in the equivalent 2D model, and the resulting geometry is finally validated in 3D.

5.3 Electric traction machine design guidelines

5.3.1 Technical specifications

The success in the design of an electric traction machine largely depends on having a comprehensive set of technical specifications from the beginning. Some of this specifications just concern the electrical machine itself, while some other may refer to the traction system, or even the whole vehicle. Communication between the electrical machine designer and the final customer (usually the car manufacturer or one of their sub-suppliers) is not always straight forward, since each belong to a different technical area. This is something that sometimes is overlooked and may yield to misunderstanding of the specifications, and thus to unsuitable design solutions.

Some technical specifications of interest for the electric traction machine design process are listed below:

- *Powertrain concept.* It helps the designer to know and understand the whole powertrain concept. The fact that the electrical machine drives only one wheel, or both wheels on one axle; its location within the vehicle; the purpose of the vehicle, etc. have several implications in the final design that are worth taking into account.

- *Physical size constrains.* The total available physical space for the unit. It is usually limited by the rest of the vehicle components' layout. For the designer, it is important to know what should fit inside that volume: electrical machine, connectors, sensors, integrated electronics, etc.

- *Load profile.* This is perhaps one of the most critical specifications for traction applications. Driving cycles seem to be the best way to specify the load profile, however it is not an easy task to find a driving cycle

that reflects both the customers' expectations and the more realistic everyday driving conditions. Besides driving cycles, there may be a number of extreme design cases that the vehicle should keep up with, such as maximum speed, standstill torque, etc. These could be specified separately, in terms of their implications for the electrical machine.

- *Mechanical environment and interfaces.* Certain aspects of the design are influenced by the mechanical environment in which the electrical machine is going to operate; machines operating under large vibrations should have a larger airgap length for example. The layout of the traction system also influences the design. If there is a gearbox, the gear ratio to the wheels is an important parameter in the electrical machine design. In some complex configurations, a hollow rotor shaft may be needed, affecting the whole rotor geometry. In addition, available fixing points and shaft couplings may be of interest.

- *Thermal environment and interfaces.* As it is discussed in this thesis, a good thermal management is essential for a successful electric traction machine design. Therefore it is important to know the thermal environment in the electrical machine surroundings: ambient temperature (if the ICE or the exhaust system are close, the temperature of the surrounding air can be significantly increased); availability of cooling media (water circuit, compressed air, fans, etc); possible heat conduction paths to large masses such as the vehicle chassis, etc.

- *Vehicle characteristics.* In order to model the whole vehicle behavior over a driving cycle some vehicle details are needed. The vehicle mass, drag coefficient, wheel radius, ICE characteristics, as well as the control strategy (most importantly the ICE - Electrical machine power split algorithm) contribute to more accurate and relevant simulations, which have an impact on the final machine design.

It is also important no to take all these specifications as fixed and invariable, but to identify the different specifications according to their possibility to be modified. Along the design process, the designer may realize that the solution is particularly sensitive to one or more of the constrains, and the design could be improved substantially if those constrains are relaxed.

5.3.2   Driving cycle simulations

In order to evaluate which electrical machine characteristics, mostly nominal power rating and overloading capabilities, are best from a fuel efficiency point of view, a dynamic model of the whole vehicle such as the one presented in Appendix C is simulated over different driving cycles. Also, different electrical

machines are simulated for each driving cycle, analyzing their effect on the vehicle fuel consumption.

At this stage, it is important to know as many details about the powertrain as possible, in order to obtain accurate results. The results obtained for the different driving cycle simulations can be combined, in order to find the electrical machine that minimizes the overall fuel consumption. Besides, the simulation model allows to try different system configuration, control strategies or even particular electrical machine topologies and asses their effect on the fuel consumption in a relatively easy and fast way.

5.3.3   Electrical machine design

From the driving cycle simulations, a certain nominal power rating and a peak-to-average power ratio is selected. The task now is to find an electrical machine geometry that fulfills these requirements with high energy efficiency. The first step is to select the machine technology(ies) that seems more promising for the application under study. This can be done with the help of a selection matrix, such as the one proposed in Figure 2.4, in which each technology is graded between 0 (poor) and 5 (excellent) for different features, and each feature is given a weight depending on its relevance for the application.

Once a certain technology is selected, a first batch of simulations determines the basic machine parameters: number of poles and rotor/stator radius ratio. Already at this stage thermal simulations are very important, since they determine the nominal power rating of the machine. However, the electromagnetic simulations at this stage do not need to be very detailed. A few simulations for the nominal current value and several rotor positions are enough to evaluate the machine performance and compare the different alternatives.

A second set of simulations is proposed, using the geometry resulting from the previous one as starting point, in order to refine the different geometry aspects, and optimize the machine for the desired application, matching the requirements from the driving cycle simulations.
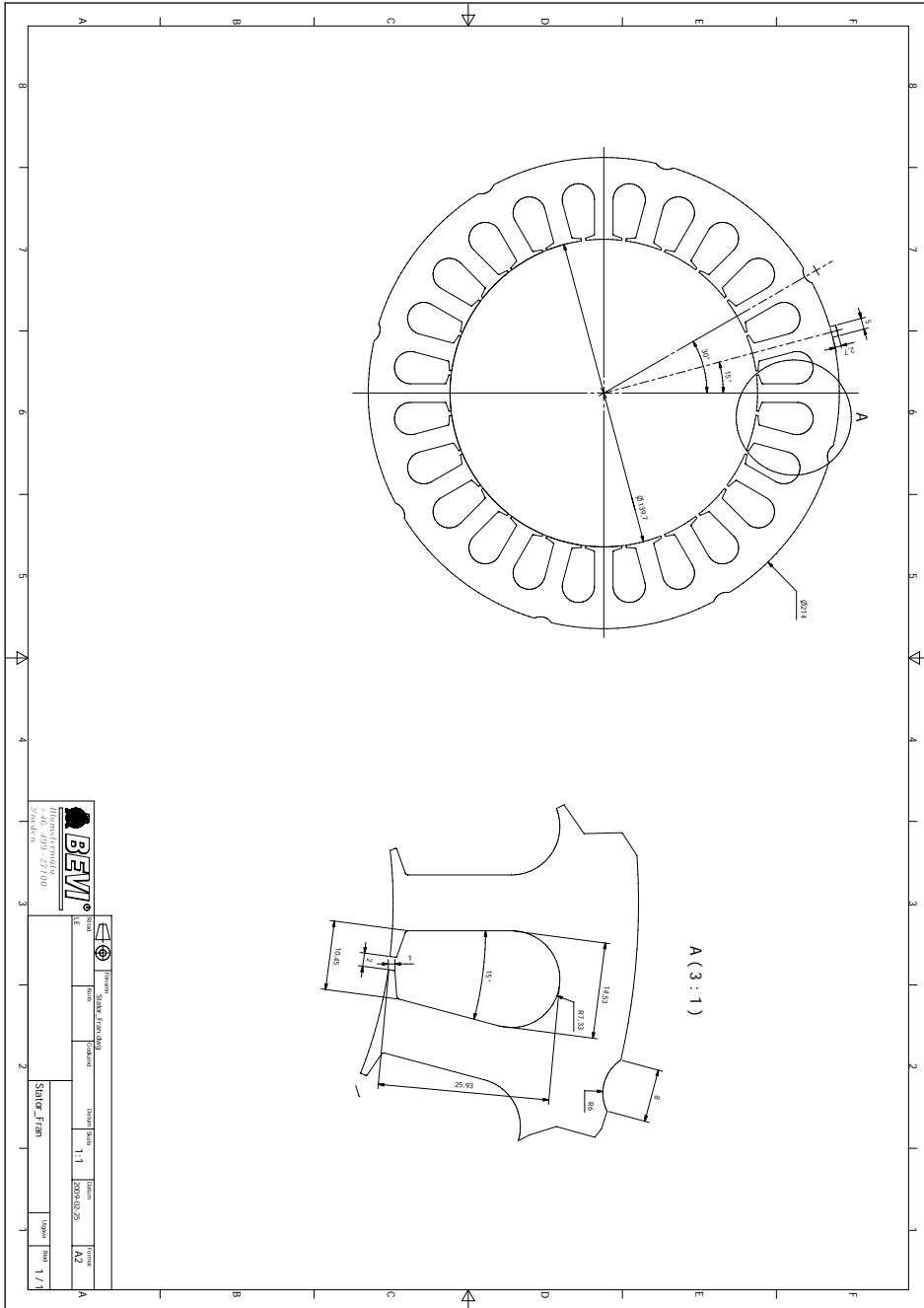
As presented in Chapters 2 to 4, different methods are available both for thermal and electromagnetic simulations, and their suitability depends on the machine analyzed. As a general rule, analytic models (such as lumped parameter models) require much less computation resources, providing results in significantly less time. However, they are not easy to tune if no experimental measurements are available, and sometimes they imply rather large simplifi-
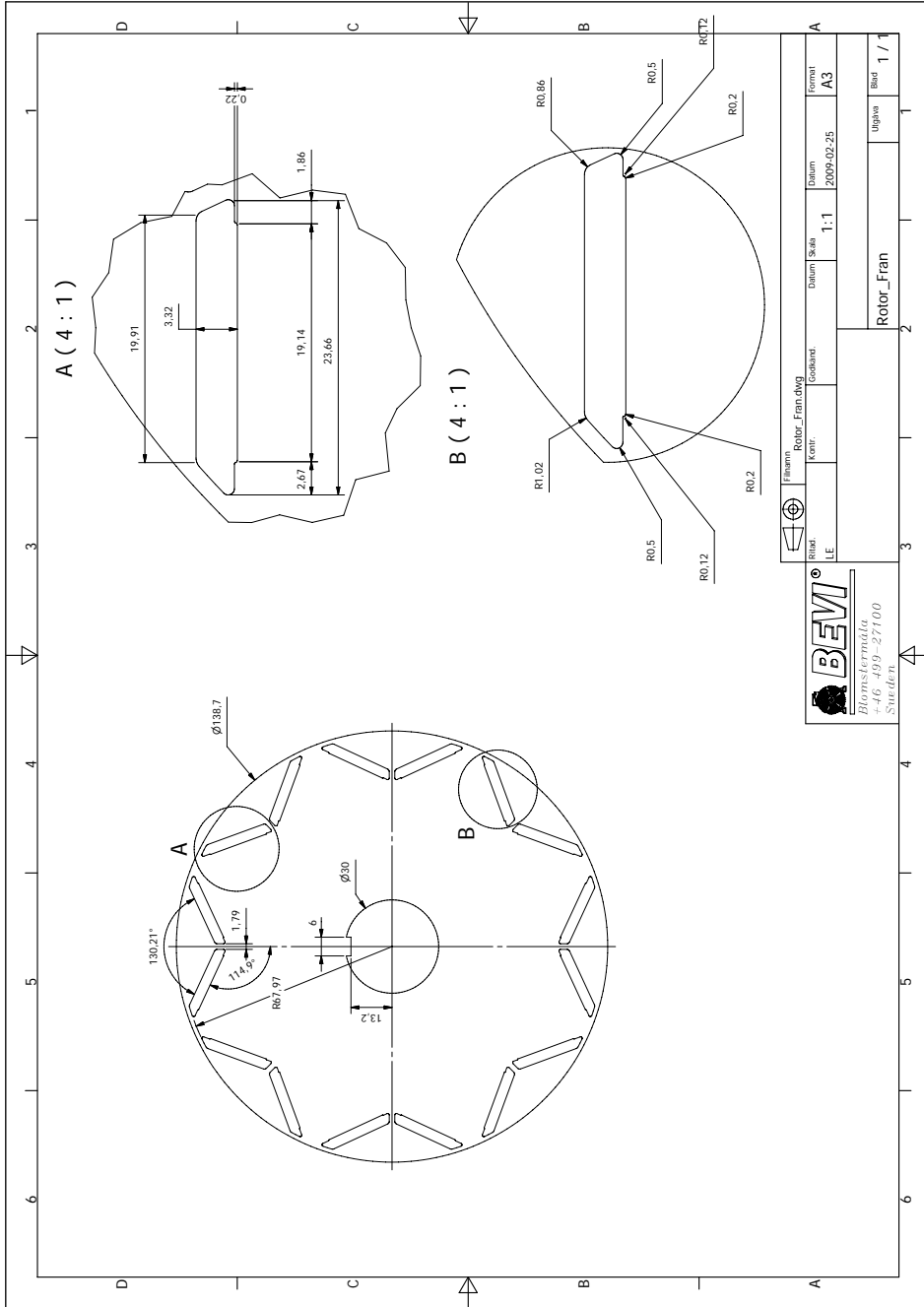
cations that may lead to misleading results. Finite Element models on the contrary are a more accurate representation of reality, but the computational cost increases remarkably when compared to the analytical models, being understandably higher for 3D FE models than for 2D FE models.

Appendix A

E-RWD traction motor drawings

The detailed stator and rotor geometry drawings corresponding to the manufactured machine prototype described in Chapter 2 are presented in the following pages. These drawings, together with the corresponding CAD files, were provided to the laser cutter for the manufacturing of the lamination packs.

A (3 : 1)

A (4 : 1)

B (4 : 1)

0,22

1,86

3,32

19,91

19,14

23,66

2,67

R0,86

R0,5

R0,2

R0,12

R1,02

R0,2

R0,5

R0,72

Ø138,7

Ø30

130,21°

114,9°

1,79

R67,97

6

13,2

A

B

Filnamn: Rotor_Fran.dwg

Ritad. LE

Kontr.

Godkänd.

Datum

Datum

Datum 2009-02-25

Skala 1:1

Format A3

Blad 1 / 1

Utgåva

Rotor_Fran

BEVI®

Blomstermåla
+46 499-27100
Sweden

Appendix B

2D Radial-flux machine design environment

The design processes presented in Chapters 2 and 3 are supported by a software tool originated at the Department of Industrial Electrical Engineering and Automation in Lund University. The development of this software is one of the contributions of the present work. This Appendix presents the details of the design tool, which helps to understand the outcome of the machine design processes mentioned above.

The aim is to provide a fast and easy-to-use CAD/CAE design tool, suitable for educational and research purposes, that simplifies the design process by relieving the designer of the tedious repetitive work, so he or she can focus on the creative and intellectual tasks: to analyze the influence of the different parameters in the machine characteristics and decide the best way to proceed in order to reach the design goal.

The design environment is based on Matlab, which launches a Finite Element package (Finite Element Method Magnetics, FEMM, developed by David Meker [84]) to conduct the actual simulations. The data resulting from these simulations is stored in a file, and subsequently post-processed in Matlab again in order to obtain the machine characteristics. The design roadmap is shown in Figure B.1.

First, the user needs to set the different geometric parameters (such as those listed in Tables 2.2 and 2.3 for example). Then, the type of analysis desired should be specified. It is possible to run either thermal FEA, electromagnetic

FEA or both, for one or several loading points, and for different rotor positions
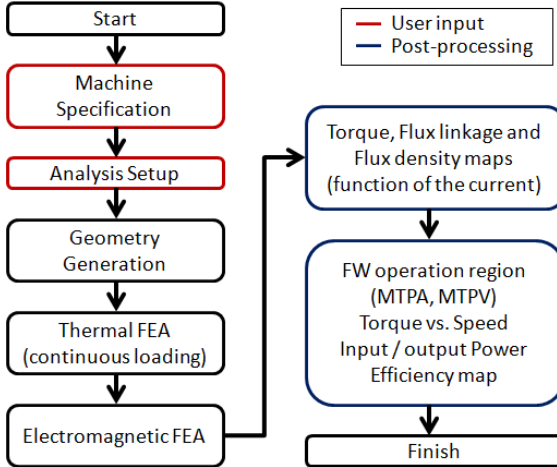relative to the stator.

Figure B.1: Design roadmap.

If the user wants to characterize a machine completely, first a number of
thermal FEA are scheduled in order to evaluate the nominal current density
loading. Then, once the nominal current density is known, magnetic FEA
are programmed for different load points (relative to the nominal value) and
different rotor positions as specified by the user. It is worth noticing that user
input is only required in the two first blocks of the roadmap in Figure B.1,
while the rest of the process is done automatically.

When both the machine and the type of analysis to perform are specified,
Matlab launches the FE package FEMM and commands it to carry out the
corresponding simulations. The results from these simulations are stored in a
text file to be processed later.

The post-processing of the simulation data is carried out entirely in Matlab.
In the most comprehensive case of a complete machine characterization, the
post processing steps are:

A. Data acquisition: The data from the FE simulation is imported from the
results file. If the simulation takes advantage of symmetry and/or periodicity

of the machine, the data is reconstructed in order to cover a full electric period.

B. *Data transformation:* The currents and flux linkages obtained from the simulations are phase values. Assuming a balanced 3-phase machine, it is possible to reduce the 3-phase AC values down to 2-phase DC values with the help of the power invariant Park transformation, which simplifies the analysis of the results. Note that the coordinate transformation is divided in two steps. First the 3-phase AC values are reduced to 2-phase AC values by means of the Clarke transformation (equation B.1). Subsequently, they are rotated with the synchronous frequency, in order to become stationary (equation B.2). The homopolar component u_0 equals zero in a 3-phase balanced system. The resulting xy system is also called the rotor coordinate system, since the x-axis is selected to be aligned with the rotor's permanent magnet flux linkage and the y-axis is just leading 90 degrees. Figure B.2 shows the graphical interpretation of the Clarke and Park transformation for a 2-pole PMSM.
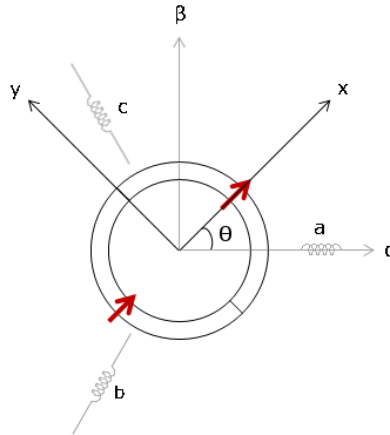
Figure B.2: Graphical interpretation of the Clarke and Park transformations.

$$
\begin{bmatrix} u_\alpha \\ u_\beta \\ u_0 \end{bmatrix} = \sqrt{\frac{2}{3}} \begin{bmatrix} 1 & \frac{-1}{2} & \frac{-1}{2} \\ 0 & \frac{\sqrt{3}}{2} & -\frac{\sqrt{3}}{2} \\ \frac{1}{\sqrt{2}} & \frac{1}{\sqrt{2}} & \frac{1}{\sqrt{2}} \end{bmatrix} \begin{bmatrix} u_a \\ u_b \\ u_c \end{bmatrix} \tag{B.1}
$$

$$\begin{bmatrix} u_x \\ u_y \\ u_0 \end{bmatrix} = \begin{bmatrix} \cos(\theta) & \sin(\theta) & 0 \\ -\sin(\theta) & \cos(\theta) & 0 \\ 0 & 0 & 1 \end{bmatrix} \begin{bmatrix} u_\alpha \\ u_\beta \\ u_0 \end{bmatrix} \qquad (B.2)$$

Once this transformation is completed, the output torque and flux linkage maps can be expressed as a function of the x and y currents.

C. Determination of the operation region: It is obvious that, in principle, the machine can be loaded with an arbitrary set of currents, provided that the inverter is able to supply them. However, for a certain output torque and speed, there is an optimal xy-current combination from an efficiency point of view. Aiming to operate the machine in the most efficient way possible, the following strategy is adopted:

1. At zero or low speeds, for a certain torque requirement the machine will be loaded with the corresponding currents on the Maximum Torque Per Ampere (MTPA) line, provided that it does not exceed the maximum current limit of neither the motor nor the inverter. This is the operation point that gives the lowest possible copper losses, which in turn are the dominating losses at low speeds.

2. As the speed increases, the back electromotive force of the machine also increases, and eventually reaches the maximum voltage level defined by the inverter dc-link voltage. From that point on, in order to increase the speed further while keeping the same output torque, the current has to move from the MTPA line following the corresponding iso-torque line towards lower flux-linkage values, until it reaches either the Maximum Torque Per Volt (MTPV) line or the maximum current limit.

3. When the MTPV line or the current limit are reached, the desired torque can no longer be delivered if the speeds further increases. The current then follows the MTPV line or the current limit circle towards lower flux linkage values, as the torque is reduced until it is not sufficient to accelerate the machine anymore. The operation region then defined by the shadowed portion of the plot in Figure B.3, where the trajectory of the xy-current vector for a certain torque requirement is illustrated.

For each point inside the operation region the torque and flux linkage maps as a function of the xy currents are known from the FE simulations; the maximum speed is calculated based on the flux linkage and the DC link voltage; copper losses and stator iron losses are computed according to equations (B.3) and (B.4) respectively, and finally, efficiency is estimated based on these calculations.
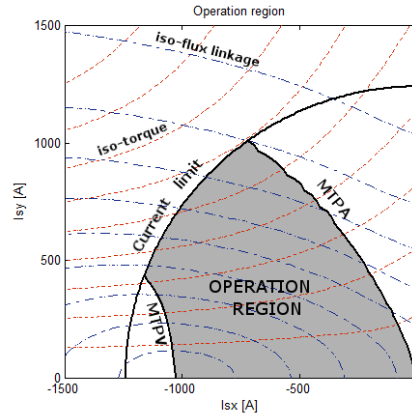
Figure B.3: Electrical machine operation region.

$$P_{cu} = R_s \, I_s^2 \tag{B.3}$$

$$P_{fe} = V_{reg} \left(C_h \, B^{E_h} \, f + C_e \, (B \, f)^2 + C_a \, (B \, f)^{1.5} \right) \tag{B.4}$$

In the previous equations, R_s is the stator resistance and it is determined based on the winding characteristics and the physical properties of the copper wires; I_s is the magnitude of the stator xy-current vector; B is the magnetic flux density; f is the electrical frequency; V_{reg} is the volume in which the iron losses are computed and it can refer to the stator yoke or the stator teeth, and C_h, C_e, C_a and E_h are coefficients depending on the material properties of the stator laminations. The values of the coefficients for the M250-35 steel used in the laminations are given in Table B.1.

Table B.1: Steinmetz coefficients for steel M250-35.

Coefficient	Value
C_h	167.219
C_e	0.3387
C_a	0.1464
E_h	1.7404

D. Presentation of the results: Finally, the main machine characteristics are presented in a graphical way, so that it is easy for the designer to assess its

suitability for a given application. The user can choose which figures to plot among the following: torque map (as a function of the xy-currents), torque ripple both at no load and at nominal current (as a function of the rotor angle), flux linkage map (as a function of the xy-currents), operation region (in the xy-current domain), torque vs. speed characteristic, input and output power vs. speed characteristics and efficiency map (as a function of the torque and the speed of the machine).

Moreover, the software allows to automatically repeat the full process explained here for one machine a number of times for different machine geometries, without requiring any user interaction. This feature is very helpful when conducting parametric studies on a certain topology. Once the simulations are finished, the designer can compare the properties of interest of the different machines and draw the corresponding conclusions.

Appendix C

Dynamic vehicle model for driving cycle simulations

This appendix describes the model used in the driving cycle simulations presented in Chapter 3. The model is implemented in Matlab-Simulink, and it is based in the work published by K. Johansson and M. Alaküla in [65, 66]. The top layer of the model is presented in Figure C.1.
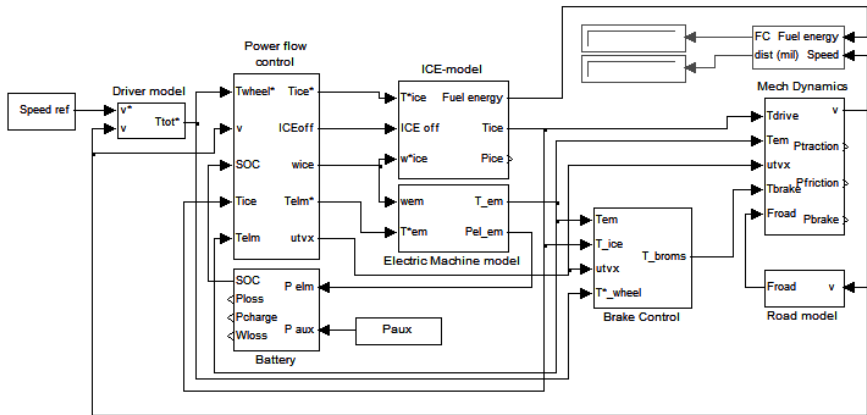
Figure C.1: Simulink model of a Parallel Hybrid Electric Vehicle.

A brief description of the different blocks is presented next, for a better understanding of the simulation results.

Speed Reference: This is the input block. Inside this block the selected driving cycle is loaded, and the different signals are conveniently forwarded to the corresponding blocks in the model.

Driver model: This block represents the behavior of the driver. It is implemented as a PI controller with anti windup. The PI parameters are dependent on the vehicle mass.

Power flow control: This is a key block in the model, where the power control algorithm is implemented. In the particular case of the simulations presented in Chapter 3 first the total power needed for traction and battery charging is computed, and based on it, the optimal operation point of the ICE is selected according to the ICE efficiency map. Since there is a clutch in between the ICE and the rest of the system, the variable *IceOff* is included to model it. For a certain required power level, the ICE is engaged if:

a. The ICE efficiency, assuming that it can be operated in the optimal point for the required power, is higher than a certain threshold.

b. The total power required is higher than a certain level.

Subsequently, the most suitable gear is selected in the *Gear Selection Block* according to the optimal speed of the shaft for the required power.

Figure C.2: Power flow control block.

ICE model: The ICE is modeled as a look-up table, giving the energy efficiency of the ICE for the given torque and speed. The efficiency map is based on a real measured ICE map, and scaled up or down if needed. A low pass filter is included in the torque reference to limit the dynamics of the ICE.

Electrical machine model: The electrical machine model first verifies that the required torque from the electrical machine is achievable at the actual speed, since a power limitation applies on the electrical machine. Then, a look-up table gives the efficiency of the electrical machine for the given torque and speed. This look-up table is based on general considerations and previous design experience, and although it does not represent any machine in particular, it gives a good approximation of the behavior of a prototypical traction permanent magnet synchronous machine. Besides, the efficiency of the power electronics and the gearbox are taken into account and they are assumed to be constant.

Figure C.3: Electrical machine model block.

Battery: In this block, the power generated/consumed by the electrical machine and the auxiliary power consumption, assumed constant in average, are added up together and affected by the battery charging/discharging efficiency, obtained from a look-up table as a function of the battery power. Then, the resulting charging/discharging power is integrated, in order to compute how much energy is left in the battery pack.

Brake control: This block computes the torque applied by the friction brakes. In principle, the electrical machine is used to brake as much as possible, feeding the braking energy back to the battery. However, in case the electrical machine is not able to produce enough braking torque, the friction brakes should contribute as well.

Road model: The air resistance and the rolling resistance are computed inside this block.

Mechanical dynamics: Based on the different forces applied to the vehicle, the road slope and the vehicle mass and load, the final speed is computed at each time.

List of Figures

List of Tables

Glossary

β_{med} thermal expansion coefficient of the medium *med* $(1/K)$

Δp pressure drop (Pa)

λ_{med} thermal conductivity of the medium *med* $(W/(m\,K))$

ν_{med} kinematic viscosity of the medium *med* (m^2/s)

ω rotational speed (rad/s)

Ψ_m Magnetic flux from the rotor permanent magnets that links the stator windings (Vs)

ρ_{med} density of the medium *med* (kg/m^3)

ε surface roughness height (m)

A_{sub} cross sectional area (m^2). Different subindexes may apply

B Magnetic flux density field (Vs/m^2)

b as subindex; bulk, usually referred to a fluid

cd as subindex; relative to the stator cooling ducts

d_{sub} distance (m); usually measured in the plane perpendicular to the symmetry axis. Different subindexes may apply

f frequency (Hz)

f_d Darcy friction factor (-)

g as subindex; relative to the airgap

g gravity constant $(g = 9.81\,m/s^2)$

Gr Grashof number (-)

h_{ca} convection coefficient at the outer surface of the motor $(W/(m^2\,K))$

h_{et} convection coefficient at the stator end windings $(W/(m^2\,K))$

h_{ica} convection coefficient at the inner surface of the outer case $(W/(m^2\,K))$

h_m thickness of the rotor permanent magnets (m)

h_{rr} convection coefficient at the rotor end rings $(W/(m^2\,K))$

I_{ax} moment of inertia with respect to the symmetry axis $(kg\,m^2)$

$i_{sx,sy}$ Stator voltage (peak value) (A) in the rotor reference frame (x,y)

J current density in the windings (peak value) (A/mm^2)

K_{sub} geometric proportion (-); used to parametrize the motor geometry. Different subindexes may apply

L_{sub} length (m); usually measured in the axial direction of the machine. Different subindexes may apply

$L_{sx,sy}$ Stator winding inductance (H) in the rotor reference frame (x,y)

lam as subindex; relative to the laminated turns

m mass, (Kg)

n rotor speed (rpm)

n, *nom*   as subindex; nominal

N_p Number of poles (-)

N_t Number of turns in the winding (-)

N_w Number of parallel wires in a winding turn (-)

Nu Nusselt number (-)

P power (kW)

p pressure (Pa)

r_{sub}	radius (m); usually measured in the plane perpendicular to the symmetry axis. Different subindexes may apply	DCM	Direct Current Motor
R_s	Stator resistance (Ω)	E-RWD	Electric Rear Wheel Drive
R_{th}	thermal resistance $(m^2\,K/W)$	emf	electromagnetic force (V)
Ra	Rayleigh number (-)	EMSM	Electrically Magnetized Synchronous Motor
Re	Reynolds number (-)	EV	Electric Vehicle
ri	as subindex; relative to the rotor, inner	FE	Finite Element
ro	as subindex; relative to the rotor, outer	FEA	Finite Element Analysis
rub	as subindex; relative to the rubber supports	HEV	Hybrid Electric Vehicle
si	as subindex; relative to the stator, inner	ICE	Internal Combustion Engine
so	as subindex; relative to the stator, outer	IM	Induction Motor (asynchronous AC electrical machine)
T	motor torque (Nm)	IPMSM	Interior Permanent Magnet Synchronous Motor
t	time (s)	LLL	Linear behavior Limit Line
th	as subindex; relative to the stator teeth	MMF	Magneto Motive Force (Ampere-Turn AT)
U_{DC}	DC voltage of the drive unit (V)	MTPA	Maximum Torque Per Ampere current loci
$U_{sx,sy}$	Stator voltage (peak value) (V) in the rotor reference frame (x,y)	MTPV	Maximum Torque Per Volt current loci
v	speed, (m/s)	PI	Proportional - Integral controller
y	as subindex; relative to the stator yoke	PMSM	Permanent Magnet Synchronous Motor
AC	Alternating Current	RMS	Root Mean Square value
CFD	Computational Fluid Dynamics	SMC	Soft Magnetic Composite
DC	Direct Current	SRM	Switched Reluctance Motor
		SynRM	Synchronous Reluctance Motor

References

[1] Electric Drive Transportation Association. Website, accessed on April 2013. `http://www.electricdrive.org/index.php?ht=d/sp/i/20952/pid/20952`.

[2] The International Council on Clean Transportation. Website, accessed on April 2013. `http://www.theicct.org/sites/default/files/publications/Pocketbook_2012_opt.pdf`.

[3] Opplysningsrådet for Veitrafikken AS (in Norwegian). Website, accessed on December 2013. `http://ofvas.no/bilsalget/bilsalget_2013/bilsalget_i_november/`.

[4] Adam R. Brandt and Alexander E. Farrell. Scrapping the bottom of the barrel: greenhouse gas emission consequences of a transition to low-quality and synthetic petroleum resources. *Climatic Change*, 84(3-4):241–263, October 2007.

[5] University of California San Diego. Website, accessed on April 2013. `http://physics.ucsd.edu/do-the-math/2012/02/fossil-fuels-im-not-dead-yet/`.

[6] Central Intelligence Agency. Website, accessed on April 2013. `https://www.cia.gov/library/publications/the-world-factbook/geos/xx.html`.

[7] International Energy Agency. Website, accessed on April 2013. `https://www.iea.org/newsroomandevents/pressreleases/2012/november/name,33015,en.html`.

[8] B. Metz, O.R. Davidson, P.R. Bosch, R. Dave, and L.A. Meyer. Cntribution of Working Group III to the Fourth Assessment Report on the Intergovernmental Panel on Climate Change. Technical report, Intergovernmental Panel on Climate Change, 2007.

[9] US Environmental Protection Agency. Website, accessed on April 2013. `http://www.epa.gov/climatechange/ghgemissions/global.html`.

[10] Envia Systems Inc. Website, accessed on April 2013. `http://enviasystems.com/technology/`.

[11] Hitachi Ltd. Website, accessed on April 2013. `http://www.hitachi-ve.co.jp/en/products/spec/index.html`.

[12] Website, accessed on June 2013. `http://www.hybrid-vehicle.org/hybrid-vehicle-history.html`.

[13] Website, accessed on June 2013. `http://www.autoevolution.com/news/hybrid-vehicles-a-short-history-of-the-alternative-drive-1779.html`.

[14] Website, accessed on June 2013. `http://www.hybridcars.com/100th-anniversary-first-us-hybrid-car-patent-25616/`.

[15] Toyota Motor Corporation. Website, accessed on June 2013. `http://www.toyota.com/about/our_business/our_history/product_history/pdf/prius.pdf`.

[16] Honda Motor Company. Website, accessed on June 2013. `http://www.honda.com/newsandviews/article.aspx?id=6927-en`.

[17] Website, accessed on June 2013. `http://www.dailytech.com/Toyota+Prius+Was+TopSelling+Vehicle+in+Japan+for+2009/article17360.htm`.

[18] Ford Motor Company. Website, accessed on June 2013. `http://media.ford.com/article_display.cfm?article_id=18541`.

[19] Website, accessed on June 2013. `http://www.edmunds.com/toyota/highlander-hybrid/2006/`.

[20] Website, accessed on June 2013. `http://www.edmunds.com/lexus/rx-400h/`.

[21] Website, accessed on June 2013. `http://green.autoblog.com/2009/02/02/volkswagen-to-launch-touareg-bluemotion-hybrid-in-2010/`.

[22] BMW AG. Website, accessed on June 2013. `http://www.bmw.com/com/en/newvehicles/x/x6_active_hybrid/2009/introduction.html`.

[23] ABB. Website, accessed on June 2013. `http://www.abb.com/cawp/seitp202/9eb9d7ffad753a5fc12579ba0039652a.aspx`.

[24] Peugeot. Website, accessed on June 2013. `http://www.peugeot.com/en/technology/engines/hybrid4`.

[25] Sture Eriksson. *Electrical Machine Development: a study of four different machine types from a Swedish perspective.* PhD thesis, Department of Electrical Machines and Power Electronics, School of Electrical Engineering, Royal Institute of Technology (KTH), Stockholm, 2007.

[26] Avo Reinap, Dan Hagstedt, Francisco Márquez-Fernández, and Yury Loayza. Development of a radial flux machine design environment. In *XVIII International Conference on Electrical Machines ICEM2008*, Vilamoura (Portugal), 2008.

[27] Jae Jun Lee, Won Ho Kim, Jin Seung Yu, Si Yeong Yun, Sang Min Kim, Jin Ju Lee, and Ju Lee. Comparison between concentrated and distributed winding in IPMSM for traction application. In *International Conference in Electrical Machines and Systems (ICEMS)*, Incheon (Korea(South)), Oct 10-13 2010.

[28] Hyung-Woo Lee, Chan-Bae Park, and Byung-Song Lee. Performance comparison of the railway traction IPM motors between concentrated winding and distributed winding. In *IEEE International Transportation Electrification Conference and Expo (ITEC)*, Dearborn (USA), June 18-20 2012.

[29] F. Leonardi. The Interior Permanent Magnet Machine: motor of choice for the HEVs of the 21st century. Lecture, 2008.

[30] Hector Zelaya de la Parra, Freddy Magnussen, and Sjoerd Bosga. Challenges for Electric Machines and Power Electronics in Automotive Applications. In *International Conference and Exhibition on Ecological Vehicles and Renewable Energies (EVER)*, Monaco, March 26-29 2009.

153

[31] M. A. Rahman. IPM Motor Drives for Hybrid Electric Vehicles. In *International Aegean Conference on Electrical Machines and Power Electronics (ACEMP)*, Bodrum (Turkey), Sept 10-12 2007.

[32] Sakai Kazuto, Hagiwara Keizo, and Hirano Yasuo. High-Power and High-Efficiency Permanent-Magnet Reluctance Motor for Hybrid Electric Vehicles. *Toshiba Review*, 60(11):41–44, 2005.

[33] Thomas Finken, Marco Hombitzer, and Kay Hameyer. Study and comparison of several permanent-magnet excited rotor types regarding their applicability in electric vehicles. In *Emobility - Electrical Power Train, 2010*, Leipzig (Germany), 2010.

[34] BEVI AB. Website, accessed on July 2011. `http://www.bevi.com`.

[35] Ayman EL-Refaie and Thomas M. Jahns. Optimal Flux Weakening in Surface PM Machines Using Fractional-Slot Concentrated Windings. *IEEE Transactions on Industry Applications*, 41(3):790–800, May/June 2005.

[36] Freddy Magnussen and Chandur Sadarangani. Performance Evaluation of Permanent-Magnet Synchronous Machines with Concentrated and Distributed Windings Including the Effect of Field-Weakening. In *IEE International Conference on Power Electronics, Machines and Drives*, Edinburgh (UK), March 31 - April 2 2004.

[37] Lester Chong, Rukmi Dutta, Nguyen Quang Dai, M. F. Rahman, and Howard Lovatt. Comparison of Concentrated and Distributed Windings in an IPM Machine for Field Weakening Applications. In *20th Australasian Universities Power Engineering Conference (ITEC)*, Christchurch (New Zealand), Dec 5-8 2010.

[38] Freddy Magnussen and Chandur Sadarangani. Winding Factors and Joule Losses of Permanent Magnet Machines with Concentrated Windings. In *IEEE International Electrical Machines and Drives Conference (IEMDC)*, Madison (USA), 2003.

[39] You-Young Choe, Se-Young Oh, Sang-Hwan Ham, Ik-Sang Jang, Su-Yeon Cho, Ju Lee, and Kwang-Cheol Ko. Comparison of Concentrated and Distributed Winding in an IPMSM for Vehicle Traction. *Energy Procedia*, 13:1368–1373, 2012.

[40] J.S. Hsu, C.W. Ayers, and C.L. Coomer. Report on Toyota Prius motor design and manufacturing assessment. Technical Report ORNL/TM-2004/137, Oak Ridge National Laboratory, July 2004.

[41] A. Vagati, G. Pellegrino, and P Guglielmi. Comparison between SPM and IPM motor drives for EV application. In *XIX International Conference on Electrical Machines ICEM2010*, Roma (Italy), 2010.

[42] Wen L. Soong and Nesimi Ertugrul. Field-Weakening Performance of Interior Permanent-Magnet Motors. *IEEE Transactions on Industry Applications*, 38(5):1251–1258, Sept/Oct 2002.

[43] Surahammars Bruk AB. Website, accessed on April 2013. `http://www.sura.se/Sura/hp_products.nsf/v0pendocument/03A8B2433FAE16C4C1256AA8002280E6/$FILE/250-35.pdf?OpenElement`.

[44] Sura Magnets AB. Website, accessed on July 2011. `http://www.suramagnets.se`.

[45] Tamagawa Seiki CO. LTD. Website, accessed on April 2013. `http://www.tamagawa-seiki.com/pdf/download/1570N11EJ.pdf`.

[46] HBM GmbH. Website, accessed on April 2013. `http://www.hbm.com.pl/arch/b0274.pdf`.

[47] Fluke CO. Website, accessed on April 2013. `http://assets.fluke.com/manuals/norma___omeng0200.pdf`.

[48] LEM SA. Website, accessed on April 2013. `http://www.lem.com/docs/products/it%20150-s%20ultrastab.pdf`.

[49] Francisco Márquez-Fernández, Avo Reinap, and Mats Alaküla. Design, optimization and construction of an electric motor for an Electric Rear Wheel Drive unit application for a Hybrid Passenger Car. In *XIX International Conference on Electrical Machines ICEM2010*, Roma (Italy), 2010.

[50] Yury Loayza, Avo Reinap, and Mats Alaküla. Performance and efficiency evaluation of FPGA controlled IPMSM under dynamic loading. In *VIII IEEE International Symposium on Diagnostics for Electrical Machines, Power Electronics and Drives (SDEMPED)*, Bologna (Italy), Sept 5-8 2011.

[51] Eloy Sánchez Caton. Dynamic braking: A new approach for testing electrical machines. Master's thesis, Faculty of Engineering, Lund University, 2012.

[52] Aldo Boglietti, Andrea Cavagnino, David Staton, Martin Shanel, Markus Mueller, and Carlos Mejuto. Evolution and Modern Approaches for Thermal Analysis of Electrical Machines. *IEEE Transactions on Industrial Electronics*, 56(3):871–882, March 2009.

[53] Joachim Lindström. Thermal model of a permanent-magnet motor for a hybrid electric vehicle. Technical report, Dep. of Electric Power Engineering, Chalmers Institute of Technology, 1999.

[54] Gunnar Kylander. *Thermal modelling of small cage induction motors*. PhD thesis, Dep. of Electric Power Engineering, Chalmers Institute of Technology, 1995.

[55] Shafigh Nategh. *Thermal Analysis and Management of High-Performance Electrical Machines*. PhD thesis, School of Electrical Engineering, Royal Institute of Technology (KTH), June 2013.

[56] David Staton, Aldo Boglietti, and Andrea Cavagnino. Solving the Most Difficult Aspects of Electric Motor Thermal Analysis in Small and Medium Size Industrial Induction Motors. *IEEE Transactions on Energy Conversion*, 20(3):620–628, September 2005.

[57] David Staton, Aldo Boglietti, and Andrea Cavagnino. Solving the Most Difficult Aspects of Electric Motor Thermal Analysis. In *IEEE International Electrical Machines and Drives Conference (IEMDC)*, Madison (USA), 2003.

[58] Emmanuel Hoang, Michel Lécrivain, Sami Hlioui, Hamid Ben Ahmed, and Bernard Multon. Element of Slot Thermal Modelling. In *IEEE International Symposium on Power Electronics, Electrical Drives, Automation and Motion (SPEEDAM)*, Pisa (Italy), June 2010.

[59] Aldo Boglietti, Andrea Cavagnino, and David Staton. Determination of Critical Parameters in Electrical Machine Thermal Models. In *Industry Applications Conference 2007. 42nd IAS Annual Meeting*, 2007.

[60] S. Gilchrist, C. Y. Ching, and D. Ewing. Heat Transfer Enhancement in Axial Taylor-Couette Flow. In *ASME 2005 Summer Heat Transfer Conference*, San Francisco (USA), July 17-22 2005.

[61] Zlatko Kolondzovski. Determination of Critical Thermal Operations for High-Speed Permanent Magnet Electrical Machines. *COMPEL, The International Journal for Computation and Mathematics in Electrical and Electronic Engineering*, 27(4):720–727, July 2008.

[62] Frank P. Incropera and David P. DeWitt. *Fundamentals of heat and mass transfer*. John Wiley & sons, 6 edition, 2006.

[63] Miroslav Marković, Laurie Saunders, and Yves Perriard. Determination of the Thermal Cconvection Coefficient in Small Electric Motors. In *Industry Applications Conference 2006. 41st IAS Annual Meeting*, 2006.

[64] Francisco Márquez-Fernández, Avo Reinap, Zhe Huang, and Mats Alaküla. Dynamic evaluation of the overloading potential of a convection cooled Permanent Magnet Synchronous Motor. In *2011 IEEE International Electrical Machines and Drives Conference IEMDC2011*, Niagara Falls (US), 2011.

[65] Karin Jonasson. *Control of Hybrid Electric Vehicles with Diesel Engines*. PhD thesis, Department of Industrial Electrical Engineering and Automation, Faculty of Engineering, Lund University (LTH), 2005.

[66] Mats Alaküla, Karin Jonasson, Cristian Andersson, Bengt Simonsson, and Sabine Marksell. Hybrid drive systems for vehicles, part 1. Course material, Department of Industrial Electrical Engineering and Automation, Faculty of Engineering, Lund University (LTH), 2004.

[67] Regulation No 83 of the Economic Commission for Europe of the United Nations (UN/ECE) Uniform provisions concerning the approval of vehicles with regard to the emission of pollutants according to engine fuel requirements. Official Journal of the European Union, February 2012.

[68] US Environmental Protection Agency. Website, accessed on July 2013. `http://www.epa.gov/otaq/standards/light-duty/sc06-sftp.htm`.

[69] Statoil ASA. Website, accessed on July 2013. `https://external.statoilfuelretail.com/mar/svg01184.nsf/design/lub_pds/$file/TransWay_S_DX_III_F_SE.pdf`.

[70] Dow Chemical Company. Website, accessed on July 2013. `http://msdssearch.dow.com/PublishedLiteratureDOWCOM/dh_0030/0901b803800303d6.pdf?filepath=/heattrans/pdfs/noreg/176-01240.pdf&fromPage=GetDoc`.

[71] Francisco Márquez-Fernández, Zhe Huang, and Mats Alaküla. Redesign of an Electrical Rear Wheel Drive (E-RWD) for a Hybrid Vehicle in a given drive cycle. In *XX International Conference on Electrical Machines ICEM2012*, Marseille (France), 2012.

[72] Abdul Rehman Tariq, Carlos E. Nino-Baron, and Elias G. Strangas. Overload Considerations for Design and Operation of IPMSMs. *IEEE Transactions on Energy Conversion*, 25(4):921–930, December 2010.

[73] Zhe Huang, Francisco Márquez-Fernández, Mats Alaküla, and Jinliang Yuan. Characterization and application of forced cooling channels for traction motors in HEVs. In *XX International Conference on Electrical Machines ICEM2012*, Marseille (France), Sept. 2-5 2012.

[74] Zhe Huang, Shafigh Nategh, Viktor Lassila, Mats Alaküla, and Jinliang Yuan. Direct oil cooling of traction motors in hybrid drives. In *International Electric Vehicle Conference IEVC2012*, Greensville, South Carolina (USA), March 4-8 2012.

[75] Zhe Huang. Thermal Design of Electrical Machines - Investigation and Evaluation of Cooling Performances. Licentiate thesis, IEA - LTH, 2013.

[76] Conny Högmark, Avo Reinap, Kenneth Frogner, and Mats Alaküla. Laminated winding with rapid cooling capability for electrical machines. In *International Conference for Inductive and Electromagnetic Components Systems and Devices including Manufacturing and Processing, INDUCTICA 2012*, Berlin (Germany), June 26-28 2012.

[77] Conny Högmark, Rasmus Andersson, Avo Reinap, and Mats Alaküla. Electrical Machines with Laminated Winding for Hybrid Vehicle Applications. In *International Electric Drives Production Conference and Exhibition, EDPC 2012*, Nuremberg (Germany), Oct. 16-17 2012.

[78] LORD Corporation. Website, accessed on August 2013. `http://www.lord.com/products-and-solutions/electronic-materials/product.xml/561`.

[79] Rasmus Andersson, Conny Högmark, Avo Reinap, and Mats Alaküla. Modular Three-phase Machines with Laminated Winding for Hybrid Vehicle Applications. In *International Electric Drives Production Conference and Exhibition, EDPC 2012*, Nuremberg (Germany), Oct. 16-17 2012.

[80] Rasmus Andersson, Avo Reinap, and Mats Alaküla. Design and Evaluation of Electrical Machine for Parallel Hybrid Drive for Heavy Vehicles. In *XX International Conference on Electrical Machines ICEM2012*, Marseille (France), Sept. 2-5 2012.

[81] R. Kjellstrand and V. Akujärvi. Modeling and evaluation of laminated windings. Master's thesis, IEA - LTH, 2013.

[82] R.K. Shah. Thermal entry length solutions for the circular tube and parallel plates. *Proc.* 3rd *National Heat Mass Transfer Conference, Indian Inst. Technology Bombay*, Vol. 1(HMT-11-75), 1975.

[83] C.F. Colebrook. Turbulent flow in pipes, with particular reference to the transition region between smooth and rough pipe laws. *Journal of the Institution of Civil Engineers (London)*, February 1939.

[84] D. Meeker. Website, accessed on November 2013. `http://www.femm.info/wiki/HomePage`.